THESIS

A NEW LOOK AT THE EARTH'S RADIATION BALANCE FROM AN A-TRAIN OBSERVATIONAL PERSPECTIVE

Submitted by

David S. Henderson

Department of Atmospheric Science

In partial fulfillment of the requirements

For the Degree of Master of Science

Colorado State University

Fort Collins, Colorado

Fall 2010

Master's Committee:

Department Chair: Jeff Collett

Advisor: Graeme Stephens

Colette Heald
Venkatachalam Chandrasekar

ABSTRACT

A NEW LOOK AT THE EARTH'S RADIATION BALANCE FROM AN A-TRAIN OBSERVATIONAL PERSPECTIVE

The weather and climate of the Earth are driven by interactions of the longwave and shortwave radiation between the Earth's atmosphere and surface. Past studies have tried to derive the Earth radiative budget through the use of models and passive satellite sensors. These past efforts did not have information about the vertical distribution of cloud or aerosols within the atmosphere that significantly influence radiative transfer within the atmosphere. This problem was improved upon with the launch of CloudSat and CALIPSO in 2006. These satellites provide the information on the vertical distribution of clouds. From CloudSat, a fluxes and heating rates product was produced to study the radiative budget, but this was limited to some degree because of undetected clouds and aerosol that have non-negligible effects on the radiative balance.

This study addresses these issues by combining CALIPSO and MODIS data with CloudSat to detect and obtain the properties of cloud and aerosol undetected by the CloudSat CPR. The combined data were used to create a cloud and aerosol mask that identified distributions of undetected cloud and aerosol globally and

quantified their radiative effects both seasonally and annually. Low clouds were found to have the highest impacts of nearly -6 Wm^{-2}. High clouds globally have little effect, trapping 1 Wm^{-2}, with the majority of the impact in the tropics. Four case studies are presented to show how heating rates change in the vertical due low cloud, cirrus, precipitation, and aerosol. The cloud and aerosol mask was used to create seasonal global distributions of cloud radiative effect using all clouds detected by CloudSat and CALIPSO, and the direct effect of aerosols estimated at the TOA. Using fluxes at the top and bottom of the atmosphere global distributions of outgoing and incoming radiation are shown, and an annual radiation budget of the Earth is derived. Clouds globally are found to have a radiative forcing of -20 Wm^{-2} at the TOA. The radiative budget of the Earth is calculated in two ways; Using normalized shortwave fluxes by the average solar daily insolation, and by changing the solar zenith angle to simulate the diurnal cycle. Finally, the product is validated by comparing the outgoing and surface fluxes with CERES and ISCPP flux products.

David S. Henderson
Department of Atmospheric Science
Colorado State University
Fort Collins, CO 80523
Fall 2010

ACKNOWLEDGMENTS

The completion of this research would not have been possible without the help of my family, friends and co-workers. My friends here at CSU have assured me that I am not the only one that has struggled, felt stressed, or gotten extremely frustrated at code that isn't working. My friends and family back on the east coast that have kept in contact with me, have helped me keep a smile on my face throughout the M.S. process. My many officemates in 205 that have given plenty of distractions and humor that have been great. A special thanks to roommates Eric Guillot, Gus Alaka, Jeremiah Sjoberg, Darren Van Cleave, and Zach Finch, that I have had over the past two years and have become great friends. I would like to thank Phil Partain and Don Reinke in the CloudSat data Center, who have completed an enormous amount of data processing for me and taught me how to use the systems needed to process data. Without them I would still been waiting on my data to finish. I would like to give great appreciation to Tristan L'Ecuyer who has given me so much guidance and help throughout the past two years. Thanks to Norm Wood, Matt Rodgers, and Natalie Toureville who have taught me so much more about programming, computer problems, and hardware issues than I knew existed. I would like to give great thanks to Graeme Stephens for taking me on as a student and providing an opportunity to do work I enjoy, and to my other committee members Colette Heald and Chandra for there help throughout the thesis process. Finally, I am thankful to

complete my research through the funding of the NASA CloudSat Mission grant NAS5-99237.

David Henderson
Colorado State University
October 2010

TABLE OF CONTENTS

1. INTRODUCTION

1.1 Importance

The amount of solar radiation from the sun impacting the Earth's atmosphere and surface is one of the most important factors in determining the weather and climate systems we see today. It is how this radiation interacts with objects in our atmosphere that makes it such a difficult, but yet fascinating subject to study. Although, the subject of an Earth Radiative Budget (ERB) is no new area of study, it is quite important to use the tools we have today to further observe the mechanisms in our atmosphere that occur due to variations in solar energy, and exchanges in energy between objects in our atmosphere or the Earth's surface.

The diabatic heating of the Earth's surface is one process which controls the circulation patterns we see on our atmosphere, both on small and larger time scales. It is known that there is an imbalance of solar radiation absorbed at the Earth's surface compared to emitted outgoing longwave (LW) radiation (Ellis and Vander Haar, 1976), and that this imbalance of radiation from the equator to the poles helps to drive atmospheric and oceanic circulations responsible for Earth's ever changing weather patterns (Ramanathan, 1987). Early observations of circulations in the atmosphere were discovered by Halley (1686), hypothesizing that the warm air in

the tropics were more likely to rise. This helped lead to the discovery of the Hadley Cell and other large scale tropical circulations driven by surface diabatic heating, which are explained in more detail by Gill (1980). The magnitude and distribution of longwave radiative forcing by tropical clouds are known to be a key factor in the location and amount of tropical precipitation, upper tropospheric circulations, as well as extratropical flow patterns (Slingo and Slingo, 1988, 1991). Other circulations such as the Madden-Julian Oscillation (MJO) and the Walker Circulation have been found to be affected by the vertical distribution of heating in the atmosphere (Hartmann et al. 1984, Madden and Julian 1972). In fact, Lau and Peng (1987) found that the location of the diabatic heating maximum affects the phase speed of the waves that control the magnitude and length of the MJO. The strength of the MJO is of much importance as it affects the amount of deep convection and precipitation received in areas affected by the MJO (Webster, 1994), short-term weather prediction (Hendon et al. 2000), and even long-term hurricane prediction (Maloney and Hartmann, 2000).

Knowing that radiation is a key player in our atmosphere circulations, it is also necessary to look at how radiation interacts with clouds and aerosols in the atmosphere. Clouds affect the radiative balance of the Earth by reflecting shortwave (SW) radiation back to space, as well as trapping longwave (LW) radiation back to the surface. These competing affects are essential to understanding our Earth's climate system (Stephens, 2005), but yet at the same time clouds and cloud feedbacks in the climate system still remain a large unknown in climate change (Stephens et al. 2002). Distributions of cloud vary throughout the atmosphere, and

different cloud types can have different effects on the Earth's climate, circulations, and ERB (Warren et al, 1988). It could be thought that because clouds exhibit both warming and cooling features, the actual effect of clouds could be minimal. This however, does not take into account the type of cloud, location of cloud, and the time that the cloud exists in a certain region. Two specific examples of this would be cirrus clouds and low-level stratus clouds.

Cirrus clouds have a unique impact on the ERB due to their high greenhouse effect compared to their albedo effect. The radiative effect of cirrus clouds depend greatly on their microphysical properties (Liou 1986; Stephens et al. 1990), in which these properties lead to a reflection of infrared radiation back towards the Earth's surface leading to a more warming effect on our climate (Stephens, 1980). Studies, such as from Halliday and Stephens (2009) and Sassen et al. (2009), show that the distribution of cirrus are found largely in the tropics associated with large convective cumulus. Some of these cirrus are considered optically thin (optical depths near 0.1) and are difficult to detect, but are still important in analyzing our Earth's radiative budget.

Low stratus decks have a nearly opposite effect as cirrus. They are low lying compared to the ground; therefore they do not have too much effect on outgoing longwave radiation (OLR). For low-level clouds, the albedo effect tends to dominate the net radiation, causing a large negative impact on the ERB and a 'cooling' effect on the overall climate (Manabe and Strickler 1964, Slingo 1990, Tian and Ramanathan 2002). Klein and Hartmann (1993) observe three regions containing larger amounts of marine stratus off the western coasts of N. America, S. America,

and Africa and identify they have a large impact on the ERB. These regions impose a large regional impact of negative cloud forcing where the albedo effect is large as the majority of the region is filled with low stratus decks, and there is little effect on the LW as the clouds emit at similar temperatures of the surface.

Clouds are not the only player in determining the distribution of radiation in our current climate. Precipitation in clouds as well as aerosols can cause changes in absorption, latent heat release, and even change cloud properties. Looking at aerosols, we know aerosols affect radiation through their direct and indirect effects on the ERB. One important aspect in calculating the ERB would be observing how tropospheric aerosols directly effect radiation. Charlson et al. (1991) gives an example of this when he discusses how sulfate aerosols can reflect solar radiation, thus lowering the amount of radiation reaching the Earth's surface. This is not limited to just sulfates, but also dust, carbonaceous aerosol, and minerals in the air causing scattering and absorption of solar and infrared radiation (Sokolik and Owen, 1996). As stated, aerosols also affect the radiative balance indirectly by changing cloud properties. When aerosols are entrained into a cloud they act as condensation nuclei, which can change the albedo of the cloud by increasing drop concentration (Twomey, 1977), but also changes in precipitation as drop concentration begins to vary (Pincus and Baker, 1994).

1.2 History of Radiative Budget Studies

Satellites orbiting the Earth provide an excellent base to measure the energy being exchanged from the Earth, the atmosphere, and space. Vonder Haar and Suomi (1971) first derived an ERB from satellite, where they found the zonal averaged distribution of radiation. Their measurement came from some of the first generations of radiation measuring satellites: TIROS, Nimbus, and ESSA. Using data from these scanning sun-synchronous satellites over a five-year period they discovered that the Earth, as well as each hemisphere was in radiative balance (no need for an energy exchange over the equator). The study showed that the Earth had a calculated albedo (ratio of solar radiation reflected into space and how much reaches the surface) of 30%, lower than past calculated values and around the value that is accepted currently. One of the most important finds was the imbalance of solar radiation entering the Earth compared to outgoing longwave radiation. Earth orbiting satellites also allowed them to calculate the first radiative global budget and to illustrate the amounts of radiation entering and leaving the Earth on a global scale. From these measurements they calculated emitted LW radiation from the Earth of about 237 Wm^{-2}, which is quite close to the measurements we see today. This research helped to understand the ERB and the driving forces of the atmosphere, but also led to more satellite observations of radiation.

Subsequent to Vonder Haar and Suomi's research, numerous satellite studies involving the ERB were completed. Hartmann and Short (1980) used two NOAA scanning Radiometers to observe the outgoing IR longwave radiation (OLR) as well

as observations of albedo. Using these two parameters, they were able to determine cloud frequencies, distributions, and general circulations patterns over the Earth. Using the IR flux measurements, the distribution of clouds could be estimated by observing the standard deviation of OLR measurements. A high standard deviation meant larger differences in OLR, coming from the decreased LW emission from the tops of high clouds. Distributions of low clouds over the oceans are observed by comparing high albedo from clouds compared to the low albedo of the ocean. From the cloud observations they were able to see the movement of the intertropical convergence zone (ITCZ) as well as mid-latitude storm tracks.

Numerous studies used the Nimbus series satellites, more specifically Nimbus 6 and 7 to complete earlier studies of the ERB from space. Nimbus 6 and 7 both had an advantage over past satellites as their flat plate detectors measured in the broadband with outgoing SW radiation (OSR) measured from 0.2-0.38 um and OLR in the IR from 3.8->50 um. Nimbus 7 had an advantage over the Nimbus 6 as it also added a multi-axis scanner, which allowed it to scan for measurements horizontally at a higher resolution. Stephens et al. (1981) describe the advantages of the Nimbus satellites and use them to complete an ERB using the Nimbus series satellites as well as NOAA instruments in space. Their study showed similar results from Vonder Haar and Suomi with annual global average emitted radiant exitance of about 234 Wm^{-2}. They were able to show latitudinal distributed net radiation for each of the months confirming the idea that there was an excess of energy in the tropics, but a deficit near the poles. With the global distribution, they were able to see that the net radiation actually varied greatly by season around the Earth. These findings using

the newer satellites also agreed with previous values that were found using the Nimbus 6 satellite (Jacobowitz et al., 1979).

The Nimbus satellites were also used in order to observe the effects of clouds on the ERB. Studies such as Sohn and Smith (1991) and Ardanuy et al. (1989,1991) used the Nimubus 7 satellite to observe top of atmosphere (TOA) fluxes and determine the cloud forcing (amount of radiation at TOA from clouds compared to clear sky) as well as view the general circulation patterns of clouds. In the studies the net cloud forcing is defined as,

$$F_{net} = F_s - F_l \tag{1.1}$$

where F_s is the shortwave cloud forcing and F_l is the longwave cloud forcing. But, due to the differences in cloud forcing definitions each study has drastically different results. Sohn and Smith find a cloud forcing of -2.1Wm^{-2} and Ardanuy et al. find -26.8 Wm^{-2}. Both results show a global cooling effect of clouds, but the magnitude greatly differs. The difference from the studies comes from the definitions of cloud forcing used within the research. Sohn and Smith only define cloud forcing as the change in outgoing radiation with the change in cloud area, while Ardanuy et al. use this, but also include surface temperature, mixing ratios of absorbing gases, and subtract the clear-sky flux from the outgoing fluxes. The methods of Ardanuy et al. provide more information on the atmosphere and surface within its calculations. The results show a stronger cooling affect of clouds, but also seem to agree more with other studies taken from the Earth Radiation Budget Experiment (ERBE) mission.

The ERBE mission (Barkstrom, 1984) provides another group of sensors to observe the fluxes going in and out of the Earth's radiative system, and provides a higher resolution scanner compared to the Nimbus platforms. The satellite system in the ERBE mission consists of the mid-inclined orbiting (at 57 degrees) Earth Radiation Budget Satellite (ERBS) and two NOAA satellites that are in sun-synchronous orbit. The scanners used on the satellites provide higher resolution output at 2.5 x 2.5 latitude/longitude regions, but still coarser resolutions for the flat plate detectors. The data from the mission was designed to help users to better understand the effects of clouds on our climate system and to find the overall energy balance of our Earth. The mission was launched in 1984 and provided data with the scanner until 1990, while the flat plate detector provided data until 2003.

Ramanathan et al (1989) uses ERBE data to examine cloud radiative forcing over the time period of April 1985. This study was repeated over a longer time period by Harrison et al. (1990) who provided a look at the ERBE data and how it compared with previous studies of the impacts of clouds on the ERB. Their study gives information on how global measurements of cloud forcing in LW and SW give way to information on major climates and cloud systems over the Earth. Using the months of January and July in 1985 and 1986, respectively, they were able to determine a global cloud forcing of ranging from -21 Wm^{-2} to -17 Wm^{-2}. Global cloud forcing compared to the current climate models showed some similarities of the direction of forcing, but in many cases the magnitude and location of maxima and minima varied. Maximum negative cloud forcing was found in the mid-latitude storm tracks, in the summer hemisphere, and in the subsidence area off of the west

coast of S. America, where low cloud albedo effects dominate. The most positive areas of cloud forcing occurred in desert areas were clouds are minimal, and the deep convective areas in the Western Pacific near the ITCZ.

The satellite missions containing the Nimbus satellites and the ERBE satellites were major contributors in the discovery of the distribution of radiation on the Earth and the impacts of clouds on the ERB. The missions influenced atmospheric scientists to keep observing the Earth's radiation and continued with missions such as the Scanner Radiation Budget (ScaRaB) missions (Kandel et al., 1998) launched by The Centre National d'Etudes Spatiales (CNES), and the Geostationary Earth Radiation Budget (GERB) aboard the Meteosat Second Generation (MSG) satellite (Harries et al., 2005). Currently two of the major archives of the radiative budget of the Earth come from the Clouds and the Earth's Radiant Energy System (CERES) aboard Aqua and Terra (Wielicki et al., 1996) and the International Satellite Cloud Climatology Project (ISCCP); A collection of global radiance measurements from numerous satellites (Schiffer and Rossow, 1983).

The ISCCP program began in July 1983 as a part of the World Climate Research Programme. It was created to provide a data set comprised of radiance measurements from various satellites to derive global cloud distributions and properties. The satellites used in ISCCP come from around the globe and have included the TIROS, GOES, METEOSAT, and GMS satellites. The data from the satellites are combined to create a dataset of 2.5° x 2.5° latitude/longitude grids for every 3 hours in a day. The study is still continuing to this day and provides one of the longest climatologies of clouds and their properties available. Studies have

shown that the ISCCP data correlates well with the data from ERBE (Rossow and Zhang, 1995), but because of the coarse resolution of the data, not all annual fluxes agree. The outgoing LW radiation at TOA from Rossow and Zhang (1995) is similar to ERBE, but due to a high planetary albedo in the ISCCP data they show a net loss of energy at TOA, whereas ERBE reports a net gain. Another, more recent study with ISCCP has used the data to find the annual ERB for the Earth (Raschke et al, 2005). The studies ERB calculation varied from Kiehl and Trenberth (1997), and in some areas agreed more with Liou (1992) who used combined measurements from satellites and models to make a global ERB. When the data was compared with CERES differences were found from 10 Wm^{-2}, resulting from differences in clear sky calculation, properties used, and again the coarse resolution used in ISCCP causing issues in data matching.

CERES was first launched in the late 1990's aboard the Tropical Rainfall Measuring Mission, but the sensor failed within a year. The next CERES sensors were launched on the Terra and Aqua satellites in 1999 and 2002, respectively. CERES is currently one of the most up to date datasets of the ERB, and provides higher resolution (20 km horizontal) of radiative properties of the Earth. The CERES data has been used in the Global Energy and Water Cycle Experiment (GEWEX), and to derive the ERB and forcings of both cloud and aerosol (Kim and Ramanathan, 2008 and Quaas et al. 2007). The global ERB has been studied by CERES data and because the data set has now been available since 2000, the annual variability of the ERB can be observed (Kato, 2009) and the energy exchanges from the surface and atmosphere can be calculated (Lin et al., 2009). The

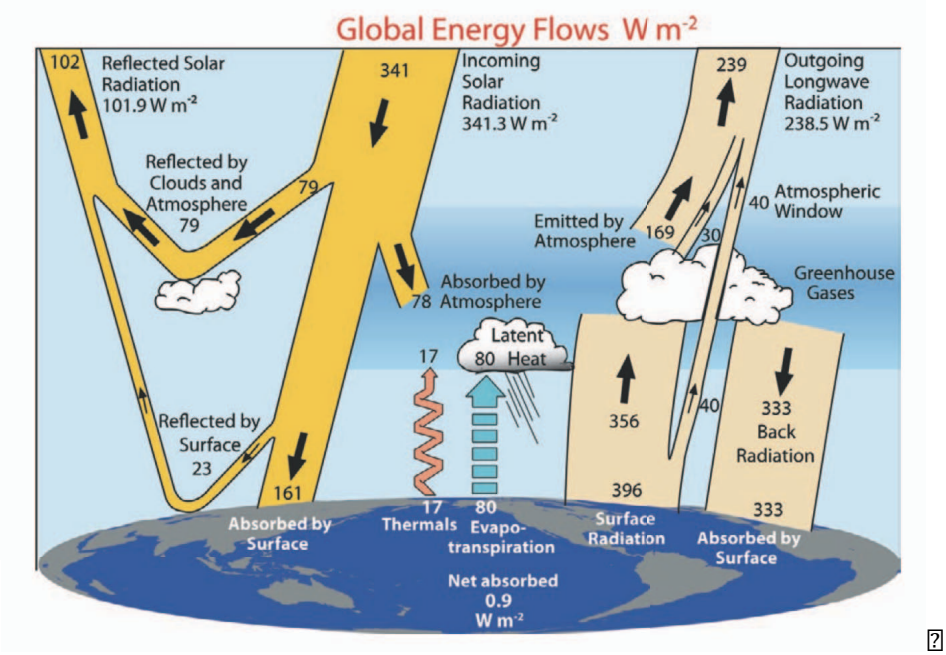
Global Energy Flows W m-2
102
Reflected Solar Radiation 101.9 W m-2
341
Incoming Solar Radiation 341.3 W m-2
239
Outgoing Longwave Radiation 238.5 W m-2
Reflected by Clouds and Atmosphere 79
79
Emitted by Atmosphere
169
30
40
Atmospheric Window
Absorbed by Atmosphere
78
Greenhouse Gases
Latent 80 Heat
17
Reflected by Surface 23
161
356
40
333 Back Radiation
396
333
Absorbed by Surface
17 Thermals
80 Evapo-transpiration
Surface Radiation
Absorbed by Surface
Net absorbed 0.9 W m-2

One major issue with the previously described studies is the inability for the satellites to detect anything within the atmosphere itself. This is of course, because the satellites are passive sensors that can only detect the radiation directly from the Earth. Kiehl and Tenberth (1997) describe that in order to properly represent the radiative impacts of clouds at the surface, we must know their properties and locations in the atmosphere. Because of this there was a need for an active sensor that could penetrate the atmosphere to directly detect the structure of clouds and aerosols. To answer this issue CloudSat (Stephens et al., 2002) and the Cloud-Aerosol Lidar and Infrared Pathfinder Satellite Observation (CALIPSO) (Winker et al., 2004, 2007) were launched in 2006 to join other satellites in the A-train. CloudSat is able to see clouds with a Cloud Profiling Radar (CPR) and CALIPSO is sensitive to both clouds and aerosols with a near-nadir pointing lidar. Stephens et al. (2002) describe the introduction of CloudSat to the A-train and how it can change our observations by giving more accurate data of cloud structure and properties, while also adding the ability to provide precipitation retrievals as well. The combination of CloudSat and CALIPSO finally allows high horizontal and vertical resolution of atmospheric properties. More information on the specifics of the satellites and their sensors can be found in Section 2.1.

1.3 Objective

With the ability to detect clouds and their properties in the vertical from CloudSat, there is now a way to derive vertical distribution of fluxes and heating rates in the atmosphere. This product was introduced to the CloudSat mission as one of its standard products. The product 2B-FLXHR (L'Ecuyer et al., 2008), described in Section 2.2.4, gives the user information on SW and LW TOA and bottom of atmosphere (BOA) fluxes and heating rates throughout the atmosphere. Using this product the CloudSat science team was able to estimate the impacts of clouds on the globally averaged annual ERB. This, however came with some assumptions that caused issues, due to the inability of CloudSat to detect all cloud types. L'Ecuyer et al. (2008) state that there needed to be improvement in the future to the algorithm to better detect all cloud types as well as describe precipitation properties.

Looking at the data from the 2B-FLXHR product, it does an excellent job of displaying the heating rates due the presence of clouds in the atmosphere. Figure 1.2 shows an example of heating rates extracted from the product and it is easy to see where the heating rates match the clouds in the CPR Cloud Mask. Cooling occurs at the tops of clouds in the longwave, as well as heating in the shortwave from the absorption of solar radiation. But, in these vertical distributions of heating rates lies a problem from the way precipitation is represented. Precipitation properties are given values of 50 mgm^{-3} for every cloud pixel up to the freezing level, decreasing liquid water linearly above freezing. This is based on cloud climatologies of

precipitation, but in some cases provides too much rain in clouds and especially when transitioning from liquid rain to ice, this creates a large spike in the heating rates with height consistently around 8 km. A similar issue with the excess of precipitation would be in the outgoing and downward fluxes. If precipitation is overestimated, the amount of solar radiation reflected back into space will also be overestimated in these areas. This is confirmed in Figure 1.3, by showing the large amounts of radiation being reflected by the precipitating portion of clouds. This effect of overestimating precipitation could have continued to effect the verification of the product using CERES data.

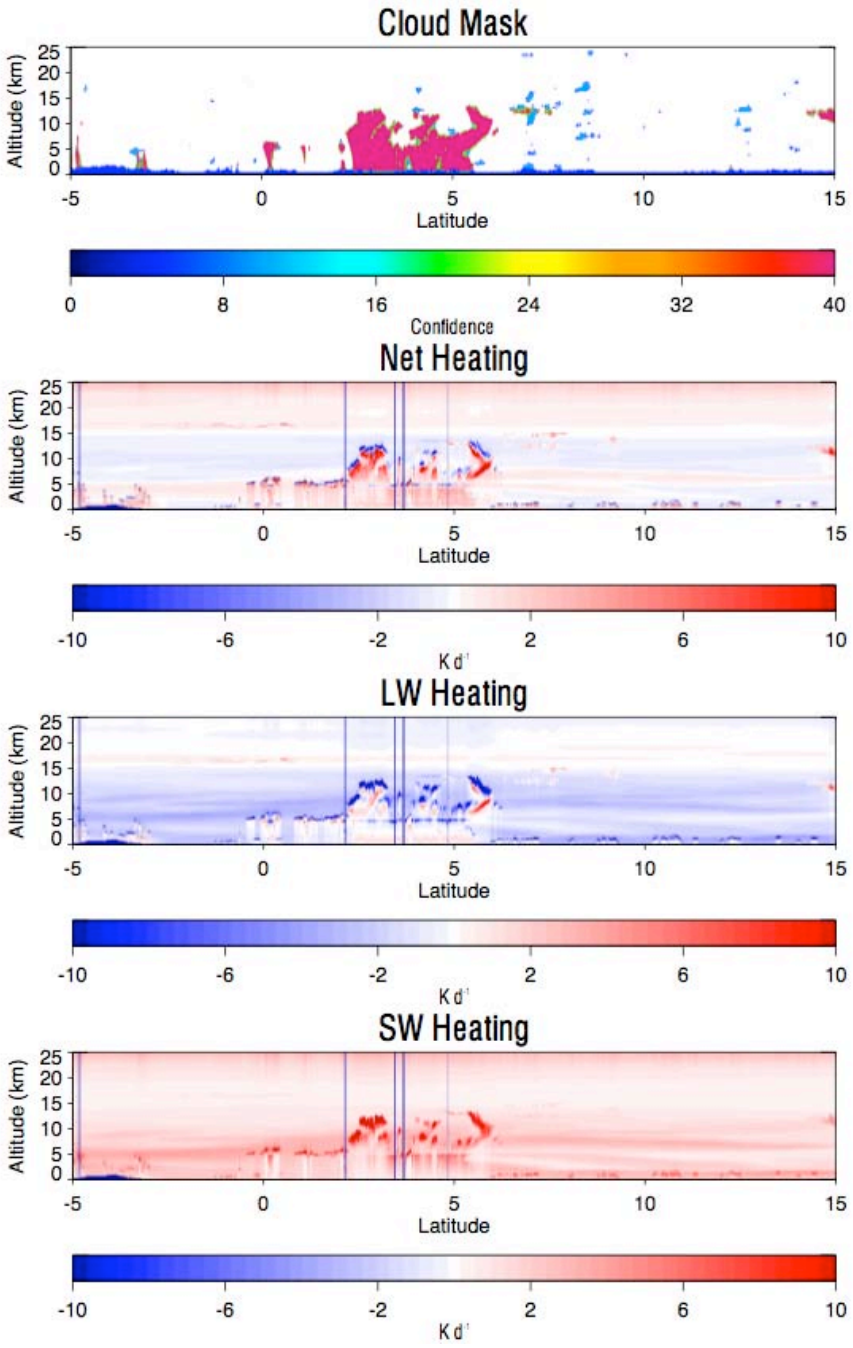

Figure 1.2. The heating rates taken from the 2B-FLXHR product from CloudSat. Areas with a blue bar extending from the surface to TOA are where calculations are not taken.

The comparison found from L'Ecuyer et al. (2008) (Figure 1.4) shows that the OSR is positively biased for CloudSat; that is that CloudSat is overestimating OSR compared to the CERES product. This, however, is odd because CloudSat does not

detect many of the low clouds on the Earth, suggesting that a negative bias would be expected, which is the opposite of their findings. This confirms that better cloud detection is definitely necessary to fully understand the ERB with this product. Fortunately a combination of other sensor data from the A-train provide this necessary data to determine how the ERB is affected by undetected cloud.

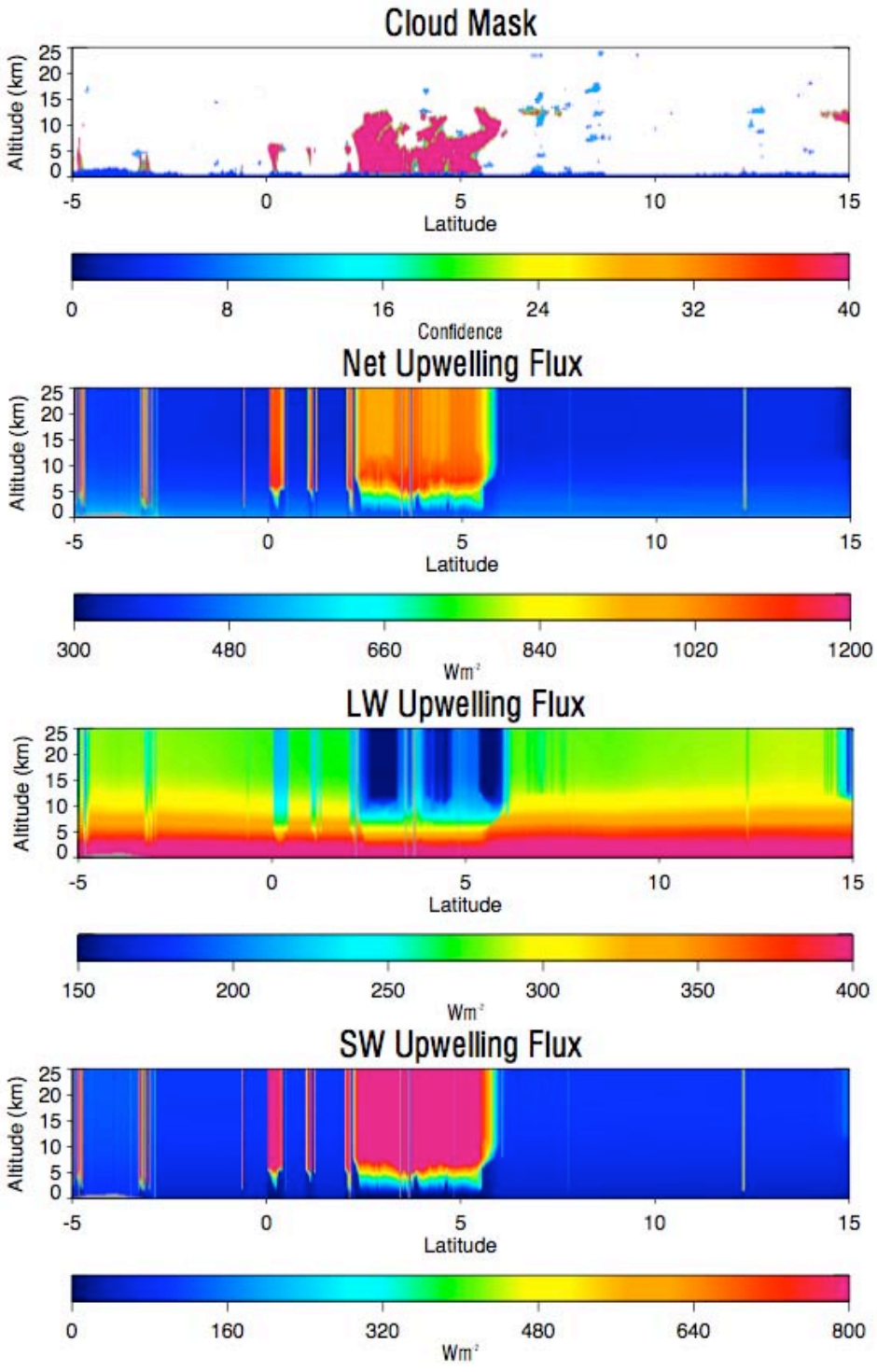

Figure 1.3. Upwelling fluxes from 2B-FLXHR. The large amount of upwelling solar radiation being reflected in the shortwave can be found in the precipitation clouds from ~0-5 degrees in latitude.

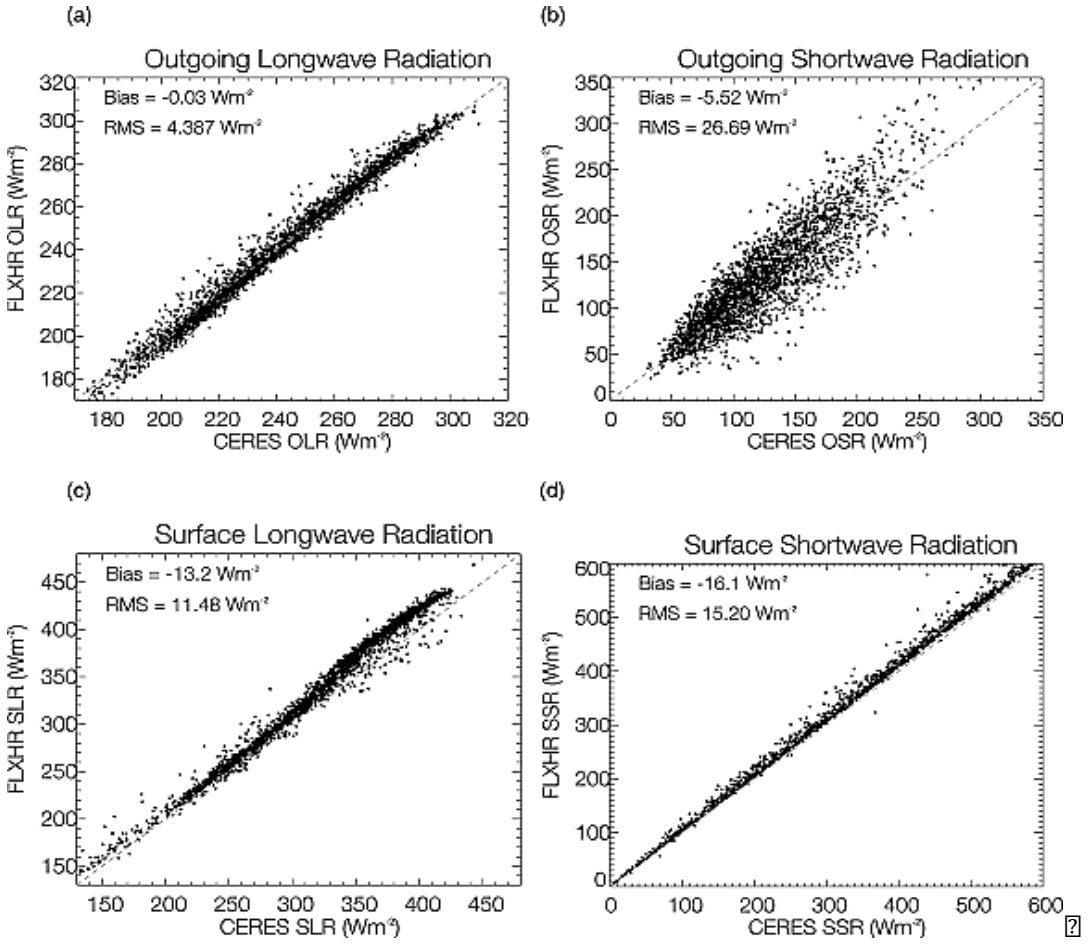
(a)
Outgoing Longwave Radiation
Bias = -0.03 Wm⁻²
RMS = 4.387 Wm⁻²
FLXHR OLR (Wm⁻²)
CERES OLR (Wm⁻²)
(b)
Outgoing Shortwave Radiation
Bias = -5.52 Wm⁻²
RMS = 26.69 Wm⁻²
FLXHR OSR (Wm⁻²)
CERES OSR (Wm⁻²)
(c)
Surface Longwave Radiation
Bias = -13.2 Wm⁻²
RMS = 11.48 Wm⁻²
FLXHR SLR (Wm⁻²)
CERES SLR (Wm⁻²)
(d)
Surface Shortwave Radiation
Bias = -16.1 Wm⁻²
RMS = 15.20 Wm⁻²
FLXHR SSR (Wm⁻²)
CERES SSR (Wm⁻²)

Section 3 will show the steps taken to detect new clouds and aerosols, then go over the process used to derive the properties of these new clouds and aerosols. Section 4 will concentrate on the results of this study with the radiative impacts of the clouds as well as look at heating rate profiles in the atmosphere. Regional results based on cloud climatologies that show where high level cirrus and low-level clouds are most prominent on Earth are discussed. Following the regional and global impacts of new clouds unseen by CloudSat, the globally averaged ERB for the year 2007 is calculated. This will focus on the top of atmosphere (TOA) fluxes, bottom of atmosphere (BOA) fluxes, and then the difference between them will be the fluxes contained in the atmosphere. The results from FHR-A are compared with results with other satellite missions and ERB evaluations to discuss any major differences found between them. Finally, in Section 5, a summary is presented along with future work and applications of the FHR-A data.

2. INSTRUMENTATION AND DATA

Described in this section is the satellites and their data used for detection, calculating cloud, aerosol, and precipitation properties.

2.1 Satellites and Sensors

The data for this research are taken from a series of satellites called the A-train (Figure 2.1). The name comes from the fact that the satellites are in sun synchronous orbit and cross the equator at 1:30 pm local time. The current constellation of satellites consists of four National Aeronautics and Space Administration (NASA) satellites called Aqua, CloudSat, CALIPSO, and Aura. In 2009, PARASOL (Polarization and Anisotropy of Reflectances for Atmospheric Sciences Coupled with Observations from a Lidar) was removed from the A-Train because it lacked the fuel to keep formation in the constellation. The satellites orbit close to each other, with Aqua and Aura only being separated by 7 minutes and are at an altitude of nearly 705 km above the Earth's surface. CloudSat and CALIPSO are the closest of the satellites being only separated by about 12.5 seconds (L'Ecuyer, 2010). This makes the pair useful for combining their data to better assess cloud and aerosol distributions.

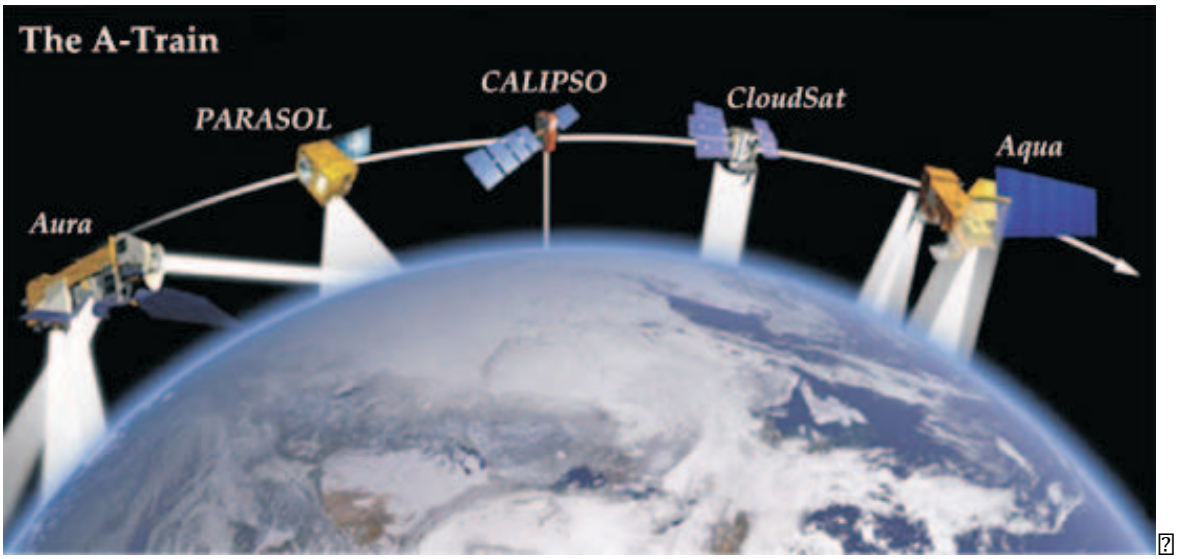
The A-Train
CALIPSO
PARASOL
CloudSat
Aqua
Aura

width of 3.3 μseconds, sent every 0.32 seconds, giving the CPR a horizontal resolution of 1.4 km and a vertical resolution of 240 m, due to overlapping samples.

This research utilizes many CloudSat products that are available from the CloudSat Data Processing Center (DPC). These products include the Radar-Only (RO) cloud detection algorithm, surface properties from collocated European Centre for Medium-Range Weather Forecasts (ECMWF) reanalysis data, collocated cloud proprieties and optical depths from the Moderate Resolution Imaging Spectroradiometer (MODIS) on Aqua, and RO fluxes and heating rates, described further in Section 2.2.

2.1.2 CALIPSO/CALIOP

CALIPSO was launched along with CloudSat and entered into the A-Train constellation in May 2006. The satellite currently resides between CloudSat and Aura, trailing CloudSat by about 12.5 seconds. The satellite is operated by NASA, in collaboration with CNES. The satellites primary instrument is the near-nadir pointing Cloud-Aerosol Lidar with Orthogonal Polarization (CALIOP). The lidar is used to observe the vertical distribution cloud and aerosol particles in our atmosphere. CALIPSO also contains two other instruments: the Imaging Infrared Radiometer (IIR), and the Wide Field Camera (WFC). These instruments provide additional swath data and are centered on the lidar footprint.

The data used in this research comes from the CALIOP instrument. CALIOP is two-wavelength polarization-sensitive lidar used to detect clouds and aerosols in

the vertical. Three channels are measured on CALIOP, the first being 1064 nm backscatter intensity and also two channels that measure the orthogonally polarized components of the 532 nm backscattered lidar signal. CALIOP has a horizontal resolution of 335 m and a vertical resolution of 30 m, although this resolution may decrease in certain products due to horizontal averaging to detect weak signals. Because of its high resolution and high sensitivity to particles in the atmosphere, measurements from CALIOP are useful to match with CloudSat, to get a larger range of cloud detection and include additional information of aerosols unseen by CloudSat.

Data from CALIPSO were obtained from the CloudSat DPC as well as the Atmospheric Science Data Center (ASDC). Cloud and aerosol properties are obtained from the Level 2 cloud layer product and aerosol layer product (CAL_LID_L2_05kmCLay/CAL_LID_L2_05kmALay). Level 1 backscatter products are also used to find properties of thin clouds (CALIPSO_L1B_ValStage1).

2.1.3. AQUA/MODIS/CERES

Aqua was launched in May 2002 and is the first satellite launched by NASA in the A-Train. Each instrument on Aqua serves a different purpose and help make a strong package for observing our Earth's systems. Aqua contains six different instruments which are: the Atmospheric Infrared Sounder (AIRS), the Advanced Microwave Sounding Unit (AMSU-A), the Humidity Sounder for Brazil (HSB), the Advanced Microwave Scanning Radiometer for EOS (AMSR-E), Clouds and the

Earth's Radiant Energy System (CERES) and MODIS. Aqua is also used in tangent with CloudSat and CALIPSO as it flies in orbit ahead of CloudSat by about one minute.

In this research MODIS and CERES sensors are used to provide cloud properties and are used to verify our flux products. MODIS obtains cloud properties from 6 spectral bands between 0.405 and 14.385 μm, which vary in horizontal resolution from 250 m to 1 km. Using the spectral bands observations of the land, oceans and the atmosphere are calculated. In this research we use MODIS 06 data to find cloud properties (i.e. cloud drop size or cloud optical depth). The CERES instrument was constructed based on the ERBE (Earth Radiative Budget Experiment) scanning radiometer design, but with higher spatial resolution and improved calibration. The instrument uses three channels to measure the shortwave radiation from reflected sunlight, infrared radiation in the 8-12 μm atmospheric water vapor window, and radiation wavelengths from 0.3 to 100 μm. The CERES instrument was created to provided a long term database of TOA fluxes, increase the accuracy of TOA and BOA fluxes, provide a long term estimate of the ERB, and provide cloud properties consistent with the observed radiative fluxes.

2.1.4. ISCCP

Although the International Satellite Cloud Climatology Project (ISCCP) is not associated with the A-Train, it still is a tool that can be used to check the consistency of the results. ISCCP began in 1983 and has used polar and geostationary satellites

to construct 2.5° x 2.5° latitude/longitude datasets. These datasets include cloud cover and radiative properties on the Earth. ISCCP was created to provide infrared and visible radiance data sets to derive radiative properties of the atmosphere to be used in modeling and to help further the understanding of our ERB. The fluxes from the global surface and atmospheric radiative flux products are used to compare our TOA and BOA atmospheric fluxes.

2.2 Data Description

2.2.1 2B-GEOPROF

The 2B-Geoprof product can be considered as CloudSat's cloud mask and is created by the Geometrical Profile algorithm along with MODIS and ECMWF auxiliary files. The files are used to estimate the radar reflectivity factor for which a significant radar echo is present (Stephens et al, 2001). The strength of the echo is defined in the products CPR Cloud Mask that varies in value from 0-40. Values over 20 can be considered an echo, which may be a cloud, while below 20, can be considered a very weak return or a false return. The 2B-Geoprof cloud mask is an excellent way to detect clouds in the atmosphere, but in return the CPR on CloudSat is not able to detect all clouds. Due to the high return power from the Earth's surface, many clouds below 1 km are unable to be detected from the surface return. This 'ground clutter' causes detection issues with low stratiform clouds as well as finding a cloud base below 1 km. Clouds that are below -30 dBz are also undetected

by the CPR and are missed in the 2B-Geoprof cloud mask. This does include some low clouds, but mostly involves high sub-visible thin cirrus clouds.

2.2.2 2B-CWC-RO

CloudSat's product for finding water content and cloud properties is the Radar-Only Cloud Water Content Product (2B-CWC-RO). This product gives information on cloud liquid and ice water content in the vertical by creating a combined profile for liquid and ice based off of separate retrievals. Each retrieval is completed with the assumption that the profile is composed of either only liquid water or only ice. Water contents are calculated using,

$$LWC = \int_0^\infty \rho_w N(r) \frac{4}{3} \pi r^3 dr, \tag{2.1}$$

where ρ_w is the density of water, N(r) is a logarithmic drop distribution, and r is the drop radius. Ice contents are calculated in a similar fashion,

$$IWC = \int_0^\infty \rho_i N(D) \frac{1}{6} \pi D^3 dD \tag{2.2}$$

Where ρ_i is the density of ice, N(r) is a logarithmic distribution of ice, and D is the diameter of an equivalent mass ice sphere. Using this product the water content needed to calculate fluxes and heating rates are obtained. This product however does tend to fail under areas of large drops, such as precipitation making it necessary to estimate water contents in these areas.

2.2.3. 2B-Tau

CloudSat's Level 2 optical depth product is created to estimate cloud optical depth values as well as their effective radii. Optical depth and effective radii are calculated by using MODIS TOA upwelling reflectivity in several channels, as well other data including geolocation, meteorological parameters, and surface albedo. Radar reflectivity from the CPR provides the data to find the cloud distribution in a column, and helps to calculate a priori values for the optical depths. Data used from this product are limited to daylight hours, where MODIS measures reflected solar radiation from the Earth.

2.2.4. 2B-FLXHR

The Level 2 2B-FLXHR (Fluxes and Heating Rates) CloudSat product was introduced to give the user vertical distributions for atmospheric fluxes and heating rates due to clouds in the atmosphere (L'Ecuyer, 2007). Its main inputs are the liquid and ice water contents that are derived by the 2B-CWC product as well as atmospheric variables taken from ECMWF reanalysis data. The product does make assumptions in case the 2B-CWC product fails to make a solution. This happens in many cases of precipitation, where a large LWC is assumed, making flux measurements more uncertain. The product is a CloudSat only product so the fluxes and heating rates are calculated only for clouds seen by the CPR on the CloudSat satellite.

The fluxes derived in this product are broadband and both upward and downward fluxes throughout the atmosphere are provided. The fluxes along with the cloud properties are used to then calculate the heating rates for each radar bin. The products are calculated by inserting the variables into a two-stream radiative transfer model. The model consists of 18 individual bands of which 6 are in the shortwave and 12 are in the longwave. The optical properties, derived from the atmospheric variables, in the model are used to calculate the reflectance, transmission, and the radiative source. The optical properties are the optical depth, τ, the single scattering albedo, ω_0, and the asymmetry parameter, g. The atmosphere is then divided into multiple slabs vertically in the atmosphere, and each flux and heating rate are found from these slabs. Once the reflectance, transmission, and radiative source are found the model is ran and solved by using equations 2.3 and 2.4.

$$F_a^+ = RF_a^- + TF_b^+ + \Sigma^+ \tag{2.3}$$

$$F_b^+ = RF_b^+ + TF_a^- + \Sigma^- \quad , \tag{2.4}$$

where the F^+ indicates a flux that is going in the direction of "b->a", the F^- indicates a flux going in the "a->b" direction, R is the reflectance, T is the transmission, and Σ is the radiative source properties. Given the fluxes of F^-_a and F_b^+ the other two fluxes may be calculated. More detailed description of the model can be found in Section 3.4.

2.2.5. CAL_LID_L2_05kmCLay/CAL_LID_L2_05kmALay

CALIPSO's 5 km cloud and aerosol products provide retrievals of cloud and aerosol properties. With a recent release in the new Version 3 algorithm of CALIPSO's products we are able to use them to make a cloud and aerosol mask as well as find properties of certain clouds. The product is averaged over 5km, but has varying horizontal resolution from 333 m to 80 km. Cloud and aerosol are detected and separated by observing the magnitude and variation of the CALIOP backscatter at 532 nm and 1064 nm wavelengths. Besides cloud and aerosol layer detection, this product also gives information on the optical depths of the cloud and aerosol layers. This is not the most accurate product for all situations as there are times when the lidar becomes fully attenuated and therefore the entire cloud is not observed. For FHR-A this product is used for the optical properties of thin sub-visible cirrus and aerosol layers, as this is currently best available product for this data. More information on the layer detection and properties can be found in Vaughan et al. (2005).

2.2.6. CALIPSO_L1B_ValStage1

Data from the CALIOP Level 1B data contains calibrated and geolocated high-resolution (333m) single shot lidar profiles. These profiles are created from backscatter measured at both 532 nm and 1064 nm wavelengths. The 532 nm

attenuated backscatter profiles are used to help find optical properties of thin sub-visible cirrus clouds.

2.2.7. MODIS 06

Data from MODIS 06 (King et al., 1997) is a level 2 product from the MODIS sensor aboard the Aqua satellite. The MODIS 06 product uses the spectral bands in the visible (0.645 um) and near-infrared (1.64, 2.13, and 3.75 um) to calculate daytime SW cloud retrievals, and then thermal bands from 8.55 to 14.235 um to find cloud top properties. Cloud property retrievals include the particle phase, cloud fraction, cloud water path, optical depth, and the effective radius. The optical depths and effective radii are intended to be from clouds that are plane parallel liquid water clouds. All clouds have been screened by Ackerman et al. (1997) and information of particle phase is taken from Menzel and Strabala (1997). Optical depths and the effective particle radius reported by MODIS data are created by starting with the reflective intensity field (radiance), derived from a radiative transfer model. When the atmospheres optical thickness is large enough the reflection properties of optically thick layers will depend on a scaled optical depth, albedo of the underlying surface, and the effective radius. The algorithm assumes that the reflection is not dependant on the cloud drop size distribution of a cloud, but that the effective radius of a cloud is more primarily depended on. A reflectance function is then integrated over wavelength and weighted by the band's spectral response and the incoming solar flux. The reflectance function is,

$$R(\tau_c, r_e; \mu, \mu_0, \phi) = \frac{\int_{\lambda} R^{\lambda}(\tau_c, r_e; \mu, \mu_0, \phi) f(\lambda) F_0(\lambda) d\lambda}{\int_{\lambda} f(\lambda) F_0(\lambda) d\lambda} \quad , \qquad (2.5)$$

where τ_c is the cloud optical thickness, r_e is the effective radius, μ is absolute value of the cosine of the solar zenith angle θ_0, μ_0 is the cosine of the solar zenith angle, F is the incoming solar flux, φ, is the relative azimuth angle, λ is the wavelength, R_λ is the reflectance as a function of wavelength, and f is the band's spectral response. The inverse of the reflectance produces the cloud properties of τ_c and r_e, which are calculated by comparing the measured reflectance via a lookup table of values.

2.2.8. CERES FLASHFlux

Data from CERES also serves as an independent test of the fluxes from this study. CERES provides high-resolution cloud and radiative data to provide a long-term climatology of its products. The issue is that to insure data quality, the CERES data generally must go through thorough processing, delaying the release of the data many months. The Fast Longwave and Shortwave Radiative Flux (FLASHFlux) product derived from CERES data is a product that was designed to overcome this issue producing surface and top of atmosphere fluxes in almost real time (Stackhouse et al., 2006). The data provides surface and top of atmosphere outgoing and incoming radiation at a 1° x 1° degree resolution, and is available within a week of the CERES overpass. The ability to process so quickly comes from using only a part of the CERES processing system, combining CERES and MODIS data

to obtain cloud information, then obtaining meterological information of the atmosphere from NASA's Global Modeling and Anaysis Office (GMAO), Goddard Earth Observatory System (GEOS), and the Stratosphere Monitoring Ozone Blended Analysis (SMOBA) product from NCEP. The products are processed through an angular distribution model and radiative transfer model to obtain the FLASHFlux (SSF) dataset.

2.2.9. ISCCP FD

One of the longest and most homogeneous global radiative flux climatologies comes from ISCCP's FD product. The product was started in 1983 and continued through December 2007. The product provides TOA and surface fluxes derived from a combination of NASA GISS climate Global Circulation Model (GCM) and a collection of global satellite data to describe cloud (Zhang and Rossow, 1995). Like all other ISCCP products the FD product is provided daily at 3-hour intervals and are binned into 2.5° x 2.5° resolution globally. Meteorological variables for the data input are derived from the TIROS satellite for temperature and humidity, ozone data from the Total Ozone Mapping Spectrometer (TOMS), cloud layers from rawisonde humidity profiles, and land albedo and emissivity from NASA GISS. Climatologies are used to obtain information on cloud particle size, stratospheric properties, and diurnal variations of surface temperature. The inputs of these data are combined into a radiative transfer model, which produces the ISCCP FD dataset.

3. METHODOLOGY

3.1 Cloud Detection and Properties

For the detection of clouds, collocated 2B-Geoprof and CAL_LID_L2_05kmCLay data were used. The combination of these datasets gives a result quite similar to the 2B-Geoprof-Lidar product from CloudSat's DPC (Mace et al., 2008), but with the release of Version 3 of CALIPSO data, the new 2B-Geoprof-Lidar dataset had yet to be reprocessed during the span of this research. Since the reprocessing was not completed in the timeframe of this research and, in order to use the most current lidar backscatter data, a new cloud mask was created using the new lidar data.

Clouds detected by CloudSat were identified by using the CPR Cloud Mask in the 2B-Geoprof product. Values of 20 or higher were used in the discrimination of cloud and any values below this were ignored. To detect clouds unseen by CloudSat the Vertical Feature Mask (VFM) in the CAL_LID_L2_05kmCLay is used for cloud detection. To collocate the CALIPSO data to CloudSat, the CPR footprint is matched to the 5 km and 333 m footprints from CALIPSO. Each CloudSat granule requires three half-orbit files (day/night) from CALIPSO to ensure full coverage in the CloudSat file. Figure 3.1 is a simple illustration of how the nearest point between CloudSat and CALIPSO is determined. Within each granule, the 1.4 km footprint

from the latitude and longitude locations along the 2b-Geoprof (blue circles represent CloudSat footprint) were matched to the nearest locations (5 km grid) obtained from CAL_LID_L2_05kmCLay-Prov-V3-01 (red circles represent the 5 km horizontal sampling from CALIPSO) by calculating great circle distances between successive profiles. Because the lidar samples the atmosphere at 333 m increments, averages of 15 shots are used to construct aerosol and cloud layers on a 5 km horizontal grid (CALIPSO Quality Statements Lidar Level 2 Cloud and Aerosol Layer Products Version 3.01). For the 5 km layer products, three latitude/longitude values are reported: the time for the first pulse included in the 15 shot average; the time for the final pulse; and the time at the temporal midpoint (i.e., at the 8th of 15 consecutive laser shots). The location of the temporal midpoint (for the 5 km grid) is used for nearest neighbor matching to the CloudSat orbit. Because CloudSat samples the atmosphere more frequently (1.4 km) than the consecutive laser shot averages obtained from CALIPSO, multiple CloudSat observations (typically 3 bins) coincide with the observations from CALIPSO at 5 km horizontal resolution. The 333 m layer product latitude and longitude positions are also matched to the CloudSat orbit.

The VFM distinguishes whether CALIPSO detected cloud or aerosol. If clouds were detected, and the feature flag labeled the cloud detection and aerosol/cloud distinction as high confidence, the cloud flag was used in the feature mask. The reason for the conservative use of the high confidence flags in the detection is to try to eliminate any errors in the discrimination of cloud. This occurs in CALIPSO Cloud and Aerosol Discrimination (CAD) score of above 70, where 100 is considered most

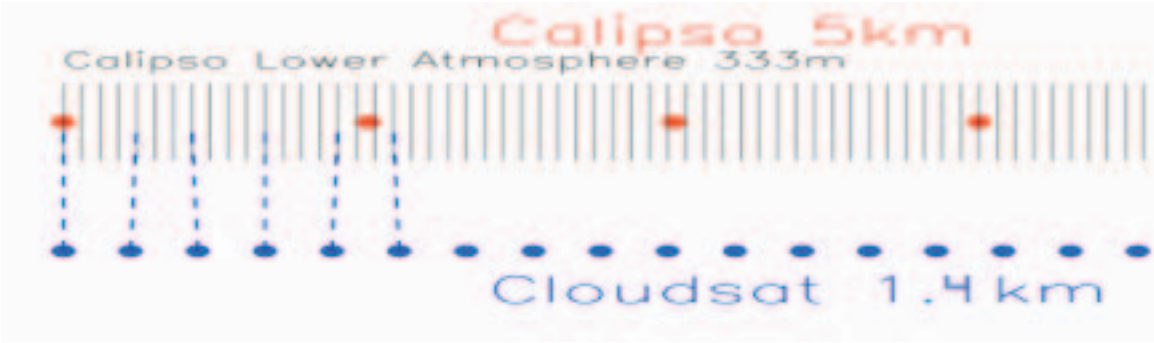
Calipso 5km
Calipso Lower Atmosphere 333m
Cloudsat 1.4km

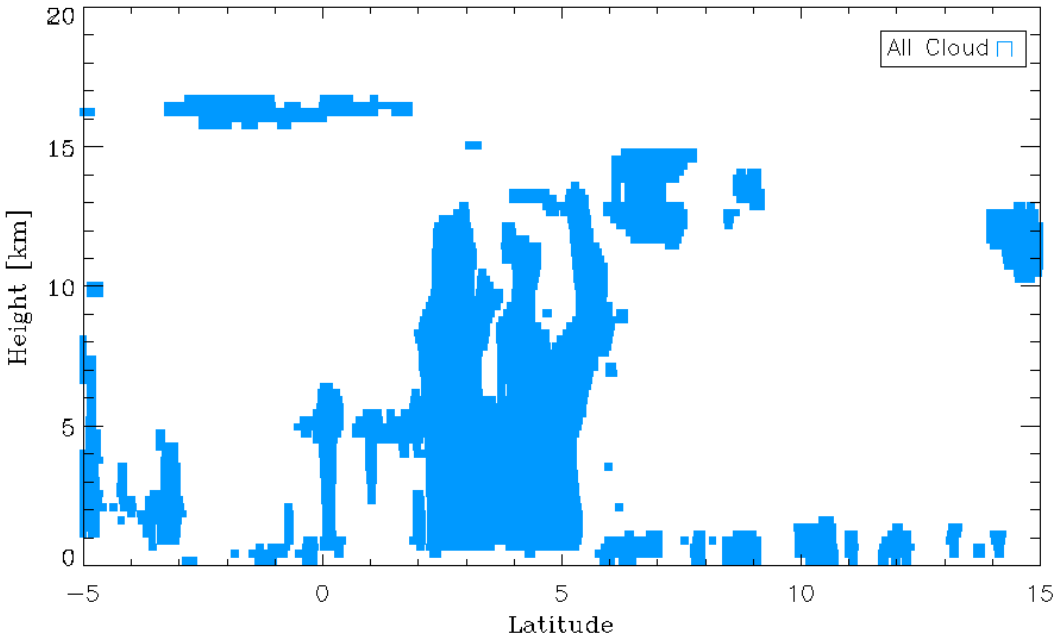

(a)

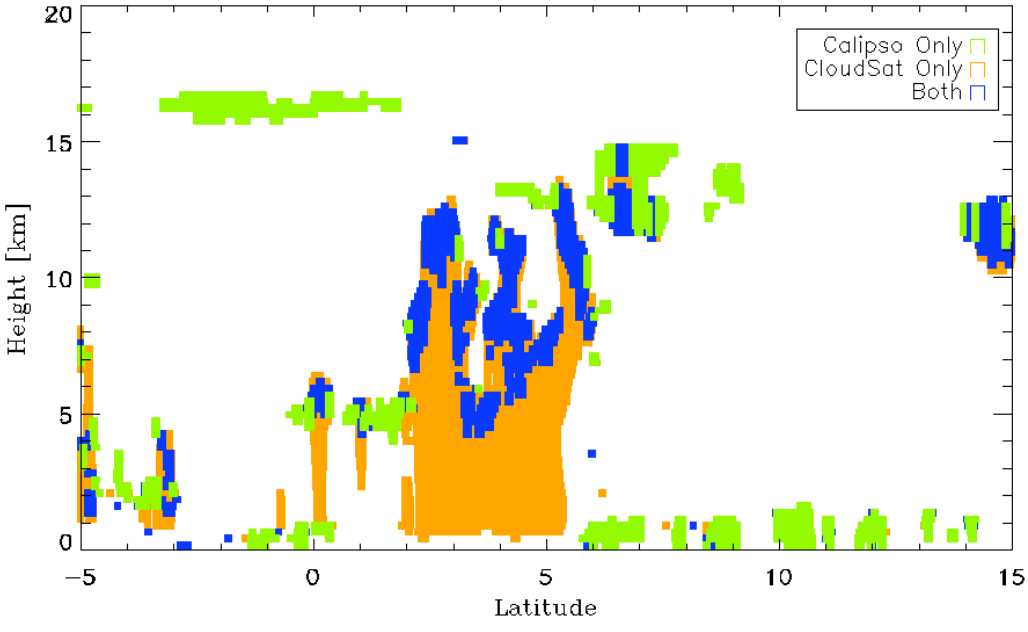

(b)

Figure 3.2. An example of the combination of CloudSat and CALIPSO used to create a cloud mask. The overall cloud mask is shown (a) as well as split by sensor (b). Clouds seen only by CloudSat are shown in orange, only by CALIPSO are shown in green, and clouds detected by both satellites are shown in blue.

With the positions of the clouds determined the properties of the clouds are then deduced. The properties are the LWC and IWC of the cloud, and the radius of liquid drop or ice crystal. These properties are inputted into each 240 m vertical CloudSat bin and in turn are used as input into the radiative transfer model (see Section 3.4). Cloud properties for RO clouds are taken from the 2B-CWC-RO product from CloudSat. This product contains the LWC and IWC based off of corresponding effective radii for each bin. The water contents in the product are calculated using Mie Theory while the ice contents are calculated using anomalous diffraction theory-based parameterizations from Stephens et al. (1990) and Mitchell et al. (1996). In the case that 2B-CWC-RO does not converge to an answer in LWC we must define the properties of the cloud manually. These situations tend to occur in areas where there are large amounts of ice over the liquid water, coincident with precipitation (see Section 3.3). Figure 3.3 shows an example of the LWC and IWC products, CPR reflectance, the CPR Cloud Mask, and also contains areas where the LWC does not converge to an answer.

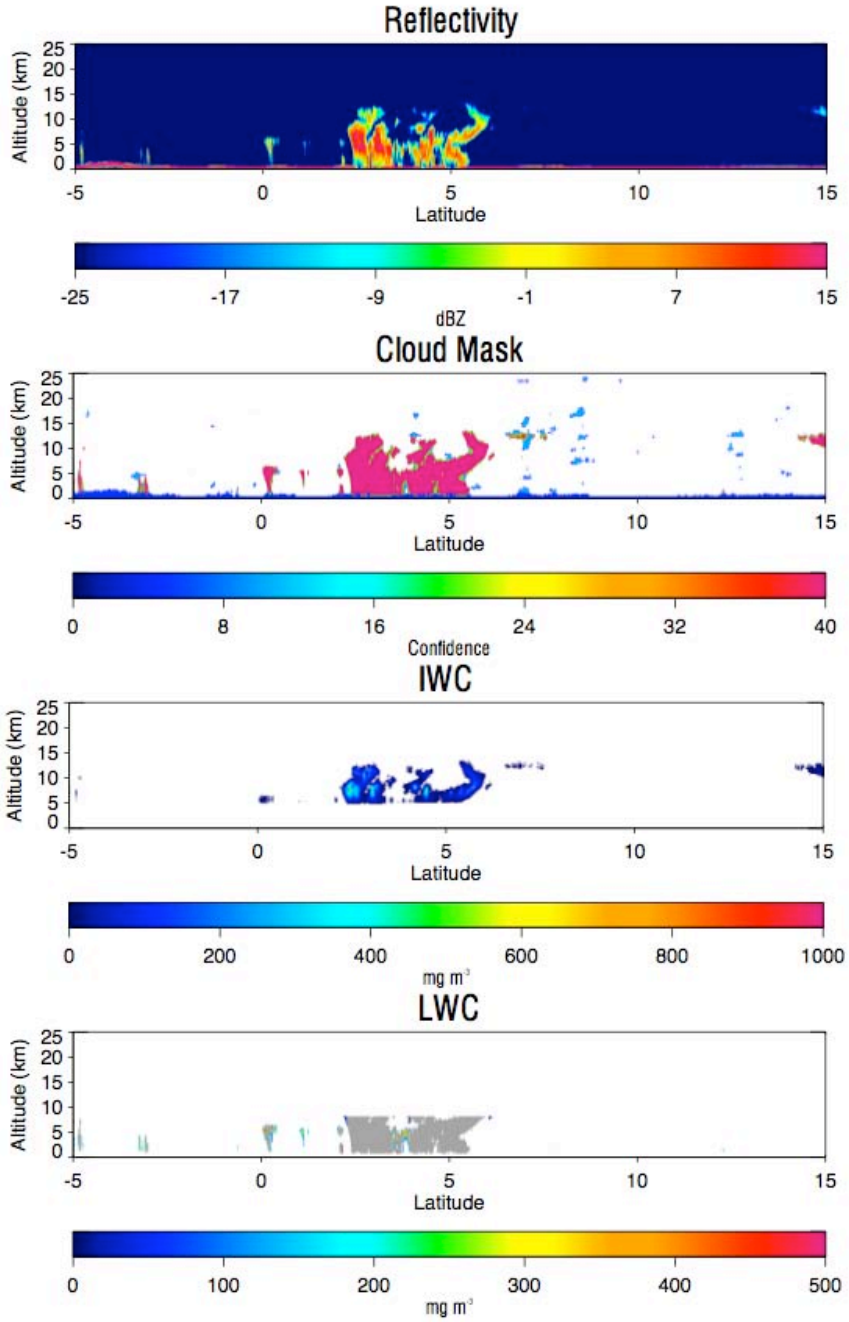

Figure 3.3. Inputs to the algorithm including the calibrated reflectivity, 2B-GEOPROF cloud mask, IWC, and LWC. Areas in red and pink indicate high confidence in cloud detection. The gray shaded areas in LWC indicate parts of clouds where the 2B-CWC product did not converge to an answer.

Sub-visible cirrus clouds also usually go unseen by CloudSat as they usually typically fall below the -30 dBz minimal detectable range of the CPR. If CALIOP

detects a cloud above the freezing level and CloudSat does not detect it, it is flagged as a possible cirrus cloud. To calculate the properties of these cirrus the optical depth of the cloud is calculated by use of a lidar-transmission method similar to those used in Comstock and Sassen (2001), Lo et al. (2006) and Haladay and Stephens (2009). To start, the CALIPSO_L1B_ValStage1 total attenuated backscatter data is used to create a vertical profile of the backscatter. Because of the high sensitivity of the lidar, surrounding profiles must be averaged to create a smoother profile, so therefore a 5 km average is used. Figure 3.4 will be used to help visualize the process of finding the optical depth of the cirrus. The CALIPSO data has a horizontal resolution of 333 m; Therefore, seven lidar profiles on each side of the current data point are averaged to make a profile with less noisy features. The blue line in Figure 3.4 is the measured backscattered lidar signal from CALIOP. Next, using pressure and temperatures from the ECMWF-AUX product from the CloudSat DPC the data is interpolated to the heights of the lidar profile to create a reference Rayleigh backscatter profile, which can be estimated as an exponential fit. This fit is the green line in Figure 3.4, and is in the form,

$$\beta_{Ray}(z) = \frac{\sigma_m}{k}\left(\frac{P_o}{T_o}\right)e^{-z/H} \approx A_{Ray}e^{-z/H} \tag{3.1}$$

where σ_m is the Rayleigh backscatter cross section, k is the Boltzmann constant, P is the pressure, T is the temperature, and H is the cloud scale height. This exponential matches the measured backscatter near the top of the profile. As the lidar beam passes through the cirrus, the cloud causes a reduction in the backscatter due to extinction. This allows us to use the reduction in extinction to find the bottom of the

cirrus. To find the bottom of the cloud, we take an exponential fit of the entire measured backscatter profile, and where the backscatter crosses the exponential fit below the large cloud signal is where the cloud bottom is located. From the bottom of the cloud we can make another exponential fit in the form,

$$\beta_{Meas}(z) = A_{Meas} e^{-z/H} \tag{3.2}$$

Using a ratio of the coefficients A_{Ray} and A_{Meas} we can get an estimate of the optical depth of the cirrus clouds. This method is a measure of the two-way transmission,

$$\frac{A_{Meas}}{A_{Ray}} = e^{-2\tau_{cloud}} \quad . \tag{3.3}$$

Using this ratio we calculate the optical depth and then can find the IWC of the cloud through a relationship defined by Stephens (1978),

$$\tau_{cloud} = \frac{3}{2} \frac{LWC}{\rho_{ice} r_e} \Delta z \tag{3.4}$$

where ρ_{ice} is the density of ice r_e is the radius of an equivalent mass sphere of ice, and Δz is the thickness of the layer. The effective radius for the cirrus clouds are set at 30 um, which is typical of cirrus observed by the CPR and consistent with the properties used in 2B-FLXHR from CloudSat.

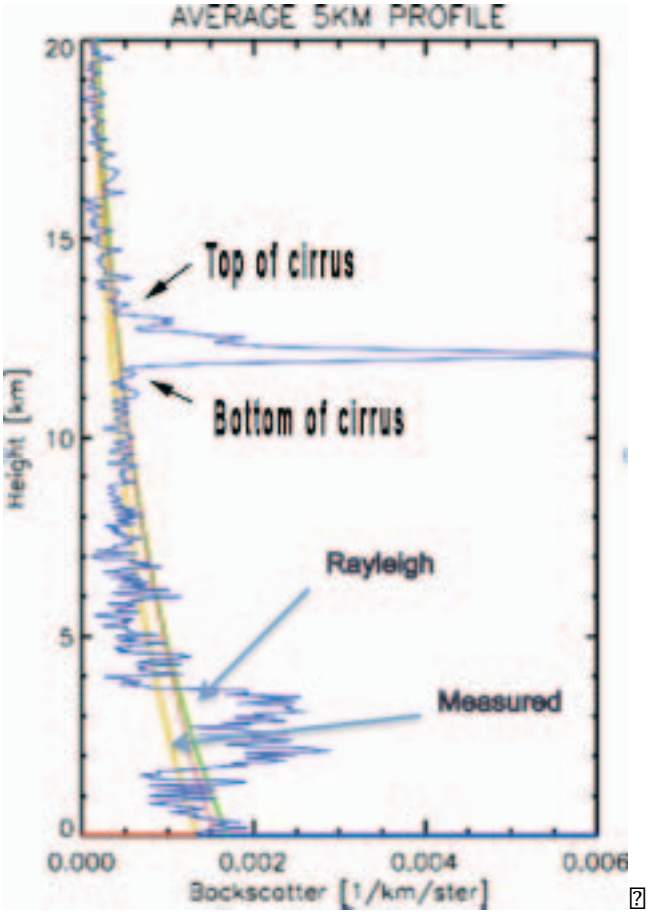
AVERAGE 5KM PROFILE
Top of cirrus
Bottom of cirrus
Rayleigh
Measured
Height [km]
Backscatter [1/km/ster]
0
5
10
15
20
0.000
0.002
0.004
0.006

from each CALIPSO point. Figure 3.5 shows a scatter plot of the differences of the products in relation to their distance from the CloudSat point. This scatter plot shows that the difference in optical depth does not vary with distance. The average difference is 0.006 with an RMS error of 0.13. Much of the scatter in Figure 3.5 is due to high measurements in optical depth from CALIPSO, putting the most used values within 0.12. If the lidar-transmission method fails to calculate a value, and CALIPSO does not have a solution, or has values too large (optical depths too high and deemed not physical), then a climatological value is used. The properties for this are the same as used from L'Ecuyer et al. (2008) having an effective radius of 30 um and a IWC of 1.5 mgm^{-3} and is independent of cloud temperature.

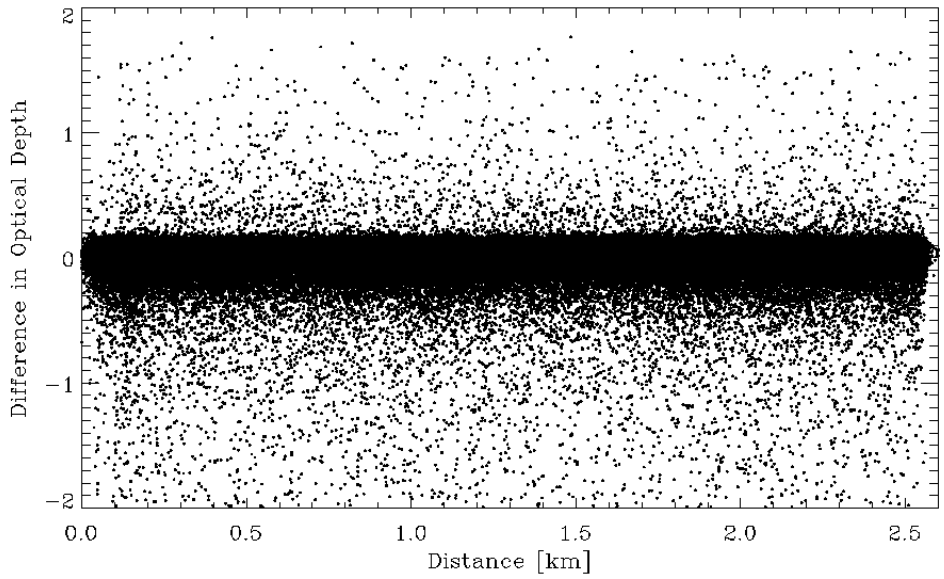

Figure 3.5. Difference in calculated optical depth from the lidar-transmission method with CALIPSO's OD product.

Undetected low clouds in the atmosphere pose a different problem for this flux and heating calculation. Low clouds that are missed in the 2B-FLXHR product

causes a larger LW flux to space, and more SW radiation from the sun reaches the surface. Slingo (1990) cites the importance of low-level clouds on the ERB and Hartmann et al. (1992) states that low clouds reduce our ERB by about 15 Wm^{-2} globally, so it is important to make sure we capture them in our algorithm. These clouds, if missed by CloudSat, are found by using the CAL_LID_L2_05kmCLay dataset. In order to assure that the low clouds are not a false detection or misclassified we only use low level clouds that are defined as high confidence in the CALIPSO VFM. In order for the clouds to be considered low level clouds, they must be below the freezing level and only seen by CALIPSO. Properties for these clouds are then taken from MODIS data. If MODIS data are available then the optical depths and the effective radii will be used to find the LWC. The LWC is found in the same way using Equation 3.4, where the IWC is now the LWC and the density of ice is switched to the density of water. If MODIS data are unavailable for a low cloud, then a climatology value is used instead. For the LWC, clouds below 1 km are given a value of 50 mgm^{-3} based from the cloud climatology from Miles et al (2000). Above 1 km clouds are given a value of 120 mgm^{-3} based from low clouds found at CloudSat's minimum detectable signal of -30 dBz. The effective radius of the cloud is averaged from MODIS. Figure 3.6 shows the curve of cloud drop effective radius from the 2.1 um channel of MODIS over the year 2007. Clouds used for this average had to be above 273K and below 2km to ensure they are liquid clouds only. Averaging this curve gives us an effective radius of nearly 13 um, which would give a cloud of 1km in thickness an optical depth of ~6.

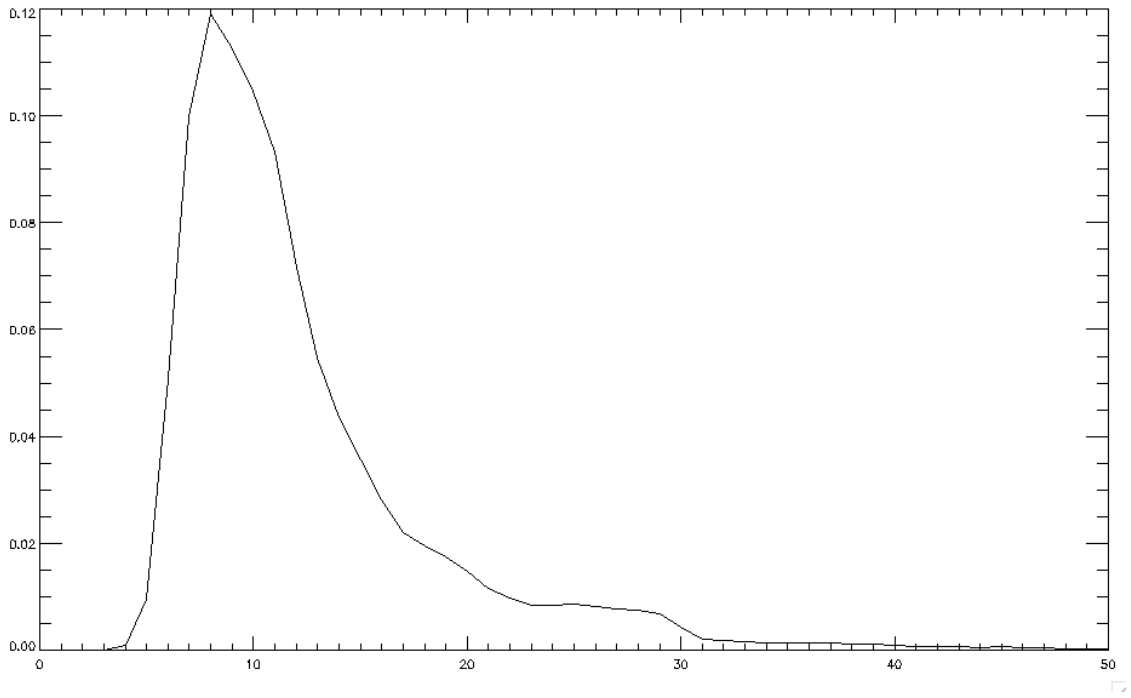

Figure 3.6. Frequency of cloud drop effective radius taken from the MODIS 2.1 um channel.

These prescribed properties for both high thin cirrus as well as low clouds undetected by CloudSat are used to fill the gaps in the 2B-CWC product. Figure 3.7 shows the products again but this time with the added data. Reflectivity remains unchanged as we do not have reflectivity measurements from the CPR of the new data. The CPR Cloud Mask has been updated to include high confidence clouds seen by CloudSat in pink, and now our high confidence clouds seen by CALIPSO in red. Where the CALIPSO clouds have been added in the cloud mask, you can see in the corresponding areas in the IWC and LWC. In the IWC the sub-visible cirrus can be seen with a lower ice content of about 125 mg/m^3. Low-level clouds are also seen in the LWC panel, with low-level clouds having similar LWC than the ones seen by

CloudSat. Areas that are still shaded gray are due to precipitation and are discussed later in Section 3.3.

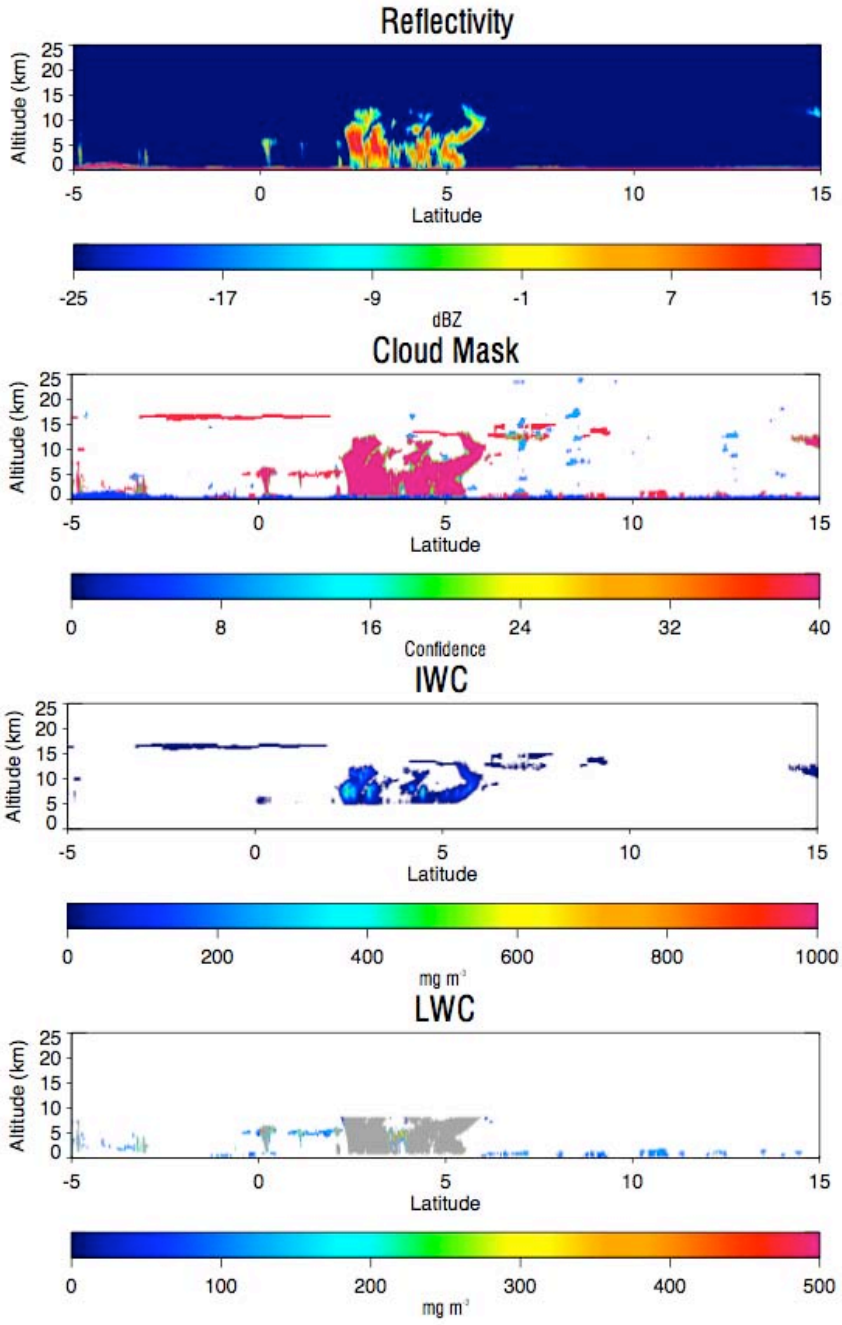

Figure 3.7. Inputs to the algorithm including the calibrated reflectivity, 2B-Geoprof cloud mask, IWC, and LWC. Areas in red and pink indicate high confidence in cloud detection. The gray shaded areas in LWC indicate parts of clouds where the 2B-CWC product did not converge to can answer.

3.2 Aerosol detection and properties

For the detection of aerosol, data from CloudSat and CALIPSO taken from the collocated 2B-Geoprof and CAL_LID_L2_05kmALay data are used. By incorporating the VFM in the CALIPSO data we are able to find the heights of the layer tops and bottoms of the aerosol. The layer heights were then adjusted to the CloudSat resolution in the same manner used to create the cloud mask in Section 3.1. In order to avoid confusion between cloud and aerosol detection, only aerosol layers labeled as high confidence in the CALIPSO feature mask were included in the aerosol mask. This occurs in CALIPSO Cloud and Aerosol Discrimination (CAD) score of above 70, where 100 is considered most confident. Also, any aerosol layer that occurs under a cloud layer is not used in this study to continue to avoid possible false aerosol detections by CALIPSO. Because there is no vertical information on aerosols aboard any other satellite in the A-train, the locations and properties of aerosols taken from CALIPSO are considered truth.

Once the location of the aerosol layers are located, the aerosol type and can also be extracted from the CALIPSO VFM. Each aerosol type is distinguished by using the CALIPSO aerosol models, which are based of the cluster analysis of the AERONET dataset. The characteristics of the specific aerosol types are grouped together based off of the instantaneous observed physical and optical properties of the aerosol. The basics of the selection will be described in the following, but more detailed information on the aerosol model can be found in Omar et al. (2009). Aerosol characteristics are determined using both information from the CALIPSO lidar

backscatter, and information from AERONET analysis, to find aerosol type and also optical properties which are found by using an assumed extinction-to-backscatter ratio, now referred to as S_a. In order to determine aerosol type the integrated attenuate backscatter (532 nm), volume depolarization ratio, and surface types are used. Using thresholds for each aerosol type along with the underlying surface where the data was taken, the CALIPSO model is able to discriminate between 6 aerosol types: Dust, polluted dust, continental, polluted continental, biomass burning (smoke), and marine aerosols. The new aerosols can be found with the cloud classification in Figure 3.8.

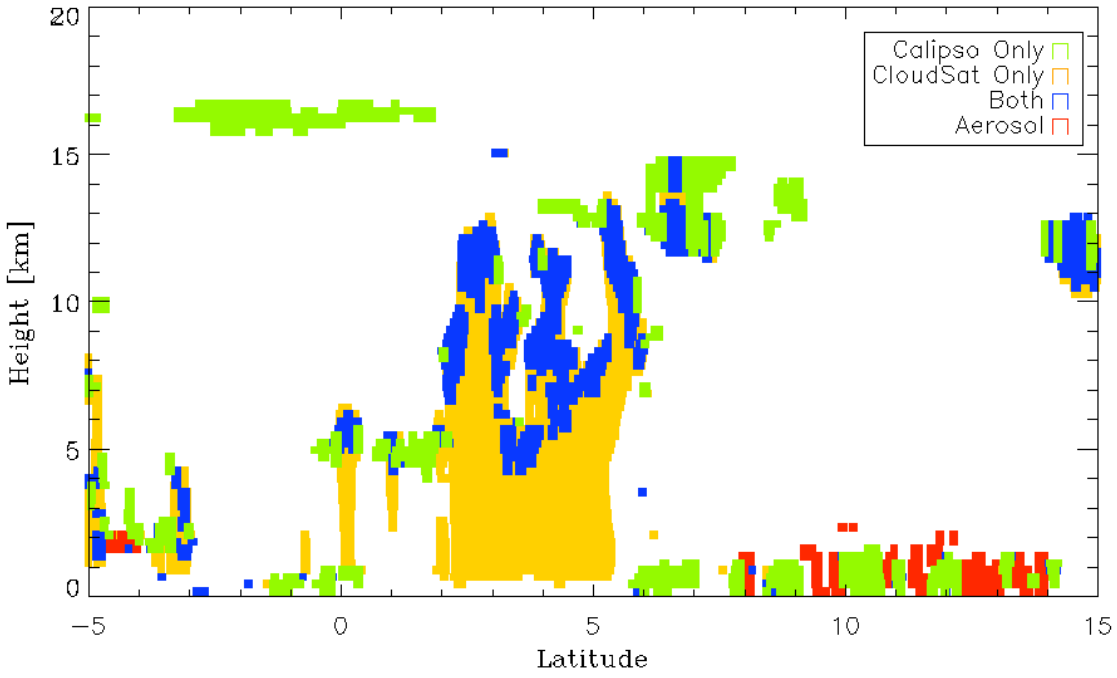

Figure 3.8. An example of the CALIPSO aerosol detection scheme. The aerosol along with cloud can be seen in the different colors and are labeled in the image.

In order to find the optical properties of each aerosol, the CALIPSO model then uses information from models and observations to determine the extinction

properties of each layer. Values of S_a, taken from field measurements, for each aerosol type can be compared with the lidar ratios found in AERONET models. For the CALIPSO model, three of the AERONET models are used to represent biomass burning (smoke), polluted continental, and polluted dust aerosols. Marine and clean continental aerosols are derived based upon the size distributions of the aerosols along with the complex refractive indices, or by adjusting aerosol model parameters to find S_a. Values for dust were taken from Kalashnikova and Sokolik (2002). Values of S_a for each aerosol type are summarized in Table 3.1, and the volume distributions of the aerosols modeled are illustrated Figure 3.9.

	S_a at 532 nm (Sr)	S_a at 1064 nm (Sr)
Dust	40	55
Smoke	70	40
Clean Continental	35	30
Polluted Continental	70	30
Clean Marine	20	45
Polluted Dust	65	30

Table 3.1. This table shows the values of the extinction-to-backscatter ratio, S_a, for each aerosol type. Values of S_a are given in Steradians.

Once S_a is established for each aerosol type, the optical properties can then be calculated for each aerosol layer using the radius of the particles, S_a, and the aerosol type. The optical depth is calculated from these properties, which are used to find other aerosol properties that are necessary input into a radiative transfer model.

The same CALIPSO aerosol types can also be matched to SPRINTARS aerosol model. The optical depth for each aerosol layer, given by CALIPSO, can be compared with the optical properties from that of SPRINTARS (Takemura et al., 2002). Using the mean radii from the CALIPSO model (Figure 3.9), we are able to compare the optical depths at each radius from CALIPSO with that of the SPRINTARS model. Optical properties included in SPRINTARS include the optical depth, single scattering albedo, and asymmetry parameter for an individual aerosol type and radius. Aerosol optical properties from this model for each variable come from d'Almeida (1991) and WCP-55 (1983). Using the 532 nm aerosol optical depth from CALIPSO and the mean radius from the CALIPSO aerosol size distribution, we can compare the closest radius and optical depth in SPRINTARS to find to matching single scattering albedo, and asymmetry parameter. The aerosol optical properties in the visible band (0.20-0.69 μm) are contained in Table 3.2. The table includes the SPRINTARS radii matched from CALIPSO's mode radius from the log-normal size distribution (Figure 3.9), the derived asymmetry parameter, and derived single scattering albedo.

	Radius [μm] (Fine/Coarse)	ω	g
Dust	0.2/2.84	0.99	0.76
Polluted Dust	0.21/3.16	0.96	0.39
Continental	--/2.63	1.0	0.74
Polluted Continental	0.14/3.55	0.96	0.35
Marine	--/1.22	0.99	0.54
Smoke	0.14/3.73	0.44	0.14

Table 3.2 The radii from CALIPSO for both fine and coarse modes, single scattering albedo, and asymmetry parameter for each aerosol species in the visible band.

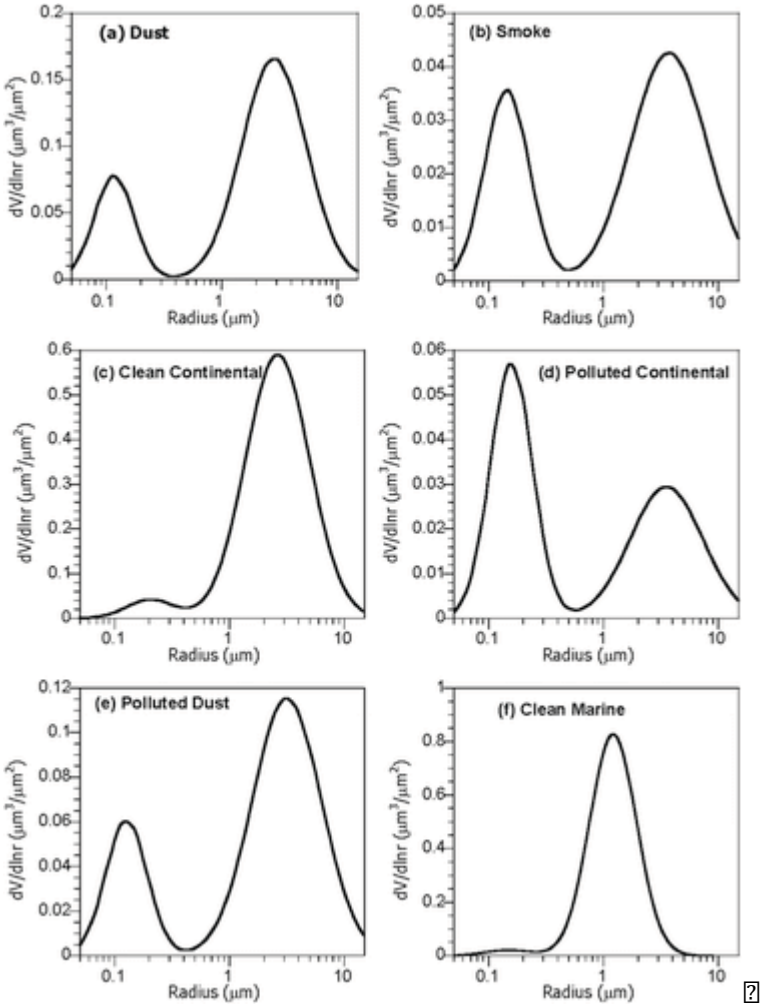
(a) Dust
(b) Smoke
(c) Clean Continental
(d) Polluted Continental
(e) Polluted Dust
(f) Clean Marine
dV/dlnr (μm³/μm²)
Radius (μm)

c jc

only clouds in which the cloud base is below the freezing level within 1 km of the surface are used. These constraints are placed for the cases where precipitation does not reach the ground, we currently do not have a method to find the precipitation base. Therefore, if the 2B-CWC algorithm fails to converge to an answer and precipitation is not either found, or not reaching the ground, we cannot process the pixels. For pixels containing precipitation that meet the constraints we are able assign properties of the cloud and rain drop sizes and liquid water contents. An example of the precipitation added into an area of cloud can be seen in Figure 3.10.

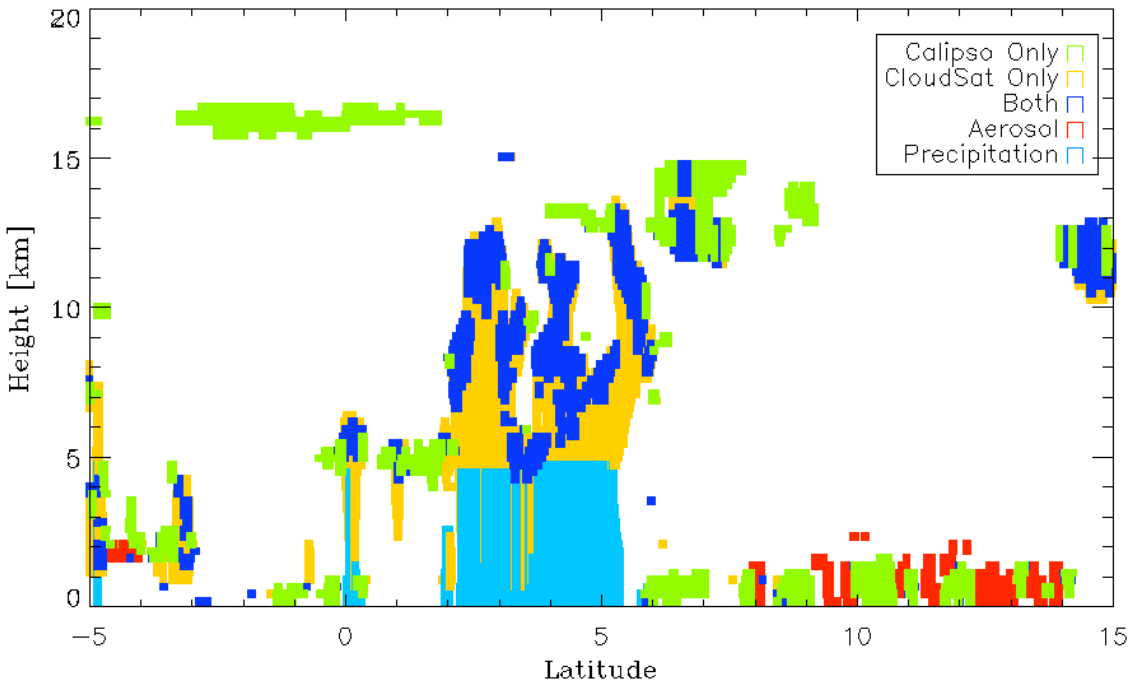

Figure 3.10. An example of the CloudSat precipitation detection. Clouds that meet the constraints now have precipitation added (a). These clouds have precipitation from the freezing level to the surface as well as cloud water added. Clouds that exceed the reflectivity needed for precipitation, but do not meet the constraints (b) show no precipitation added.

Liquid water is only added in areas of the cloud that are in temperatures above the freezing level. This is because the IWC algorithm is not affected by the 2B-CWC failure to converge to a liquid water content in the cloud. For precipitation, every CloudSat bin above freezing level to the surface is filled with a LWC of 0.11 gm^{-3} and cloud water content of 0.025 gm^{-3}. These numbers were based off of liquid water paths for precipitating clouds and cloud water of 500 gm^{-2} and 125 gm^{-2}, respectively. The thresholds to find these values lies in the highest CWC from 2B-CWC before failure. Cloud drops sizes of 13 um are used and raindrop sizes are derived from the Marshall-Palmer drop size distribution. All raindrops are assumed to be spherical and starting with the distribution,

$$N(D) = N_0 e^{-\lambda D} \quad , \tag{3.5}$$

where N(D) is the number of drops for a certain drop radius, N_0 is the initial drop amount, and D is the drop diameter described as in a gamma distribution is,

$$N_0 = \frac{3}{4}\frac{\lambda^{4+\alpha} LWC}{\pi\rho\Gamma(4+\alpha)} \quad , \tag{3.6}$$

where ρ is the density of water. This relationship can be used in a Marshall-Palmer distribution as long as α goes to zero. The last variable in the exponential is the slope of the distribution and can be defined by rearranging 3.6 to get,

$$\lambda = \left(\frac{4}{3}\frac{\pi\rho N_0}{LWC}\right)^{1/4}. \tag{3.7}$$

From this we can solve for the effective radius of the drop by the relationship of,

$$r_e = \frac{3}{\lambda}. \tag{3.8}$$

3.4 The Radiative Transfer Model

The radiative transfer model used in this research is the same used in the 2B-FLXHR algorithm from CloudSat (L'Ecuyer, 2007). The radiative transfer model was modified to include the missing clouds, aerosols, and precipitation properties and locations. After inserting the new modifications, the model was applied to the data for the 14-month period from January 2007 to February 2008. Temperature and relative humidity profiles used in the model come from matched data from the CloudSat DPC (ECMWF-AUX) and surface properties are from the International Geosphere-Biosphere Programme (IGBP).

The radiative transfer model is a two-stream, broadband, parallel plane, double adding model (Stephens et al, 2002). The inputs and some specifics of the model are described from 2B-FLXHR in Section 2.2.4. The steps for running the radiative transfer model are identical of those described in L'Ecuyer (2007). The atmospheric and surface variables are inputted into the radiative transfer model. The 18 spectral bands used in the radiative calculations are looped through individually and compute the optical properties for each layer. The cloud optical properties along with the atmospheric optical properties are then computed over spectral intervals, and inputted into the two-stream radiation transfer calculations. Each band is summed for the LW and SW fluxes, and then outputted as a flux for the layer. The amount of absorption or emission for the layer is calculated along with the flux and outputted as a heating rate. The steps taken to complete the algorithm can be found in Figure 3.11.

The output of the model are calculations of upward and downward solar and infrared fluxes at the boundaries of each of the vertical 240 m CloudSat bins. The heating rates for each bin is also determined. This will allow for calculations of fluxes at the top of the atmosphere, surface of the earth, heating profiles through many different cases, and global maps of net fluxes. Finally, by combining the information from the new fluxes and heating rates along with the merged cloud and aerosol masks from CloudSat and CALIPSO new information on the effects of clouds and aerosols on the ERB along with a more accurate view if the annual ERB can be calculated.

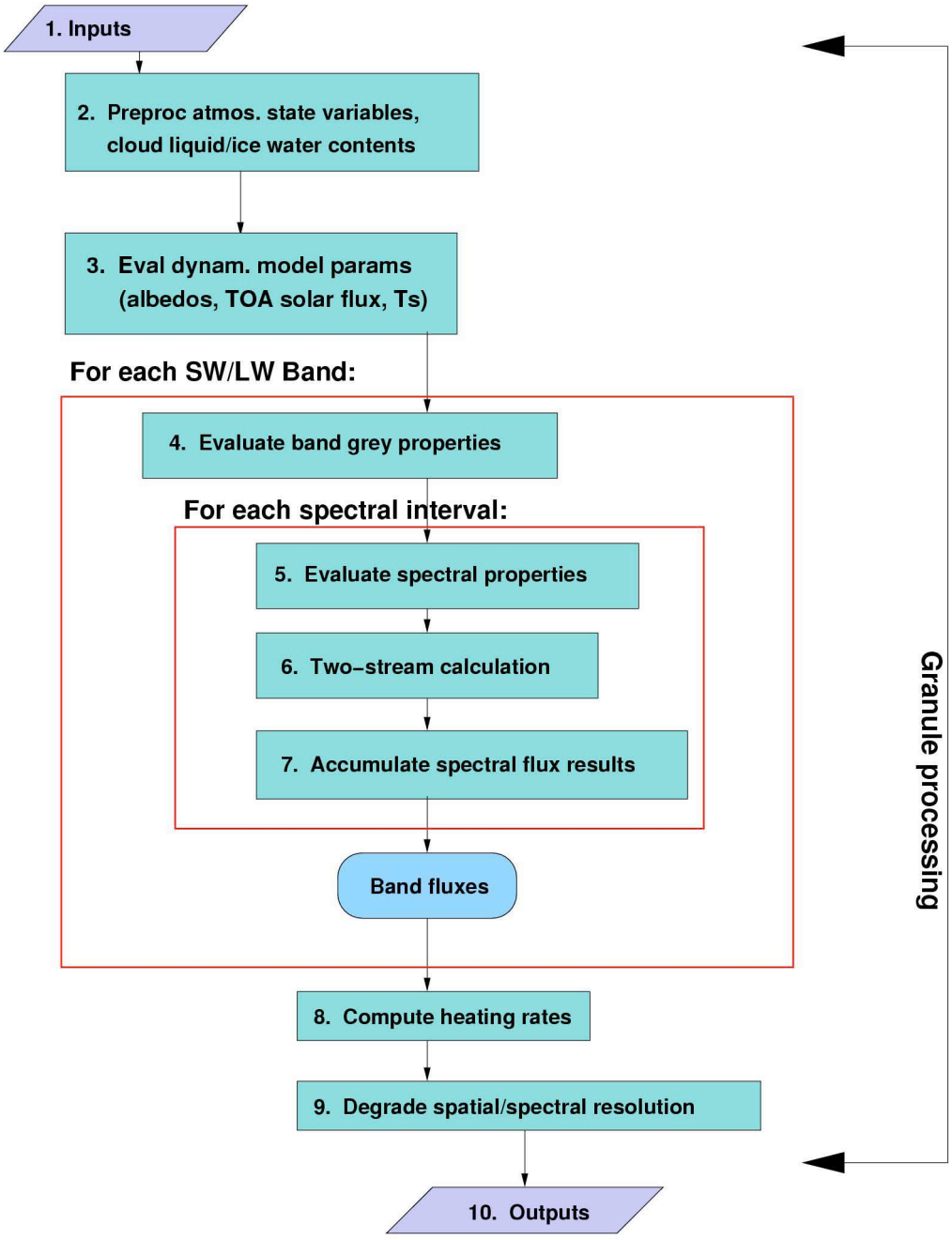

Figure 3.11. The flow of the 2B-FLXHR algorithm as well as our new merged algorithm (L'Ecuyer, 2007).

4. RESULTS

This section presents the results of the new cloud and aerosol detection methods adopted, comparison of flux products, an assessment of clouds and aerosols on the ERB, the global annual ERB, and product verification.

4.1 Distributions of Cloud and Aerosol

With the introduction of the new clouds and aerosols it is important to look at the distributions of the new clouds and aerosols to determine where the greatest impacts are likely to be found. To do this, cloud amounts were averaged into 2.5° x 2.5° grid boxes globally, and can be thought of as the cloud/aerosol fraction (frequency of occurrence) of cloud detected in each grid box. The total frequency of occurrence of all clouds can be found in Figure 4.1. The clouds detected by CloudSat are subtracted from FHR-A to find the difference in the amount of cloud reported by each cloud mask (Figure 4.2).

Clouds located along the Intertropical Convergence Zone (ITCZ) indicate a notable difference due to the undetected thin cirrus clouds are up to 65% of the time (also Haladay and Stephens, 2009). To further separate the clouds they are split into high sub-visible cirrus and low clouds missed by either ground clutter or by occurring below the minimal detectable signal of the CPR (Figures 4.3 & 4.4).

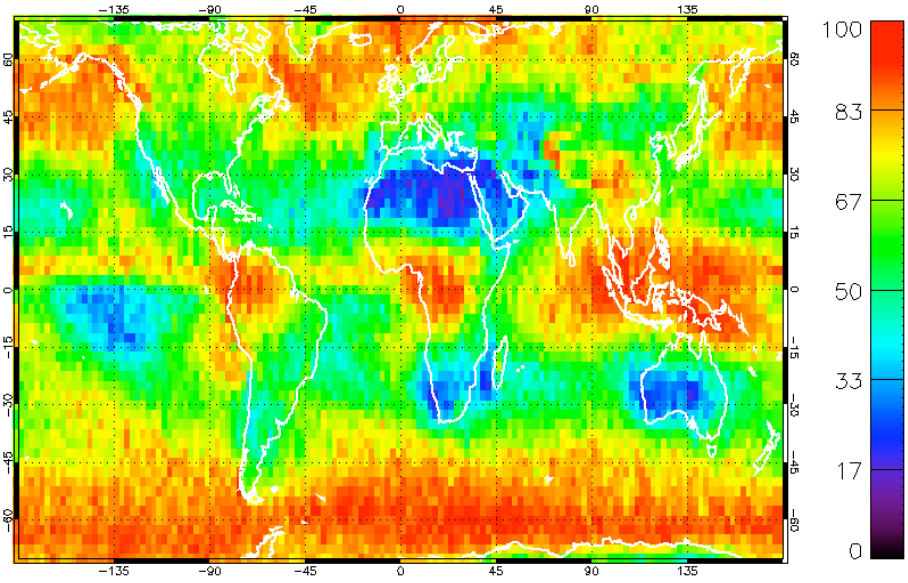

Figure 4.1. The total cloud amount from the cloud mask creating by merging CloudSat with CALIPSO. Colors are represented of the percent (%) of cloud that were located in each 2.5x2.5 degree grid box.

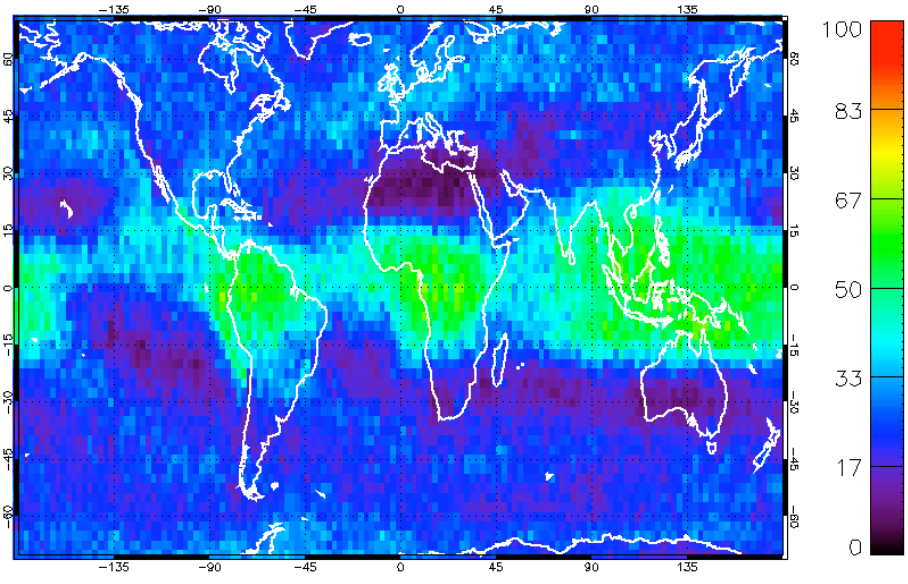

Figure 4.2. The difference in cloud amount from the 2B-Geoprof product and the cloud mask creating by merging CloudSat with CALIPSO. Colors are represented of the percent (%) of cloud that were located in each 2.5x2.5 degree grid box.

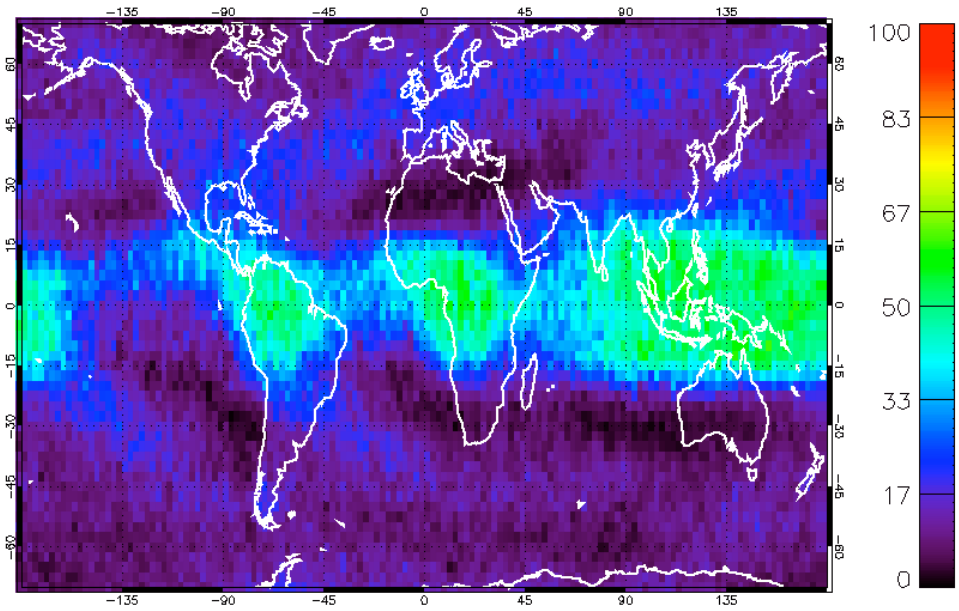

Figure 4.3. Same as Figure 4.1, but now for sub-visible thin cirrus that are not detected by CloudSat.

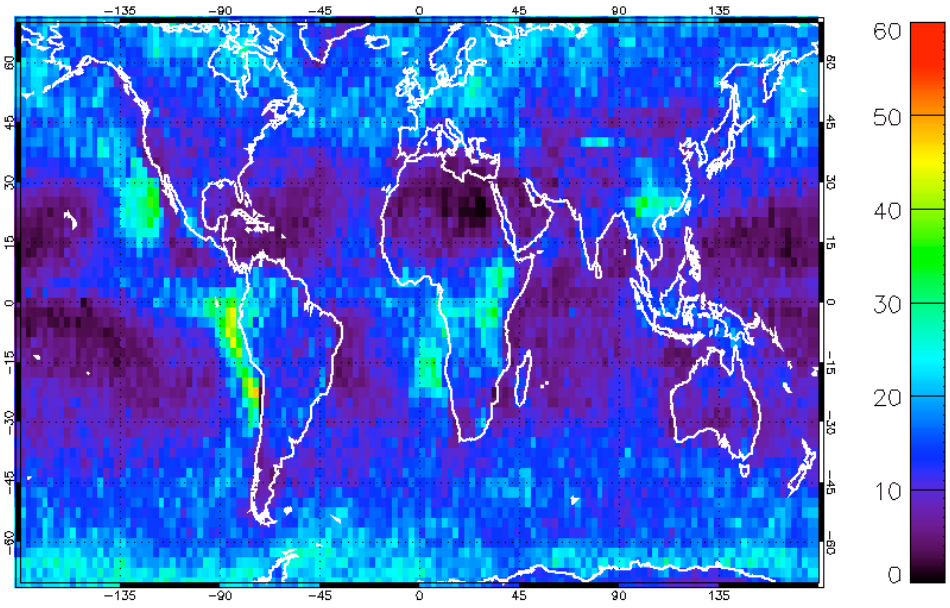

Figure 4.4. Same as Figure 4.1, but now for low clouds.

Thin sub-visible cirrus account for the clouds that are missed along the ITCZ, and over the Indian Ocean. The majority of high cloud properties in this study were calculated by using a lidar-transmission method to gain the optical depth of the

cirrus. Therefore, the mean optical depths of the cloud can also be viewed globally for undetected cirrus clouds (Figure 4.5). Looking at the distribution of optical depths for the cirrus cloud, the thickest cirrus tend to be located near the tropics, but similar values are found over the United States, Africa, and near the poles. The typical values of the thin cirrus range from 0.1 to 0.2 in optical depth. These values are also consistent with ground-based lidar measurements of thin cirrus that had observed optical depths ranging from 0.03 to 0.3 (Sassen at al., 2009).

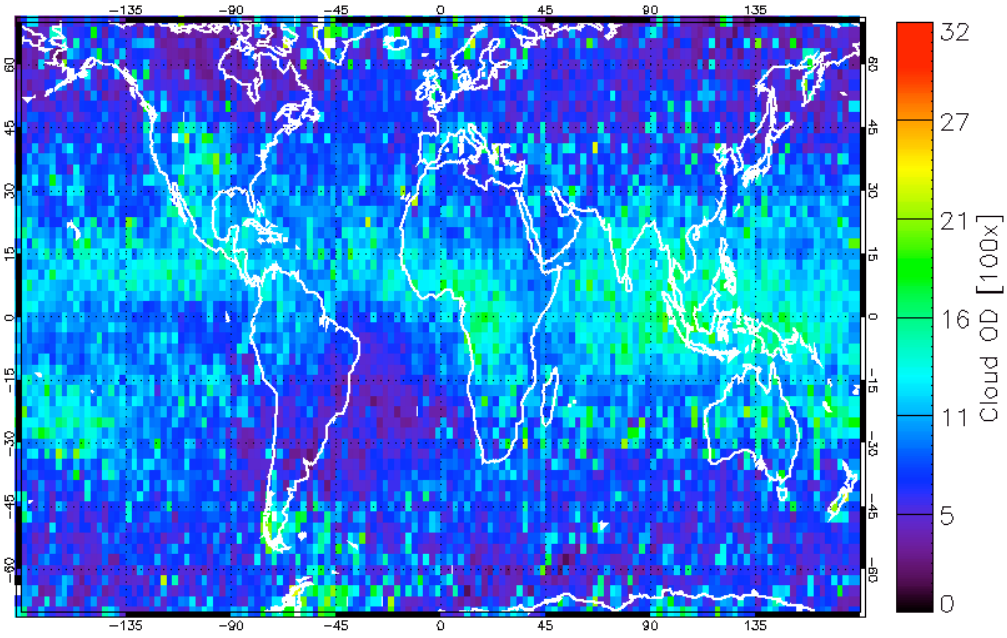

Figure 4.5. Cloud optical depth of CALIPSO only detected thin cirrus. Values of optical depth have been multiplied by 100.

Low clouds undetected by CloudSat are concentrated mostly over the three subsidence zones off the west coasts of N. America, S. America, and Africa. These areas of low cloud are the ones as indentified by Klein and Hartmann (1993) as creating local cooling of the system due to shortwave reflection by the clouds.

Studying any of these three areas in more detail would show the effects of newly detected clouds

The same process used for displaying cloud distributions is used for showing the distributions of aerosol. The aerosol are averaged globally in to 2.5° x 2.5° grid boxes and the total distribution of aerosols can be seen in Figure 4.6. The largest fraction of aerosol can be seen being transported across the Atlantic in between Africa and the Americas due to the global easterly winds that occur near the equator. Similar patterns can be found in the southern hemisphere with large amounts of aerosol in the area of global westerly winds. Another factor for the locations of the aerosol would be the total cloud cover. Comparing the distribution of aerosols to the total clouds found in Figure 4.1, where there are higher areas of cloud, there are lower occurrences of aerosol due to the inability to obtain aerosol properties when clouds obstruct the aerosol layers. It is also easy to see the distribution by observing the mean aerosol optical depth (AOD) (Figure 4.7).

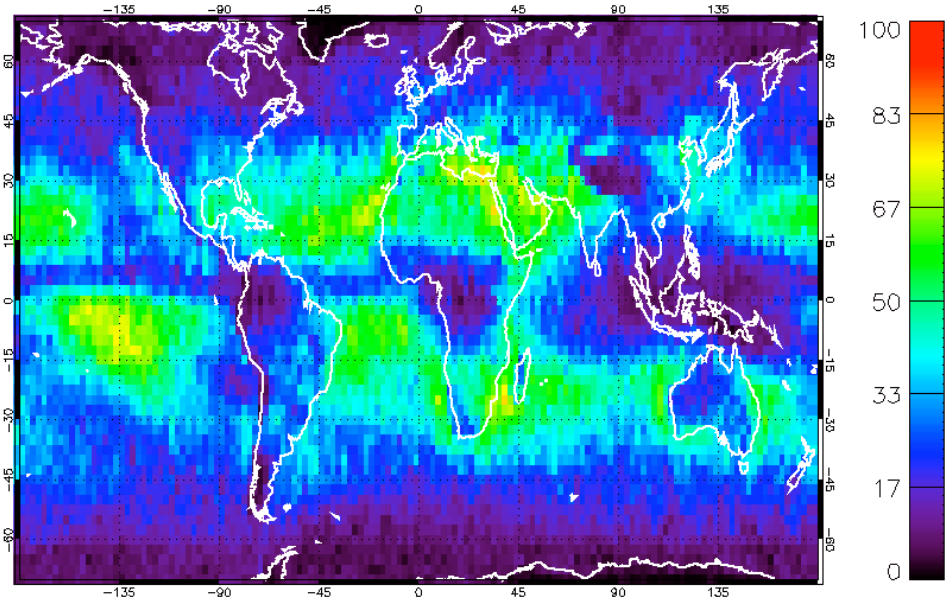

Figure 4.6. Total fraction of aerosol detected globally. Colors are represented of the percent (%) of aerosol that were detected in each 2.5° x 2.5° degree grid box.

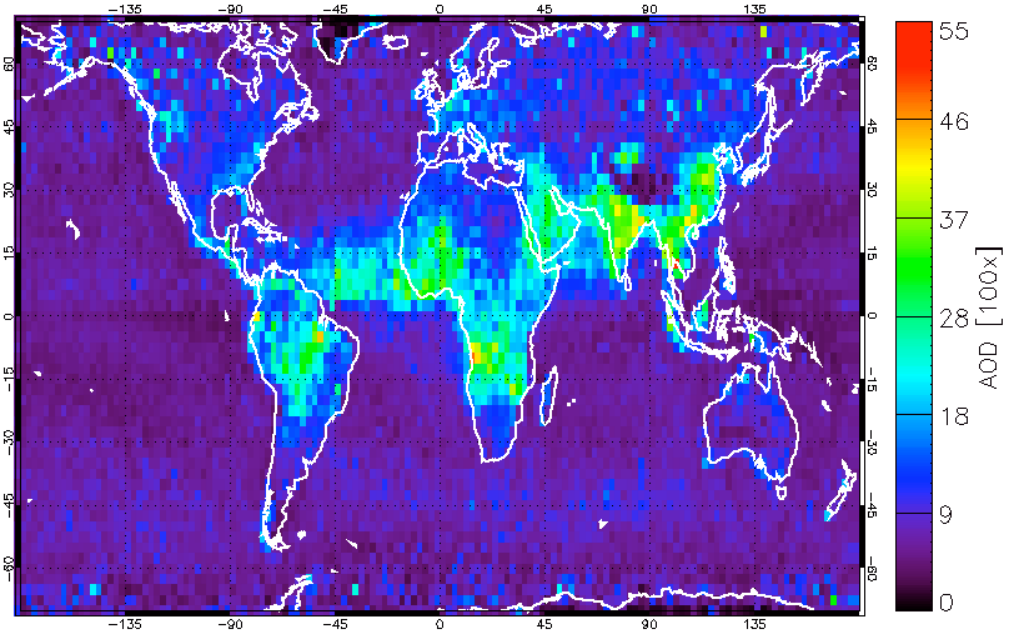

Figure 4.7. Aerosol optical depth of CALIPSO only detected aerosols. Values of optical depth have been multiplied by 100.

Here areas of aerosol with the largest optical depth are seen by the transport of Saharan dust over Africa to the Atlantic Ocean, the burning of forests in South

America and Southern Africa, pollution and biomass burning over Asia, as well as the polluted coastal areas in China. Looking at the mean optical depth eliminates the frequent marine aerosols from view, as their optical depth is not as large as that of dust, smoke, and pollution.

Using CALIOP's detection algorithm aerosols can be sorted into individual types, and their distributions are shown in Figure 4.8. The higher distributions of marine aerosols occur in areas over the ocean, again where cloud cover is at a minimum. Dust and polluted dust are more highly concentrated over African continent, with evidence of dust transport over the oceans. Smoke does not show any sort of visible pattern in this distribution, but the location of smoke near the Amazon as well as in southern Africa could be evidence of burnings in the tropical rain forests.

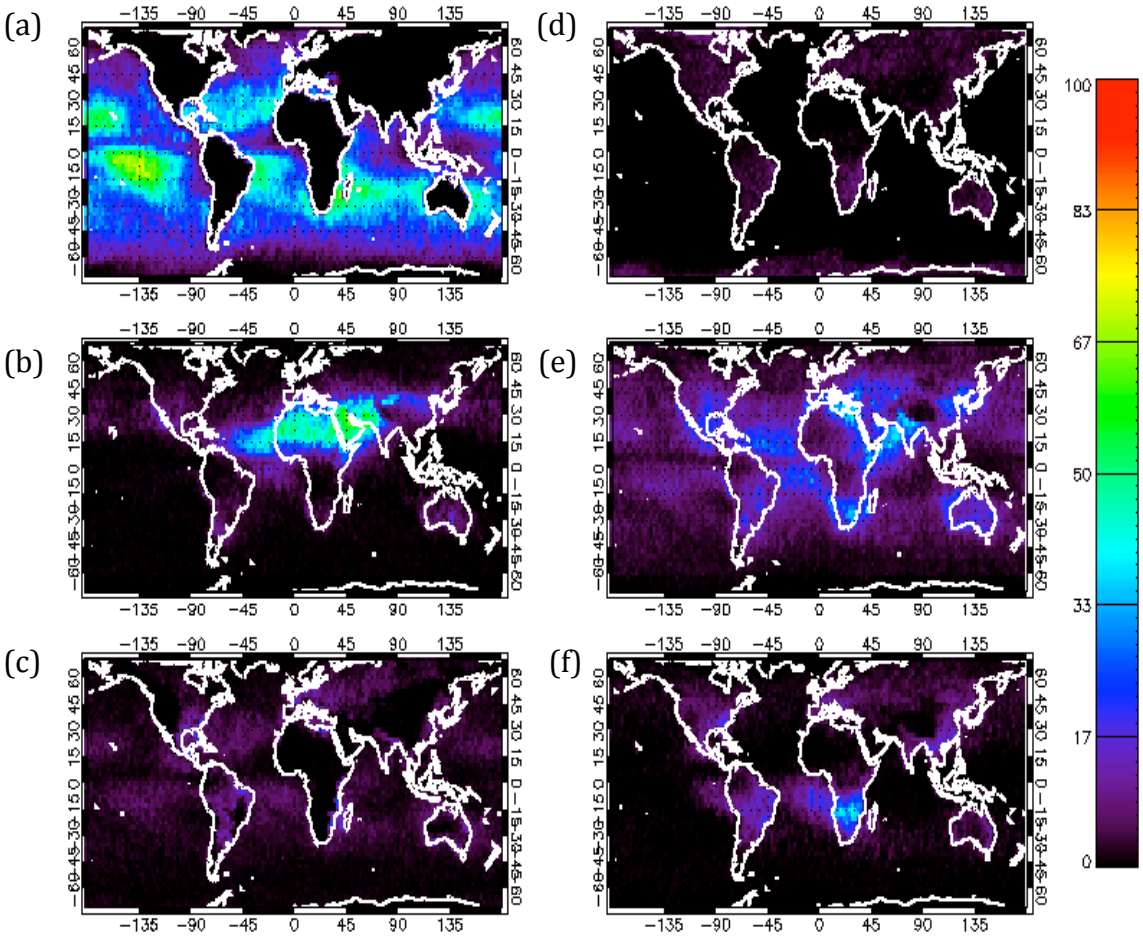

Figure 4.8. Same as Figure 4.6, but aerosols are broken up into marine (a), dust (b), polluted continental (c), clean continental (d), polluted dust (e), and smoke (f). Colors are represented of the percent (%) of aerosol that were located in each 2.5 x 2.5 degree grid box.

4.2 Impacts of New features on the Radiation Budget

4.2.1 Heating Rates

The fluxes and heating rates created for the FHR-A database will vary from the fluxes and heating rates found in the 2B-FLXHR product. To examine how they

differ, individual granules of heating rates are presented with an example shown in Figure 4.9.

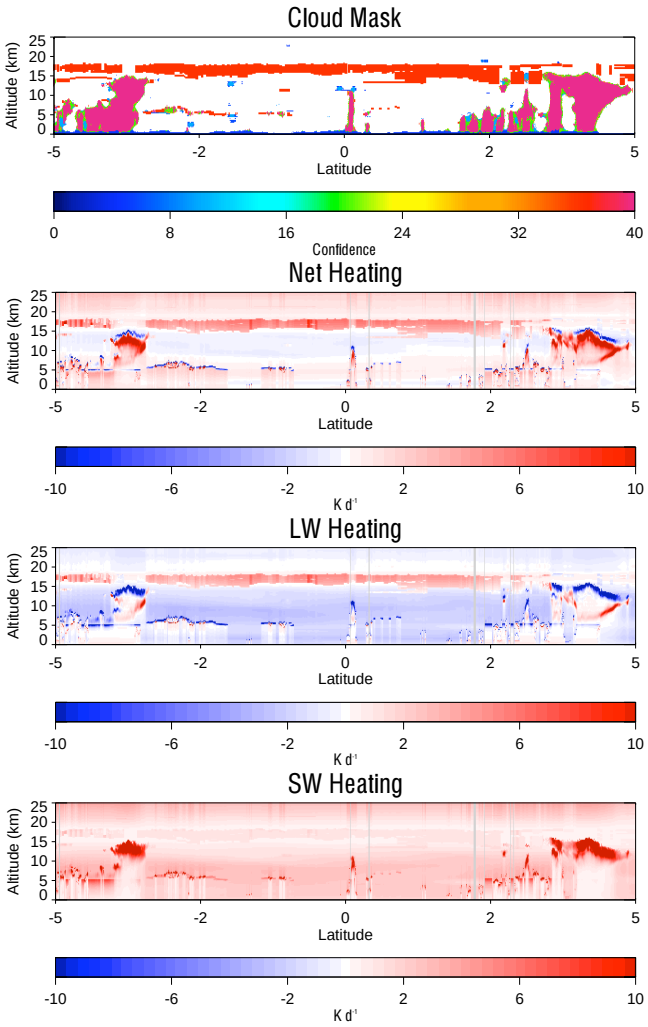

Figure 4.9. The heating rates created using the CloudSat and CALIPSO data. The features shown are the CloudSat and CALIPSO cloud mask, net heating, LW heating, and SW heating (units in K day^{-1}).

The clouds, shown in the cloud mask, only seen by CALIPSO can be seen in a brighter red, while the higher confidence clouds from CloudSat are seen in a pink

shade. This is an example of an individual cirrus missed by the CloudSat CPR. The cirrus extends along the tropics in between two convective cloud structures. In order to find the impacts of the new cirrus the difference between FHR-A and the 2B-FLXHR product is taken. This process will also be used for added low clouds, aerosols, and change in precipitation properties. Two examples, one for the thin cirrus and one emphasizing low cloud effects are shown in Figure 4.10. The undetected cirrus (Figure 4.10a) is as described earlier and labeled with (1) in the figure and the undetected low clouds are labeled with (2) in 4.10b. The low clouds are a case off of the western coast of S. America where there were a higher number of missed low clouds. The cirrus cloud of Figure 4.10a causes a net warming below the cloud as longwave radiation is absorbed by the cirrus and reemitted back to the surface. This allows less LW radiation to escape to space and creates a warming below the cirrus. The cirrus has little impact on solar radiation reaching the surface, but does reflect a small amount as observed by the solar heating above the cirrus cloud. The low clouds in Figure 4.10b are clearly visible in the heating rate differences. There is a large amount of LW cooling at the top of the low clouds, associated with the emission from cloud top to space. Solar heating can be seen at cloud top from absorption also occurs, and also above the clouds due to their high albedo effect.

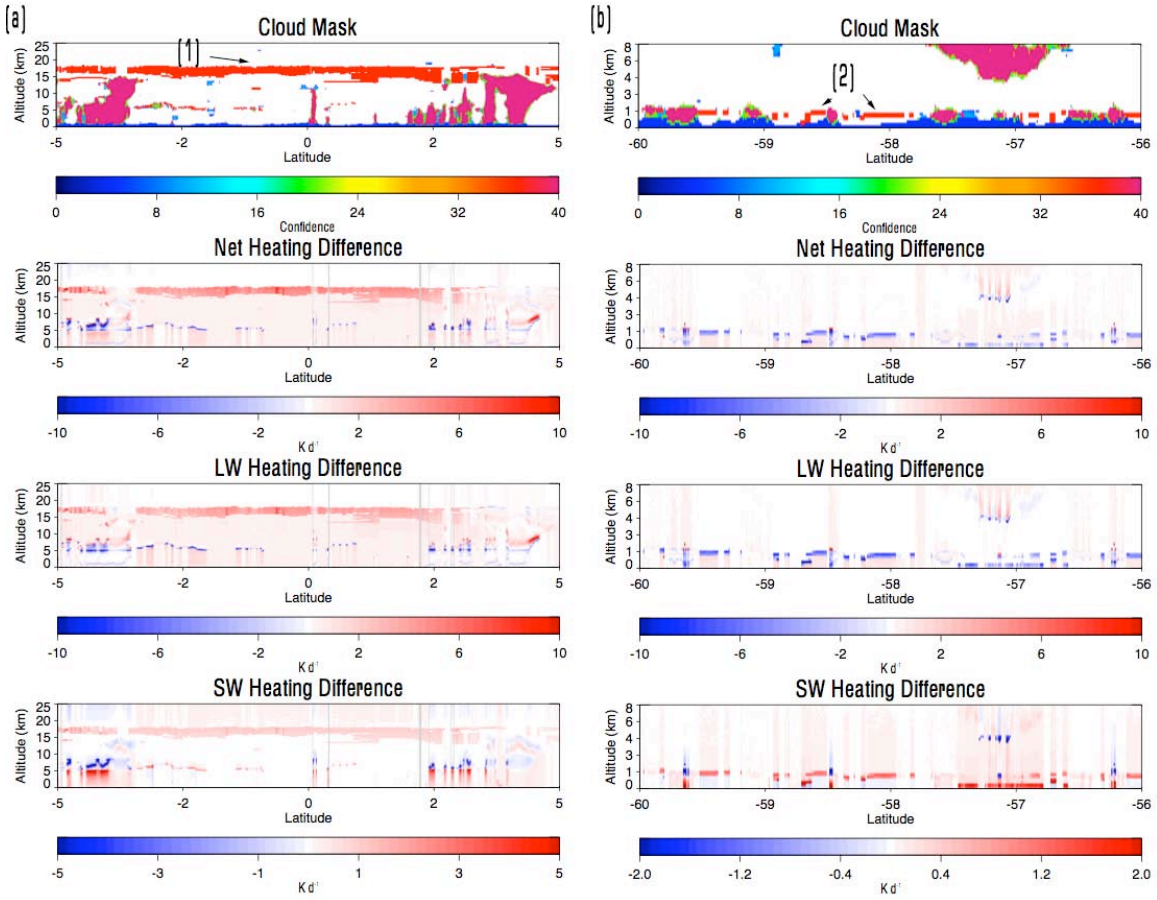

Figure 4.10. The cases used for high sub-visible thin cirrus (a) and low undetected stratus (b). The locations of the undetected clouds are labeled in the cloud mask for each figure. The figures also contain the net heating, LW heating, and SW heating differences between the heating rates in this study and the 2B-FLXHR product (units in K day^{-1}). Any gray shading in the figure denotes data that was not calculated due to missing properties.

Next, the differences in the products due to changing precipitation properties and adding aerosol are examined. A case in the tropics near the ITCZ was chosen for precipitation and the aerosol example is off of the coast of Africa where CALIPSO detected a layer of Saharan dust (Figure 4.11). The precipitating cloud (Figure 4.11a), as detected by CloudSat, is labeled with (3) and the Saharan layer (Figure 4.11b) is labeled with (4). In the precipitation case the most notable feature is the large layer of heating in the LW and cooling in the SW near 8 km. This corresponds to the heating peak created by the 2B-FLXHR product that was discussed earlier in the paper, and will be discussed later in the paper. There is a cooling at what was the cloud base near 1 km, due to extending rain and cloud water contents to the surface. The freezing level can be seen in the LW cooling near 5 km as the water transitions to ice, and heating below is due to the increased amount of SW radiation resulting from the decrease in precipitation amount in the clouds.

The aerosols are shown in the cloud mask as a bright orange color. It is to be noted that the orange color is to denote the presence of aerosol and not the confidence of the detection. The Saharan dust has an overall heating effect on the atmosphere. The majority of this is due to the absorption of solar radiation, and only slightly by trapping LW radiation from the Earth's surface. It can also be seen that there is a cooling under the dust layer where dust is aloft from the surface. The heating in the aerosol layer also causes the heating of the atmosphere above it, including weak heating into the stratosphere.

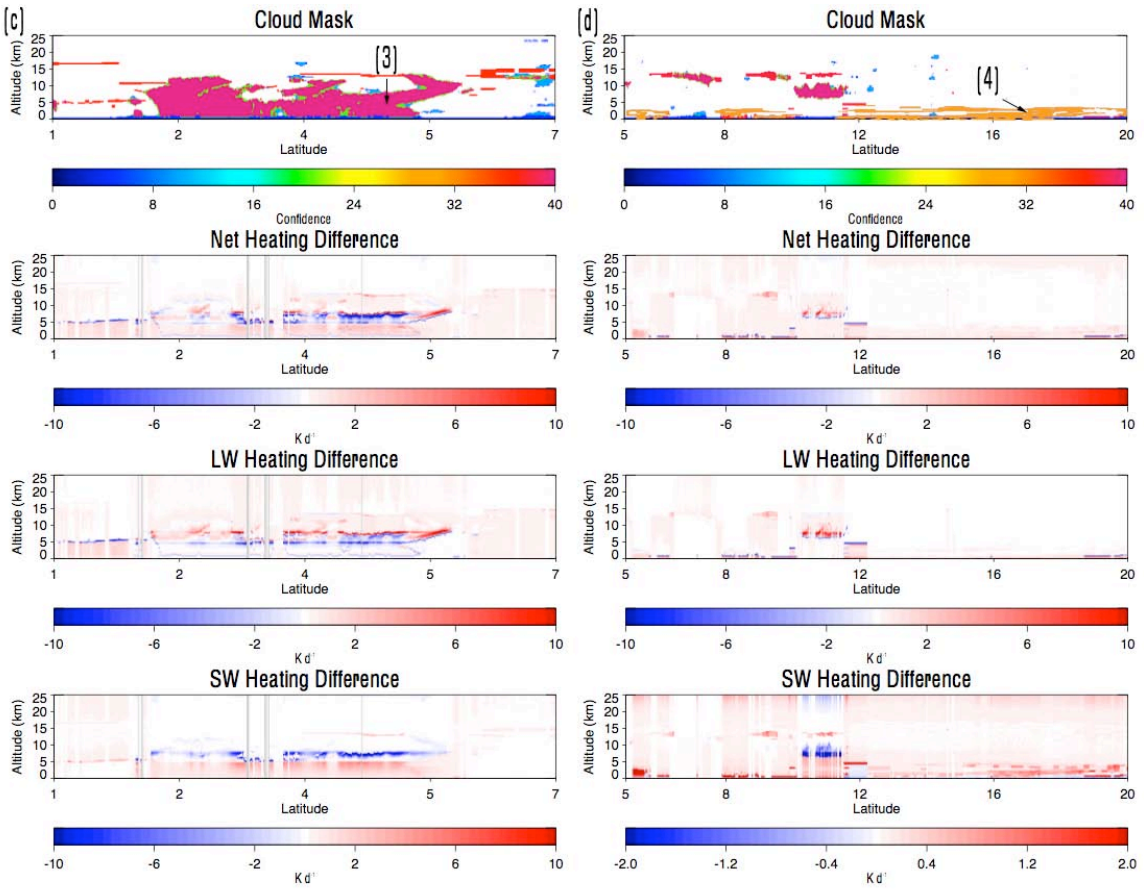

Figure 4.11. The cases used for precipitation (c) and a Saharan dust layer (d). The locations of the undetected clouds/aerosol are labeled in the cloud mask for each figure. The figures also contain the net heating, LW heating, and SW heating differences between the heating rates in this study and the 2B-FLXHR product (units in K day^{-1}). Any gray shading in the figure denotes data that was not calculated due to missing properties.

The differences in heating rates between FHR-A and 2B-FLXHR shows evidence that the introduction of new clouds and aerosols have a large effect on the atmospheric heating rates. This is further realized in vertical profiles shown in Figure 4.12. Profiles located by the labels 1-4 in Figures 4.10 and 4.11 are presented in Figure 4.12; Highlighting the LW and SW heating rate profiles for the cases of cirrus, low cloud, precipitation, and aerosol. For the cirrus case there is an obvious change in heating around 15 to 18 km, especially in the LW. The heating is by the absorption of LW and SW radiation in the cloud layer, as well as heating below the cirrus cloud and a cooling above the cloud where less radiation is emitted to space. The heating from the cirrus definitely shows how the cloud can act as a blanket by warming the atmosphere below. For the low cloud case, weak heating occurs below the cloud due to LW radiation and a cooling in the SW below the cloud. For precipitation, a large peak occurs near 8 km, as described earlier, from the 2B-FLXHR is noticeable in both the SW heating and LW cooling. This peak is due to an over abundance of liquid water in the mixed phase regions of the cloud and is removed in the new product.

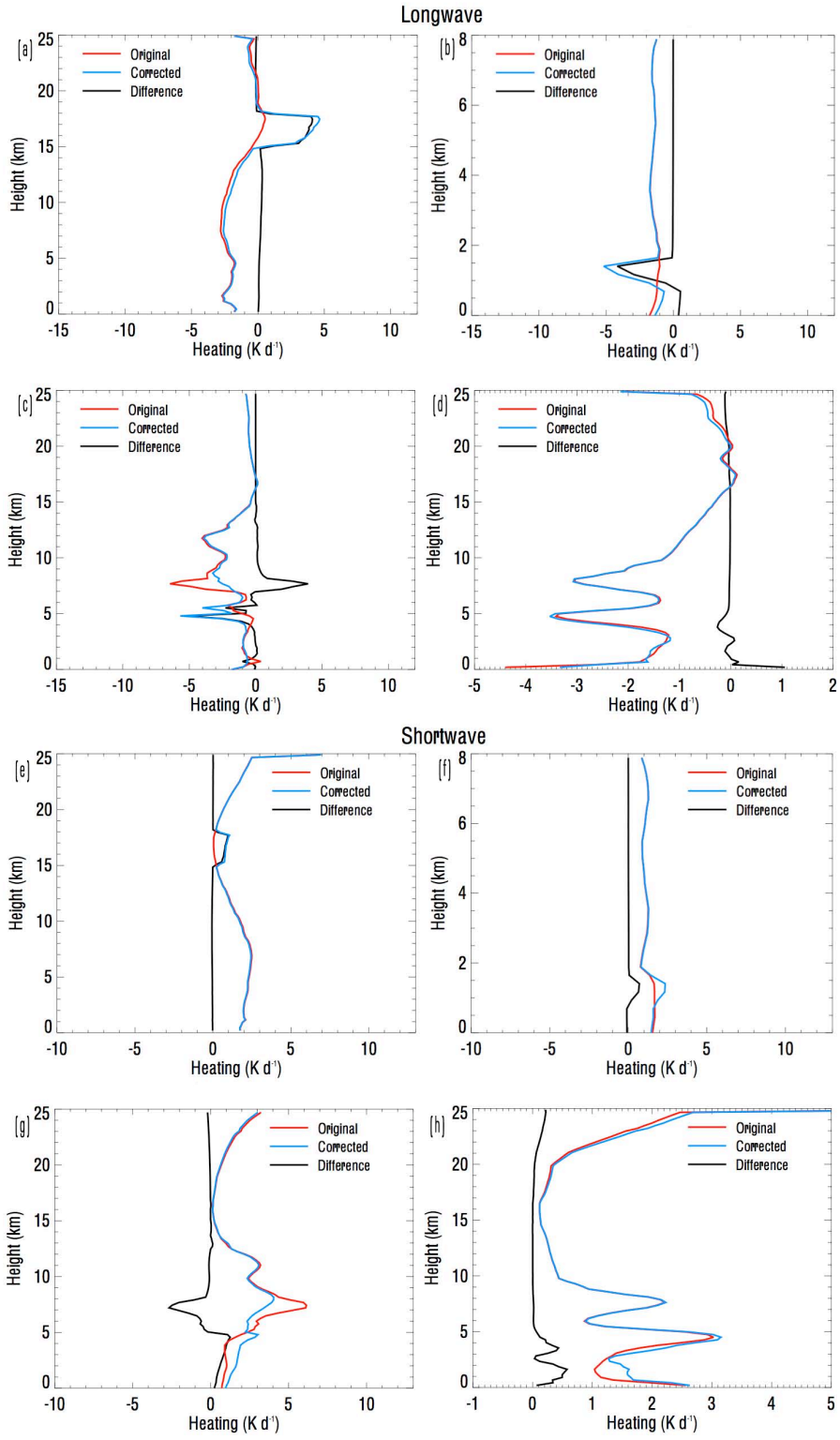

Figure 4.12. The vertical longwave/shortwave heating profiles for the cirrus (a/e), low cloud (b/f), precipitation (c/g), and aerosol (d/h) cases are shown (units in K day^{-1}). For each case the 2B-FLXHR (red), fluxes for FHR-A (blue), and the difference between are shown (black).

In FHR-A LW heating maxima occur at the freezing level ~5 km and near cloud top ~13 km. Finally, the heating changes in the aerosol layer are more readily evident in the SW vertical profile. The greatest heating is within the aerosol layer itself, but there are also influences on the SW heating in the SW above the aerosol layer. Heating can also be found in the LW radiation within the aerosol layer, but the larger impact would be the reduction of LW radiation from the Earth's surface to space, seen in the cooling of the layers above. The net effect of all cases for LW and SW heating are shown in Figure 4.13.

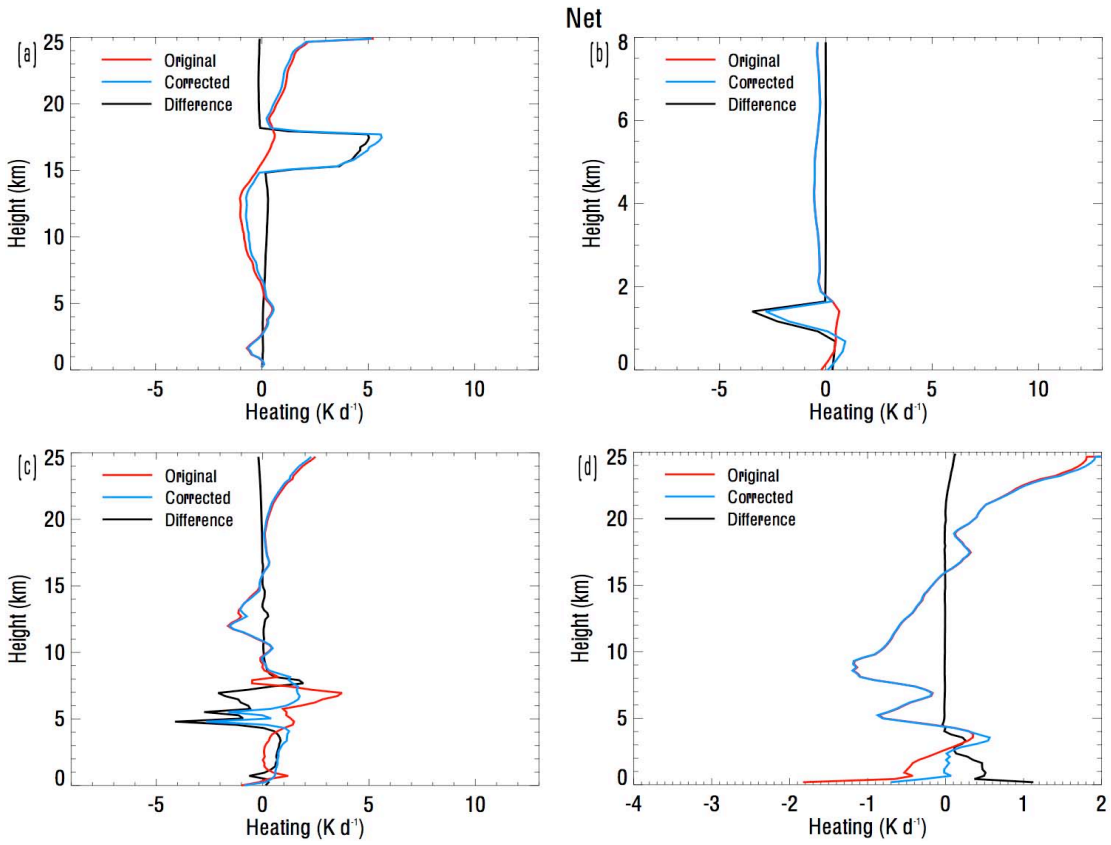

Figure 4.13. Net heating (Net = LW + SW) profiles of cirrus (a), low cloud (b), precipitation (c), and aerosol (d) cases.

4.2.2 Effects of Clouds on Radiative Fluxes

The impacts of the newly added clouds on the radiative fluxes can be illustrated by the introduction of the cloud radiative effect, also referred to as cloud forcing (eg Hartmann et al., 1986 and Ramanathan, 1987) defined as,

$$C_{NET} = F_{Clear} - F_{Cloudy} \tag{4.1}$$

where C_{NET} is the net cloud effect which is the difference in upward and downward fluxes in clear skies (Clear) and all sky (Cloudy). Looking at their radiative effect only where the new clouds are detected by CALIPSO, the impacts of these clouds can be seen. To fully understand the impacts globally and temporally, the cloud forcings are presented both for seasons and in the annual mean. The impacts, seasonally and annually, of low clouds not detected by CloudSat is highlighted in Figures 4.14-4.18. The seasons selected are December 2007-February 2008 (DJF), March-May 2007 (MAM), June-August 2007 (JJA), and September-November 2007 (SON). Seasonally the low clouds exhibit the strongest impact in JJA and SON in the three major subsidence zones near the west coasts of N. America, S. America, and southern Africa, with values reaching as high as -55 W Wm^{-2} in SW at TOA and -62 Wm^{-2} at BOA. The LW effect at the TOA is relatively negligible as the temperatures of the low clouds are near the surface temperature. The opposite holds true for LW at BOA where LW radiation is trapped below the clouds. Here we see values as high as -48 Wm^{-2} in SON and average values around 25 Wm^{-2} in regions of low stratus in MAM, JJA, and SON. A positive net flux at BOA occurs in the winter hemispheres at the poles where perpetual night exists, and the low clouds trap LW radiation without

any SW effects. The opposite is in effect for areas with perpetual daylight or longer amounts of sunlight in the summer hemispheres at high latitudes, especially in the southern hemisphere near the storm track belt at around -60° S in the DJF season.

In the annual mean, the low clouds have a cooling effect at the TOA. Areas globally that have higher surface albedo have a net radiative impact close to zero, or slight positive, such as in the Saharan Desert as well as in the Himalayas where snow or ice are present. Positive values near the poles are also observed at the BOA net annually showing low clouds tend to have a strong impact in the LW during the respective winter hemispheres. The globally averaged seasonal and annual values for the radiative impacts of low clouds are summarized in Table 4.1. There is little variation in the total LW radiation at TOA, but there is a slight seasonal variation in SW. This season shift is due to the cloud impact from the mid-latitude storm tracks in each hemisphere, with the strongest being DJF in the southern hemisphere, MAM where there is less influence from the storm tracks, and the subsidence regions. Overall, the low clouds contribute to a cooling of the atmosphere with a net of -3.6 Wm^{-2}. The same pattern follows for fluxes at BOA with higher impacts in both LW and SW, due to the low cloud heights causing more emission to the surface in the LW, and the surface receives less SW due to absorption and reflection of solar radiation. There is a larger increase in LW at BOA than SW; therefore the overall cooling at the surface is less annually at -1.46 Wm^{-2}.

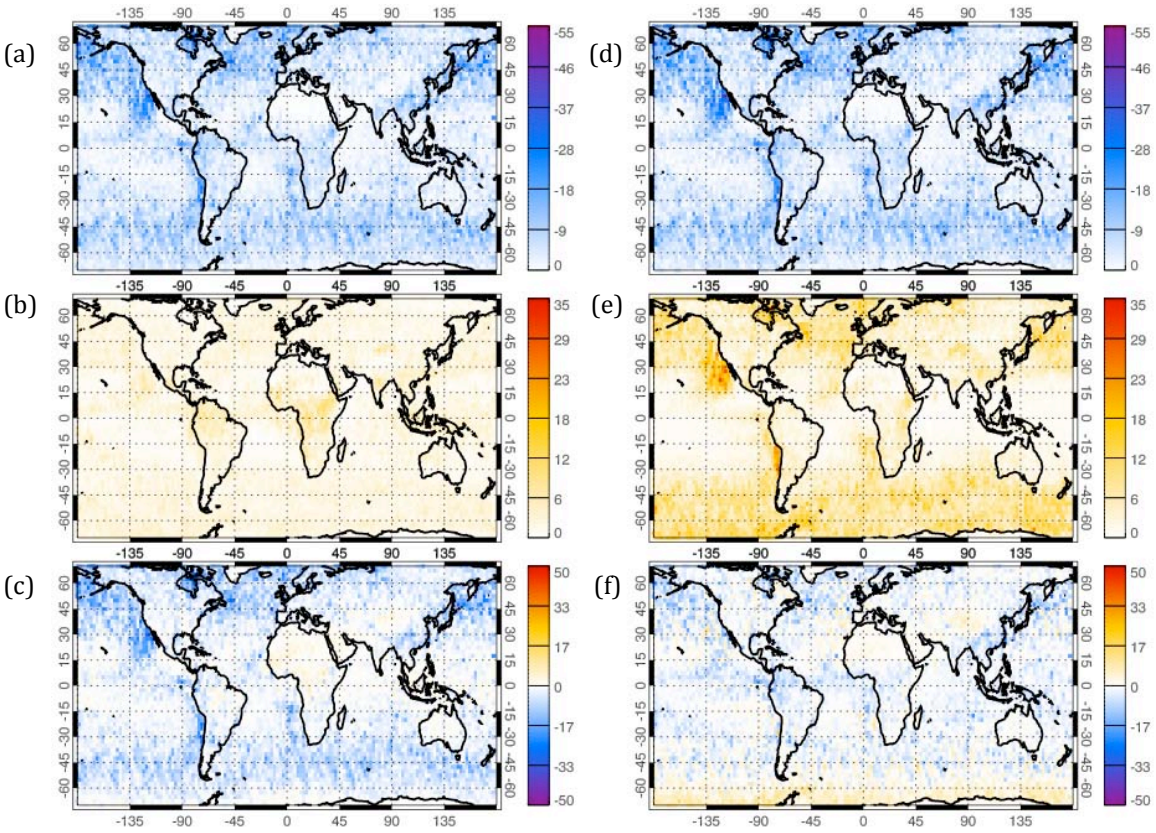

Figure 4.14. The MAM radiative forcing of low clouds undetected by CloudSat. The TOA SW (a), LW (b), and NET (c), along with BOA SW (d), LW (e), and NET (f) fluxes are shown, with units in Wm^{-2}.

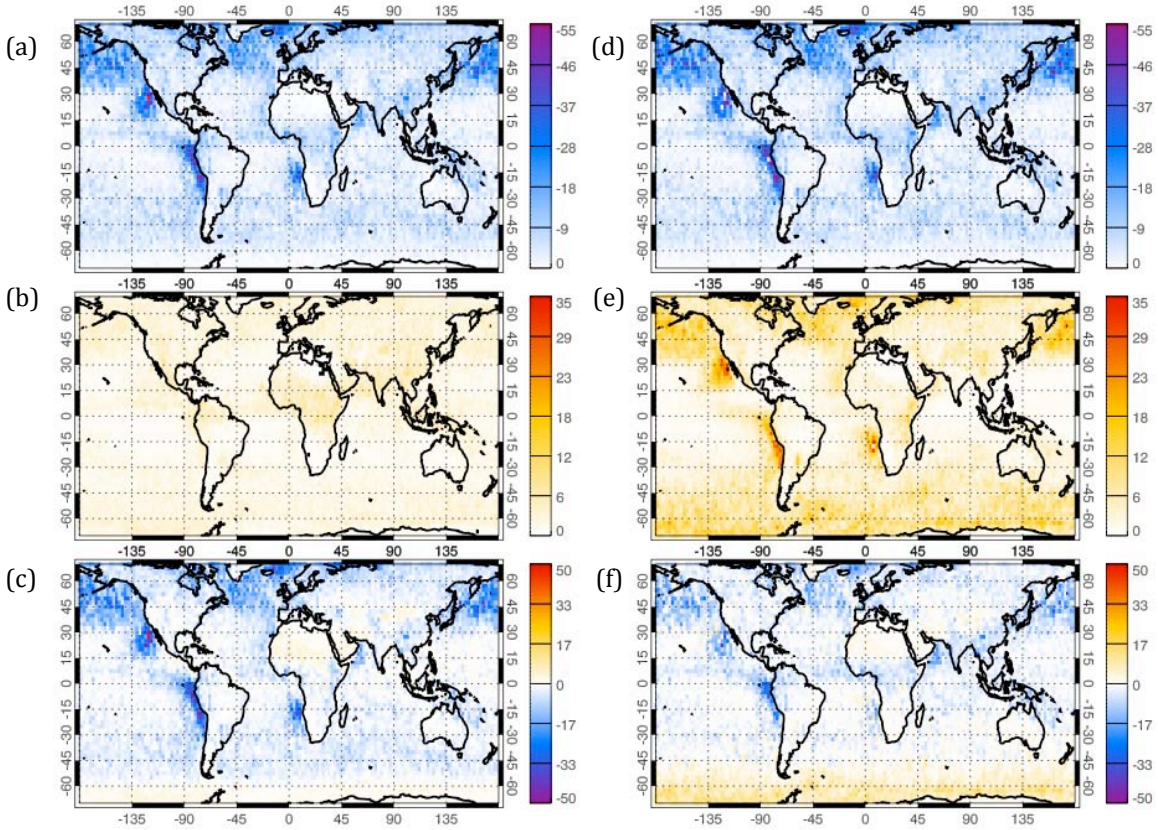

Figure 4.15. Same as Figure 4.14, but for JJA, with units in Wm^{-2}.

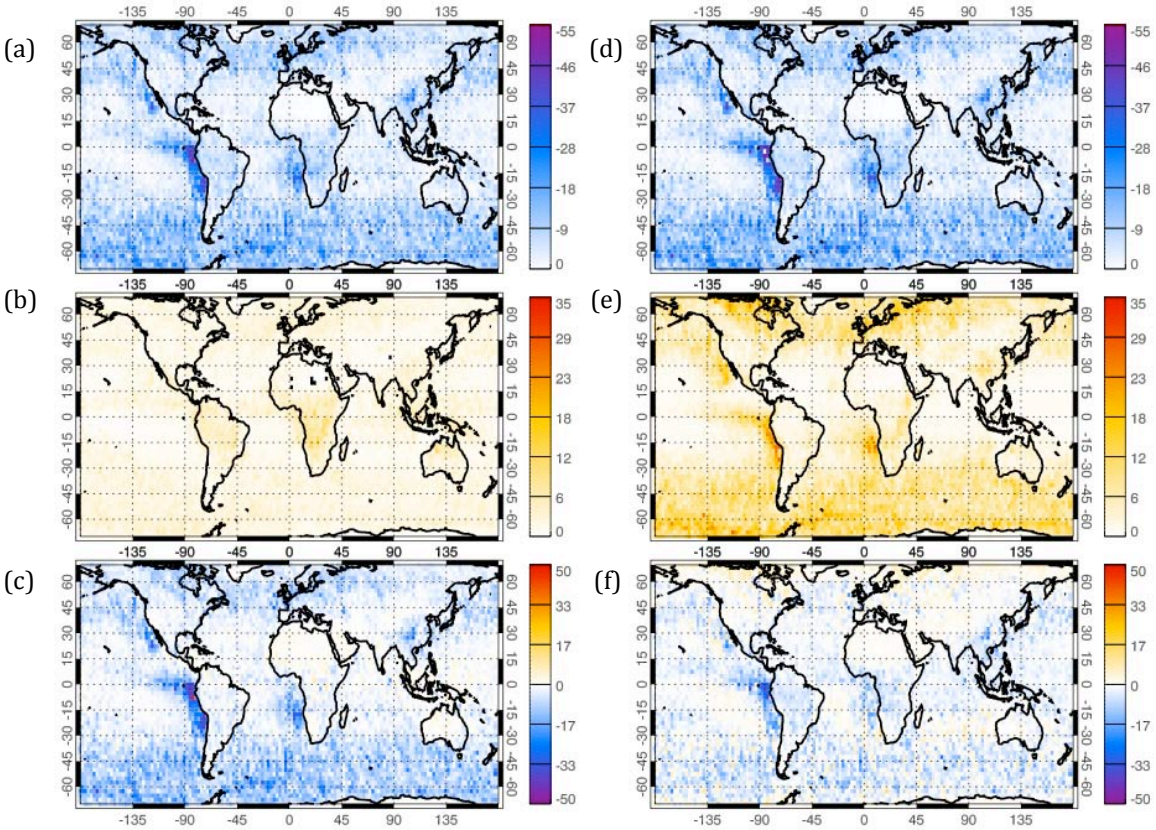

Figure 4.16. Same as Figure 4.14, but for SON, with units in Wm^{-2}.

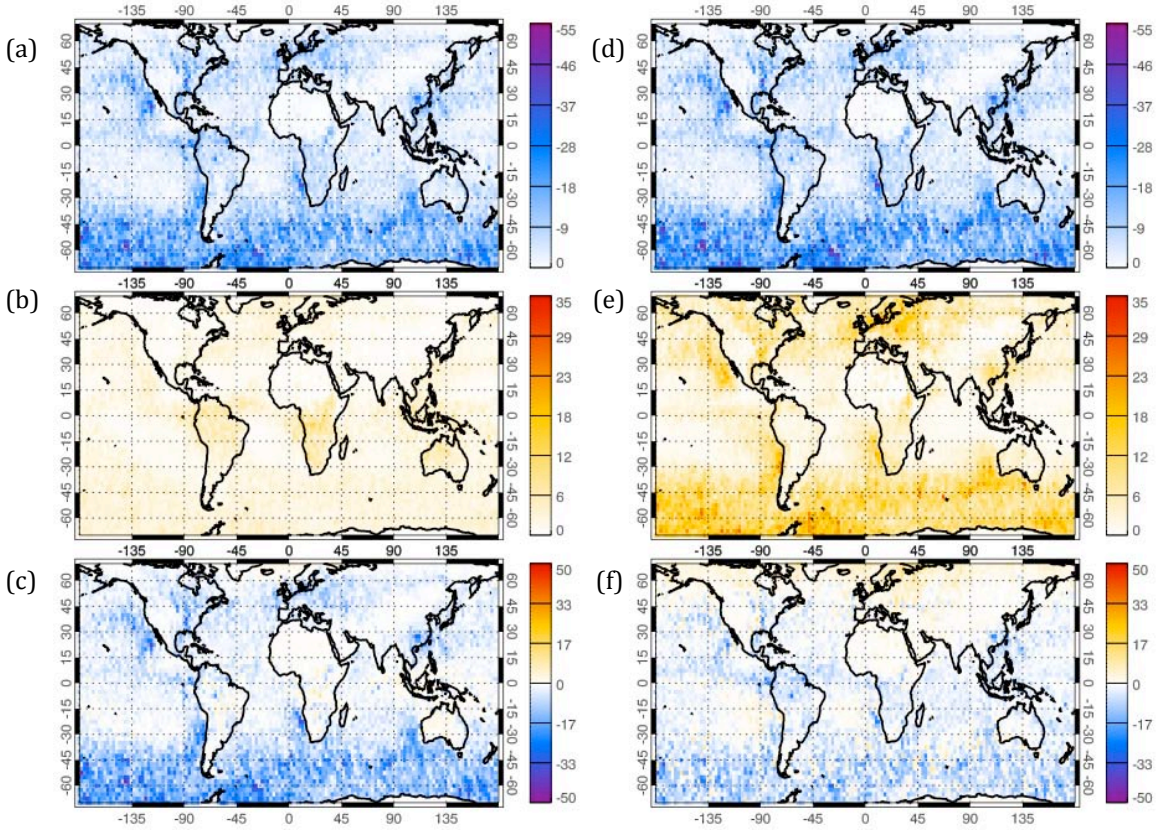

Figure 4.17. Same as Figure 4.14, but for DJF, with units in Wm^{-2}.

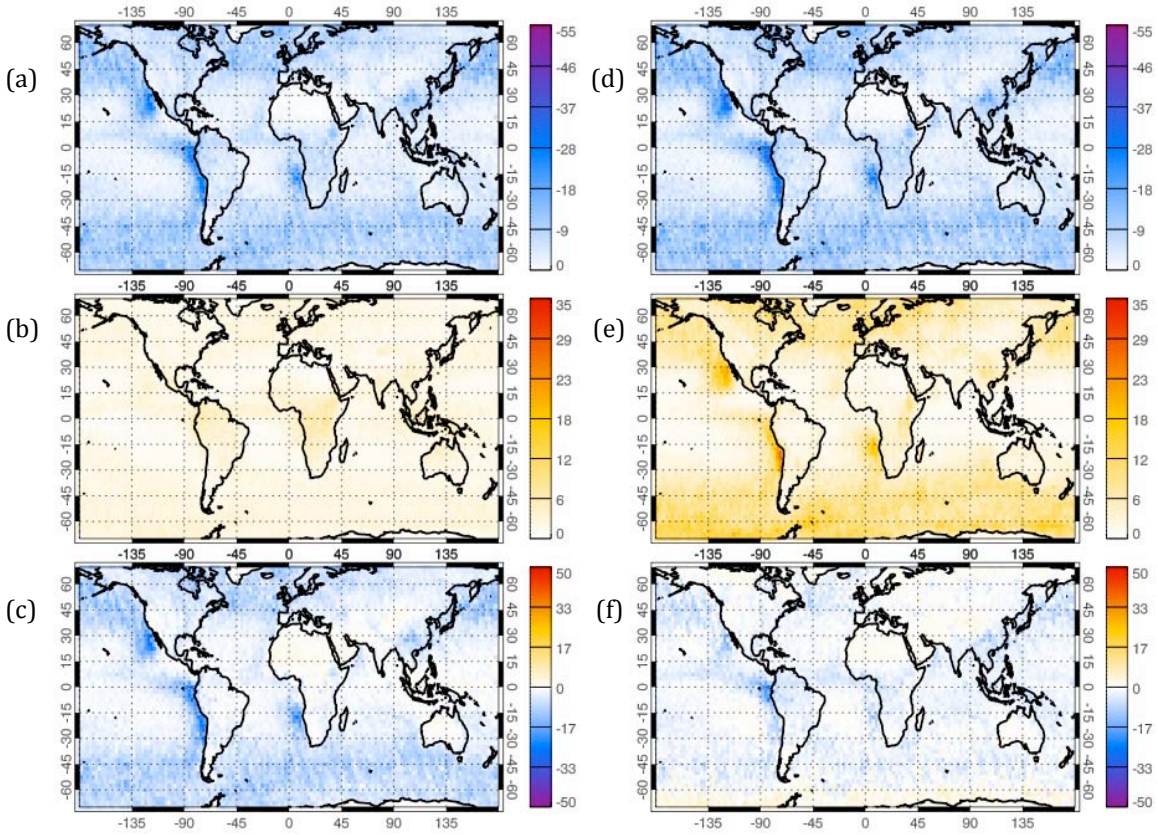

Figure 4.18. Same as Figure 4.14, but for the annual average, with units in Wm^{-2}.

	DJF	MAM	JJA	SON	ANNUAL
TOA,SW	-6.14	-5.19	-5.36	-5.98	-5.67
TOA,LW	2.07	2.08	2.06	2.07	2.07
TOA,NET	-4.07	-3.17	-3.30	-3.91	-3.60
BOA,SW	-6.69	-5.51	-5.77	-6.41	-6.10
BOA,LW	4.97	4.36	4.41	4.82	4.64
BOA,NET	-1.72	-1.15	-1.36	-1.59	-1.46

Table 4.1. The seasonal and annual globally averaged radiative forcing of low clouds undetected by CloudSat. The TOA and BOA fluxes are shown in SW, LW, and NET, with units in Wm^{-2}.

The zonally averaged annual mean values are illustrated by latitude in Figure 4.19 as a function of latitude, showing the overall effect of the low clouds zonally on the ERB. It is more evident in this figure that the highest impact of low clouds are in the higher latitudes where the mid-latitude storm tracks are located, as well as the subsidence areas of the western coasts of N. America, S. America, and Africa. There is a positive net effect in the high latitudes of the southern hemisphere where there is persistent cloud year-round, combined with the larger LW during the hemispheres winter where the decrease in daylight increases the LW effect.

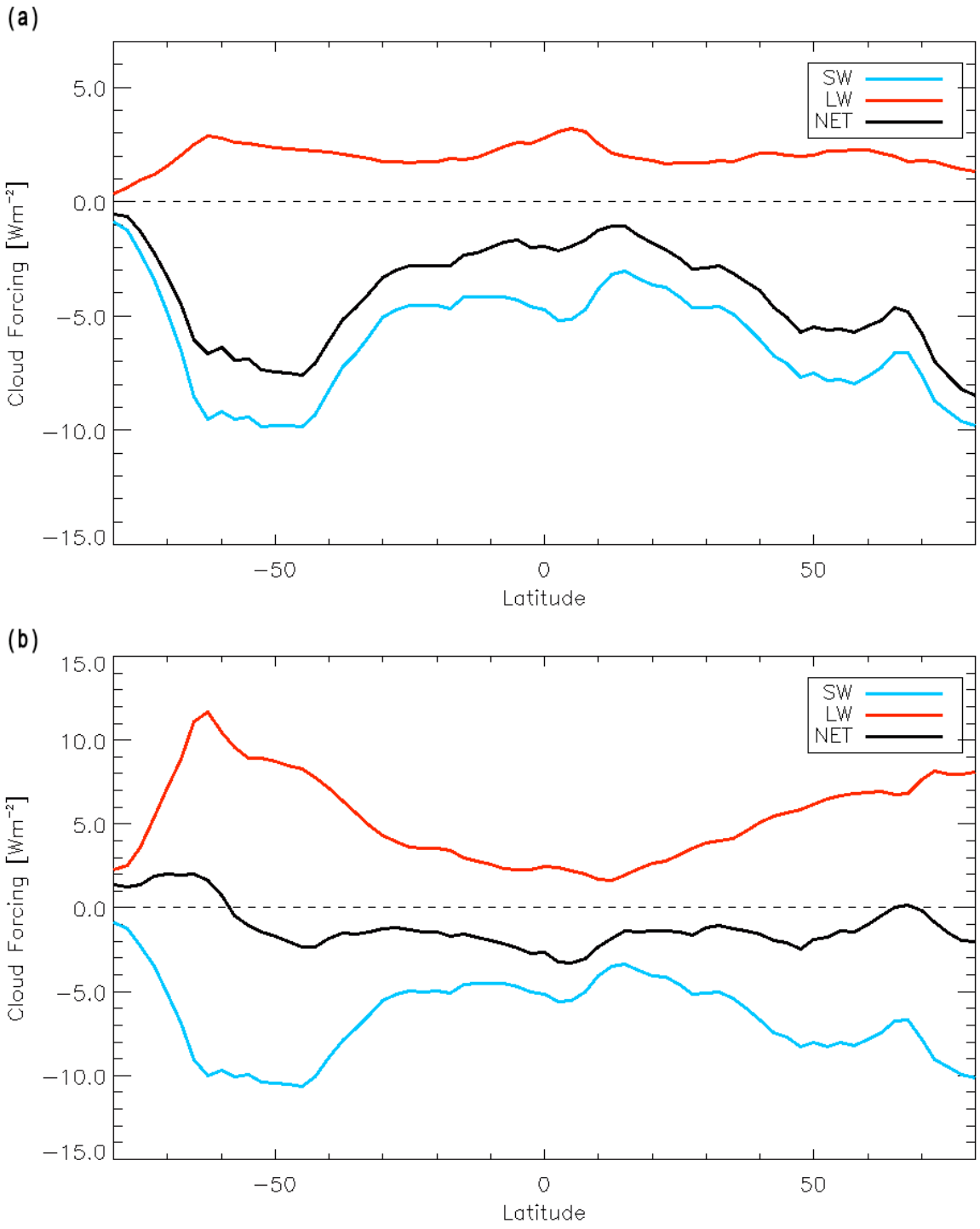

Figure 4.19. Latitudinal averaged radiative forcing of low clouds undetected by CloudSat for TOA (a) and BOA (b), with units in Wm^{-2}.

The impacts of thin sub-visible cirrus not detected by CloudSat are analyzed in a manner similar to that of low clouds (Figures 4.20-4.24). Impacts of the cirrus are most prominent in the tropics where deep convection is more frequent. Effects also exist in the mid-latitude storm tracks, most obviously in the transition seasons of MAM and SON. The cirrus clouds have a much lower radiative effect than the low clouds as they have optical depths << 1 and are constructed of sparse ice crystals. The ice crystals are not efficient at absorbing or reflecting SW radiation, but effective absorbers of LW radiation (Stephens et al., 1981). This can be seen in the TOA LW and the TOA NET where there is a positive net effect of the cirrus, causing a warming in the atmosphere. The positive radiative effect at TOA is strongest in DJF and MAM for the southern hemisphere where cirrus is present in the ITCZ as well as in the West Pacific where deep convection is frequent with effects reaching ~10 Wm^{-2}. These clouds have little effect on the LW flux at the surface, because the cirrus are at high altitudes and low temperatures, emitting very little back to the surface and the emission is masked by intervening water vapor. This causes the SW effect to dominate at the surface, but with very small values in the net being the lowest in DJF of around -1 Wm^{-2}. Similar patterns are found by looking at the annual average with the strongest impacts being in the ITCZ and West Pacific. When averaging the effects globally the transitional seasons have the largest magnitude of radiative forcing (Table 4.2). The cirrus clouds do not add much to the overall picture in terms of forcing, with the only notable value being the TOA LW forcing average of about 1 Wm^{-2} and values of SW at TOA, LW at BOA, and SW at BOA being << 1 Wm^{-2}.

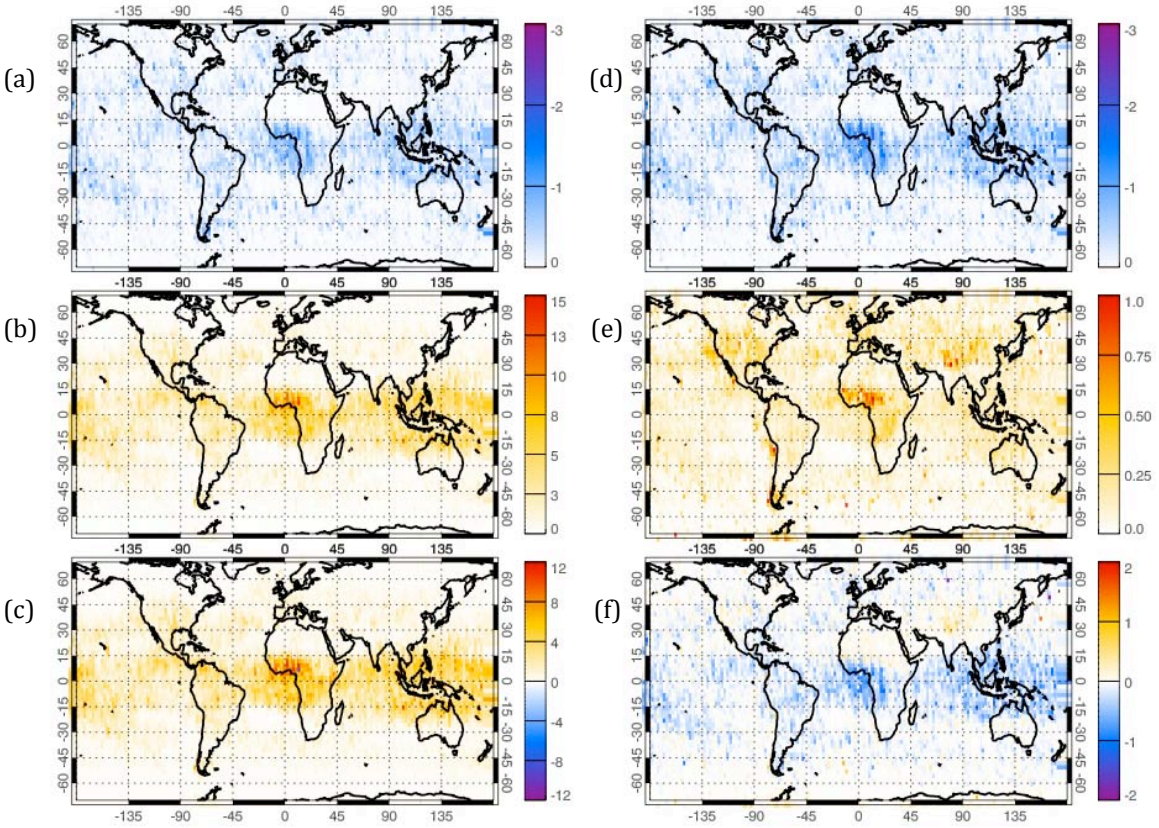

Figure 4.20. The MAM radiative forcing of sub-visible cirrus clouds undetected by CloudSat. The TOA SW (a), LW (b), and NET (c), along with BOA SW (d), LW (e), and NET (f) fluxes are shown, with units in Wm^{-2}.

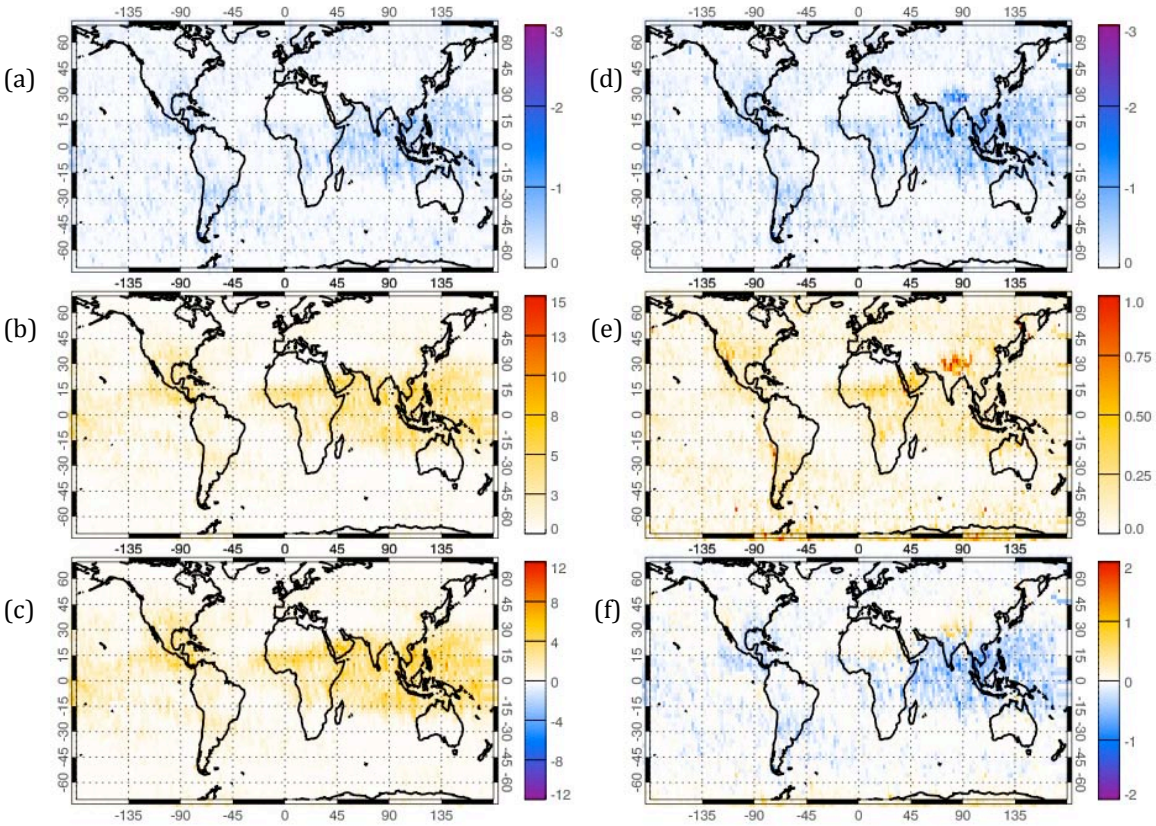

Figure 4.21. Same as Figure 4.20, but for JJA, with units in Wm^{-2}.

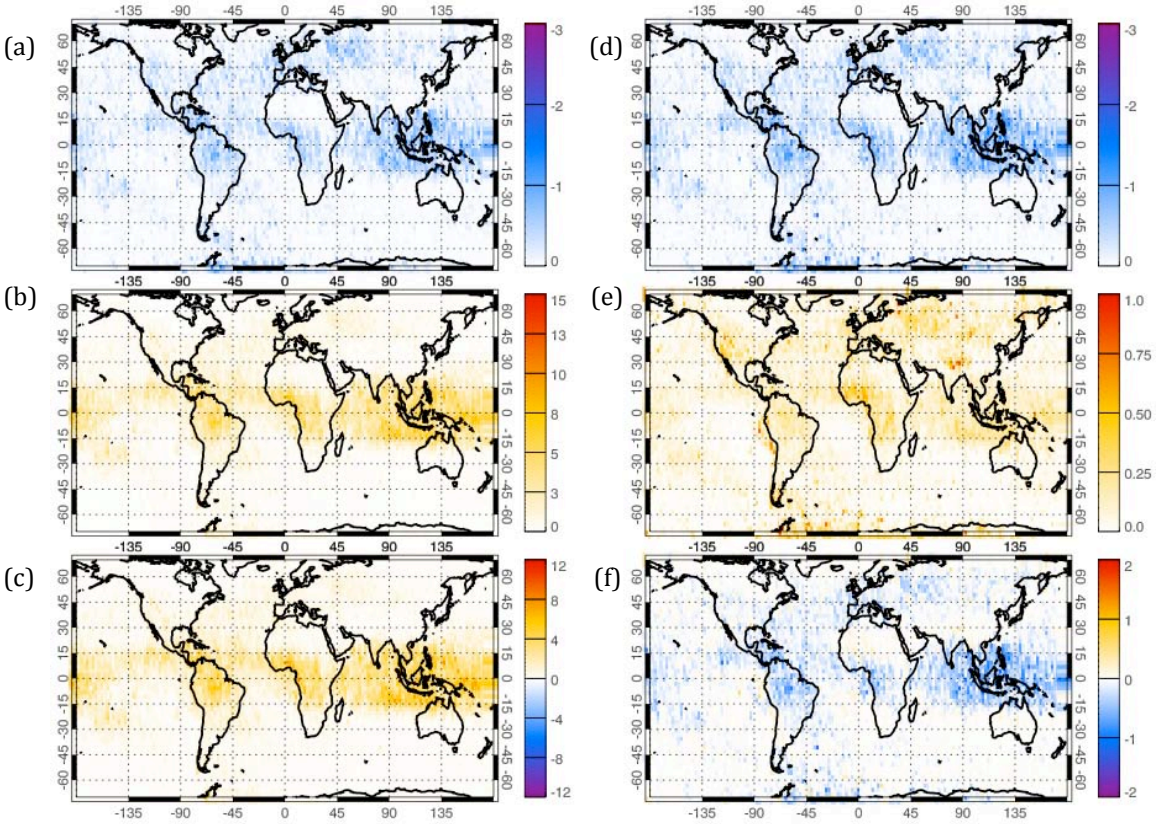

Figure 4.22. Same as Figure 4.20, but for SON, with units in Wm^{-2}.

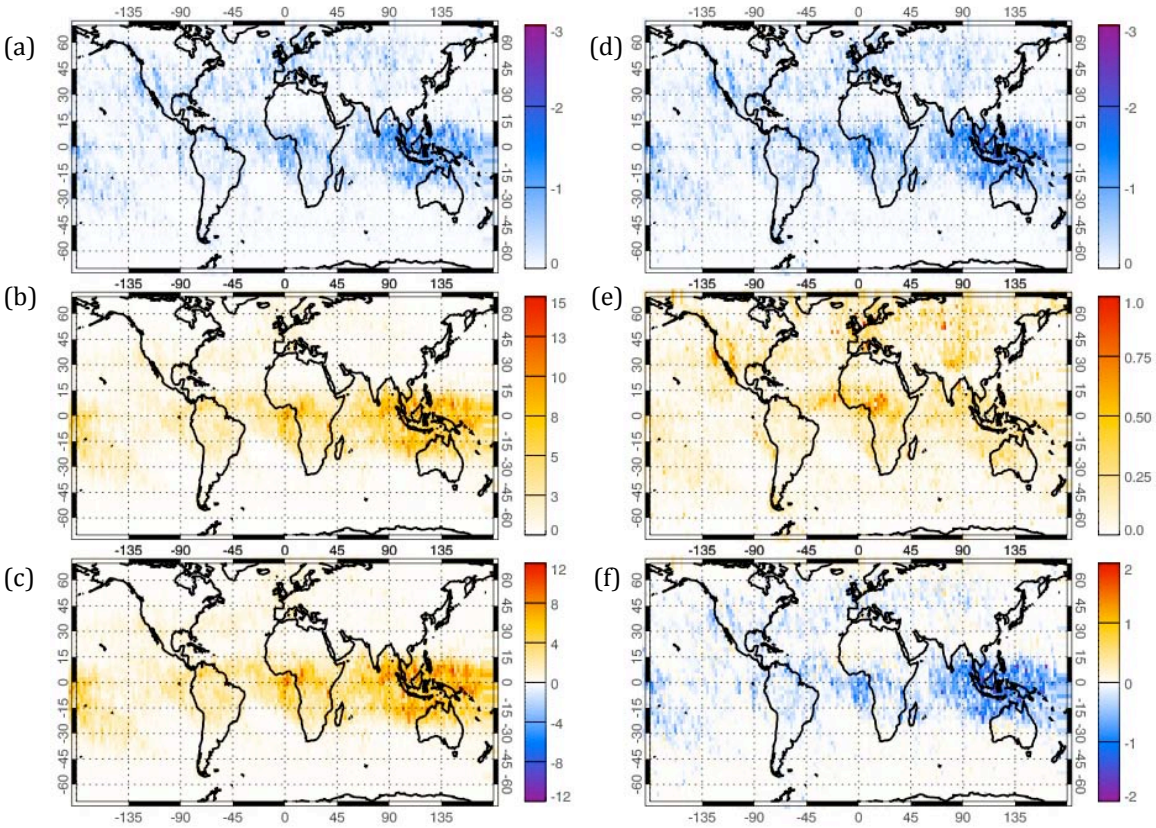

Figure 4.23. Same as Figure 4.20, but for DJF, with units in Wm^{-2}.

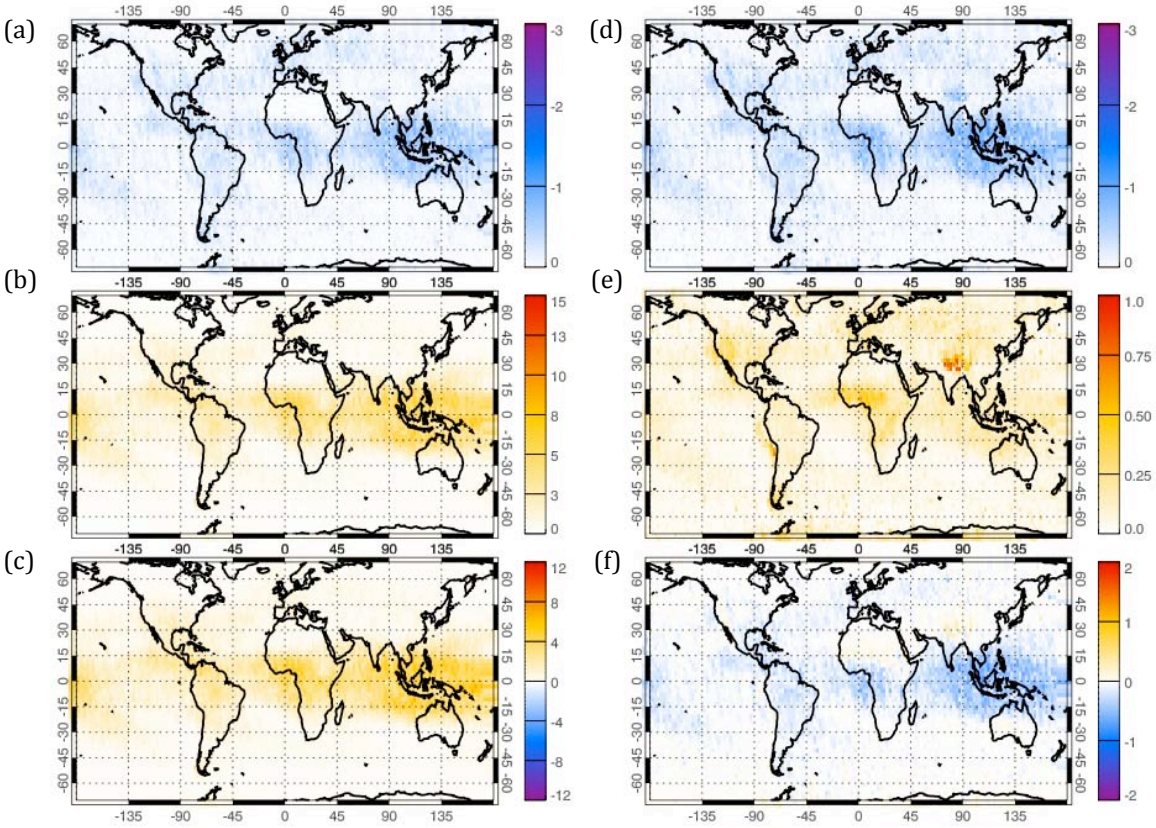

Figure 4.24. Same as Figure 4.20, but annually for the entire period of study, with units in Wm^{-2}.

	DJF	MAM	JJA	SON	ANNUAL
TOA,SW	-0.12	-0.11	-0.09	-0.12	-0.11
TOA,LW	1.06	1.12	0.92	0.90	1.0
TOA,NET	0.94	1.01	0.83	0.78	0.89
BOA,SW	-0.16	-0.16	-0.12	-0.16	-0.15
BOA,LW	0.09	0.10	0.11	0.10	0.10
BOA,NET	-0.07	-0.06	-0.01	-0.06	-0.05

Table 4.2. The seasonal and annual globally averaged radiative forcing of sub-visible cirrus undetected by CloudSat. The TOA and BOA fluxes are shown in SW, LW, and NET, with units in Wm^{-2}.

It is easier to see the overall impacts with the cirrus in the zonal averages of the data (Figure 4.25). The most obvious impact is in the tropics where the cloud forcing peaks near 3.5 Wm^{-2}. For BOA the cloud forcing of undetected cirrus is close to negligible until around 30° N/S where the forcing starts to increase to more negative values. The same can be said for TOA, but there is still some radiative impact in the LW at high latitudes.

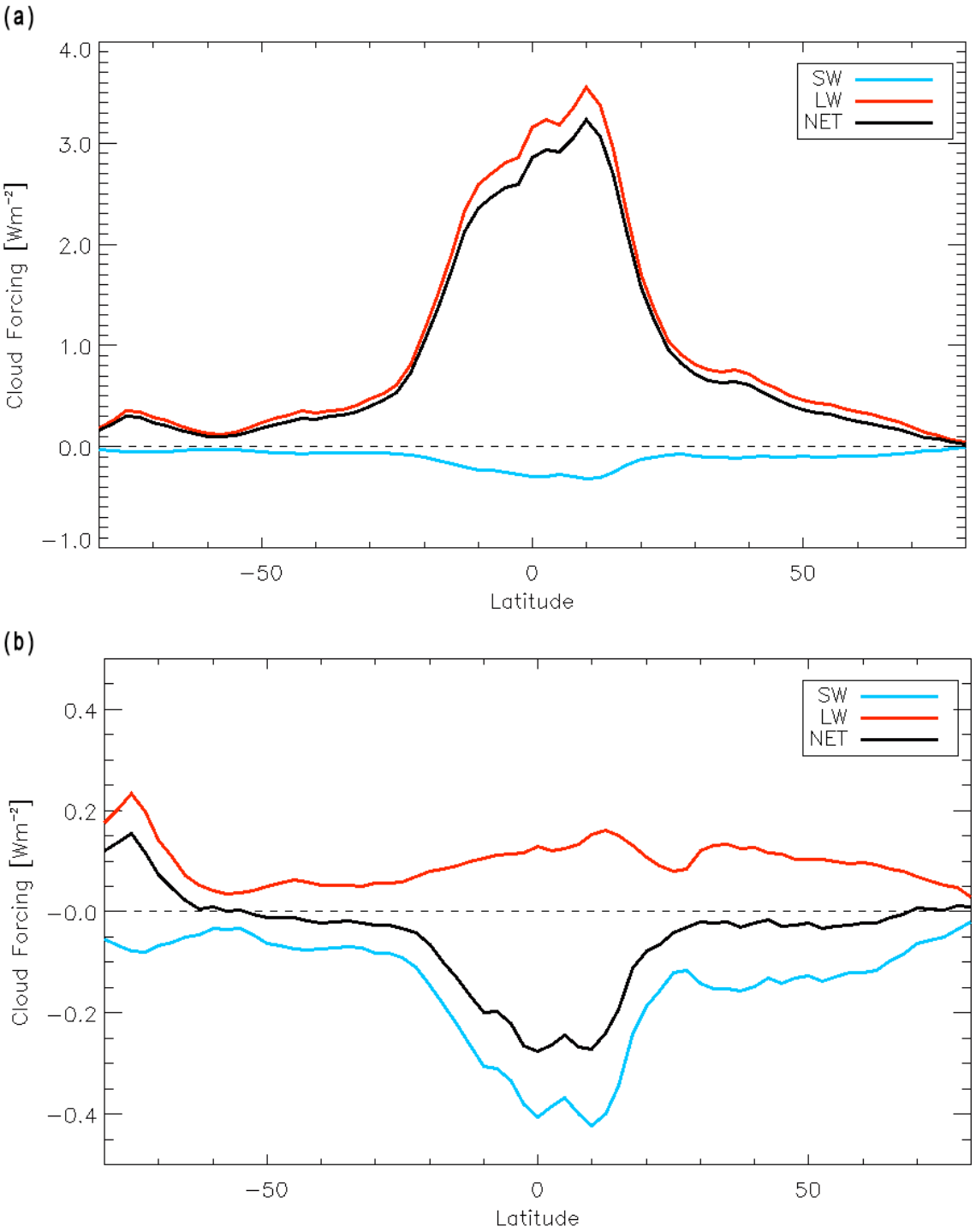

Figure 4.25. Latitudinal averaged radiative forcing of sub-visible cirrus clouds undetected by CloudSat for TOA (a) and BOA (b), with units in Wm^{-2}.

4.2.3 Aerosol Direct Effect

The advantage of using the combined data set in FHR-A is that CALIOP is able to detect aerosol layers within the atmosphere. Using this information the aerosol optical depth has already been calculated, and when combined with SPRINTARS properties, the aerosol direct radiative effect can be calculated. There have been many studies that have observed the effect of aerosol at TOA in the SW both by using satellite and by using atmospheric models (Remer and Kauffman, 2006; Yu et al, 2006; Zhang et al. 2005). All of these studies using satellite measurements employ data from passive sensors and do not have the ability to place the aerosol layers in the vertical and are limited to over oceans with clear skies only where aerosol properties are more readily detected. The direct effect for this study is derived for clear sky over both land and ocean.

The seasonal and annual clear sky SW TOA direct effect of aerosols is illustrated in Figure 4.27. The maximum SW effect is around -40 Wm^{-2} located in regions of dust transport, over the Atlantic and Indian oceans. The seasonal shift of Saharan dust transport can be seen over the Atlantic Ocean with its transport most evident in the northern hemisphere spring and summer months. The strongest effects over North America occur in JJA due to an increase in dust, from drier weather, and pollution.

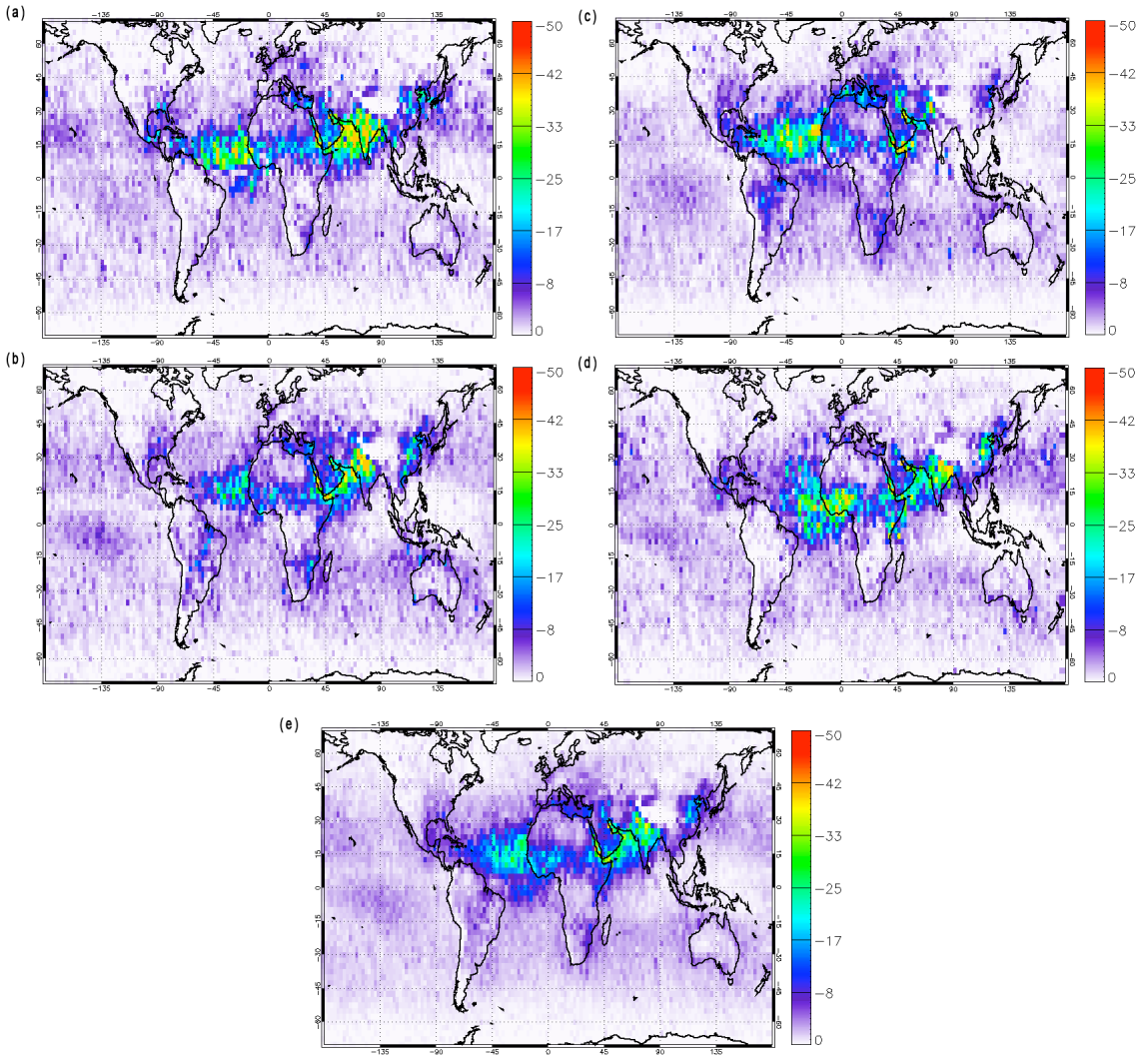

Figure 4.27. The aerosol direct effect for clear sky SW TOA for MAM (a), JJA (c), SON (b), DJF (d), and Annually (e), with units in Wm^{-2}.

Sources of pollution over Eastern China and India are largest in SON and DJF with evidence of transport of pollution over the Pacific Ocean, but the effect is masked in JJA when the Indian monsoon is present. The signal of smoke is not strong, and is expected to be found in JJA and SON. There is a small signal but not of the magnitude expected. This would be due to the fact that the aerosol properties from CALIPSO did not fit perfectly and therefore the radius for smoke aerosols was

made too large. The signal is also lost where low clouds underlie aerosol. Chand et al. (2009) researched the use of all-sky and clear sky and found that during the summer months smoke from burnings are found over low cloud decks in the Atlantic. These smoke aerosols tended to have a positive effect at the TOA in SW and increased in effect as the cloud amount increased below them. The effects of aerosol over land, such as in desert regions, are not as high due to the high surface albedo. An example of this is over the Sahara. Looking back at the aerosol optical depth in Figure 4.7, there are high values of optical depth over the Sahara. These effects of dust are cancelled from the high albedo of the surface. The annual clear sky SW TOA direct effect of aerosol is also shown zonally by latitude in Figure 4.28.

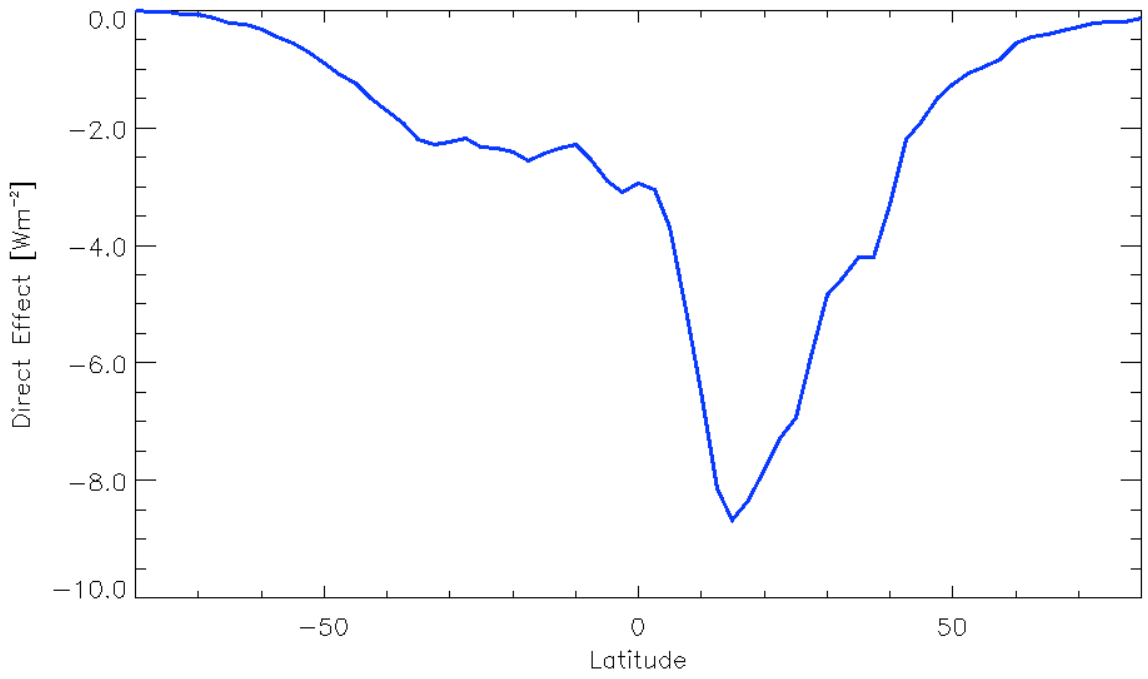

Figure 4.28. The annually averaged zonal direct radiative effect of aerosols, with units in Wm^{-2}.

The largest impact of aerosol is near 15° N where the majority of dust transport takes place across the Atlantic, peaking around -9 Wm^{-2}. The effect of dust is widespread ranging from 10° S to 15 N. Values of around -3 Wm^{-2} are found south of 15° S and are caused by marine aerosol and smoke from burnings in the forests of the Amazon and in southern Africa. The pollution from India and China can be seen in a small peak of -4 Wm^{-2} around 40° N.

The seasonal and annual effects of aerosol can best be compared to other studies by looking at the global impacts (Table 4.3). Annually the effect of in SW TOA aerosol is -2.9 Wm^{-2}, which is similar in magnitude compared to the aforementioned aerosol studies, following the pattern of the seasonal shift in magnitude, with higher effects in DJF and MAM. According to the IPCC AR4 assessment, the average global impact at TOA is around -5 Wm^{-2}. While the number from this study differs, the study from Yu et al. (2006) can help answer why. The aerosol effect is compared with numerous satellite and model sources. Looking at their results the SPRINTARS model exhibits the lowest impact annually of -1.7 Wm^{-2}. This study uses aerosol properties from the SPRINTARS model, so because of this, and the low calculations of bio-mass burning (smoke) the results from this study would be lower than the IPCC reports.

	MAM	JJA	SON	DJF	ANNUAL
Direct Effect	-3.1	-2.8	-2.8	-3.0	-2.9

Table 4.3. The direct effect of aerosols in the SW at TOA, with units in Wm^{-2}.

4.3 The Global Radiation Budget of Earth

4.3.1 Total Cloud Forcing

The total cloud radiative effect (forcing) is now evaluated. The cloud forcing is averaged by viewing all clouds detected by CloudSat and CALIPSO calculated for each season and annually (Figures 4.29-4.33). The seasonal shift in cloud is readily apparent in these figures. The ITCZ can be seen as a minimum in the tropics in both Net at TOA and BOA, and moves further north in JJA and south in DJF. The impact of low clouds at high latitudes during winter in each respective hemisphere appears in the BOA LW and the Net BOA with positive values closer to the poles. More wide spread areas of low cloud effect are in the subsidence regions in the sub-tropics where now all low clouds are observed. Impacts of the mid-latitude storm tracks are visible in the fluxes for all seasons, but most prominently in the transitional seasons. These results resemble those documented in past studies using ERBE (Gupta et al, 1993 and Harrison et al. 1990), these studies and Raschke et al. (2005) and are summarized in Table 4.4.

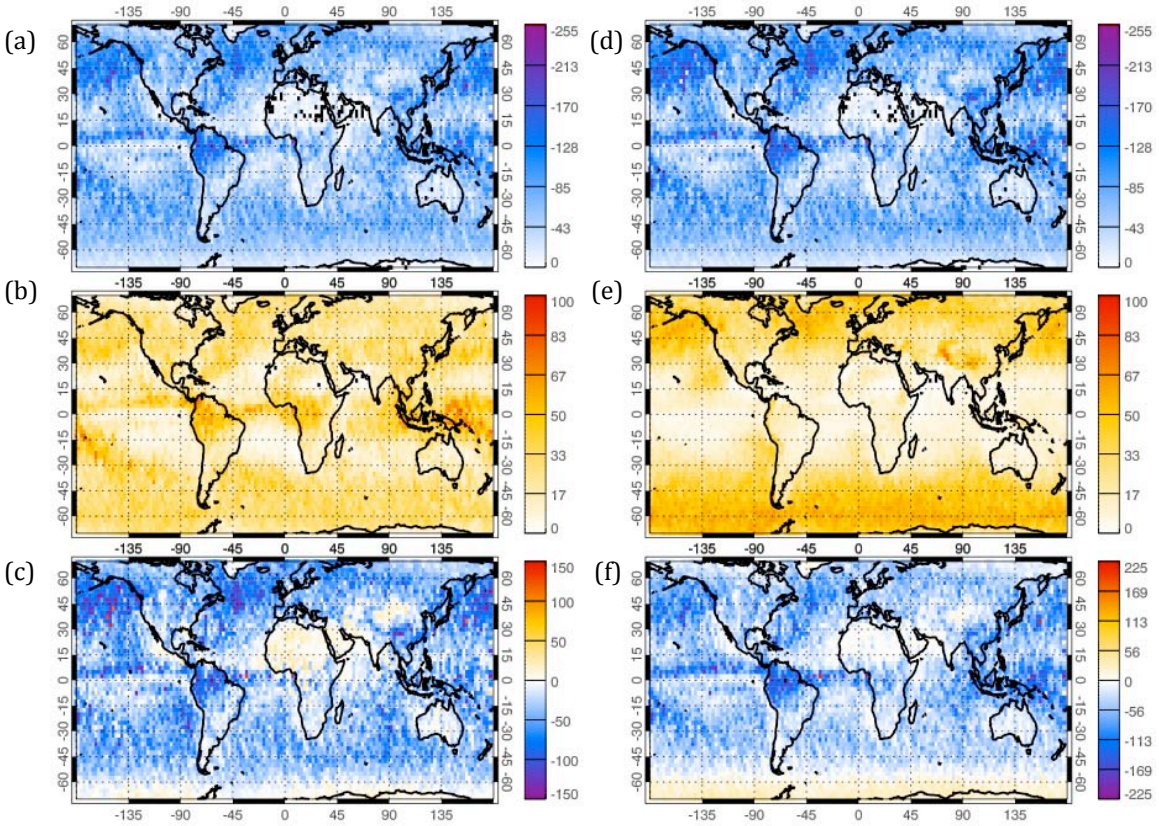

Figure 4.29. The MAM radiative forcing of all clouds detected by CloudSat and CALIPSO. The TOA SW (a), LW (b), and NET (c), along with BOA SW (d), LW (e), and NET (f) fluxes are shown, with units in Wm^{-2}.

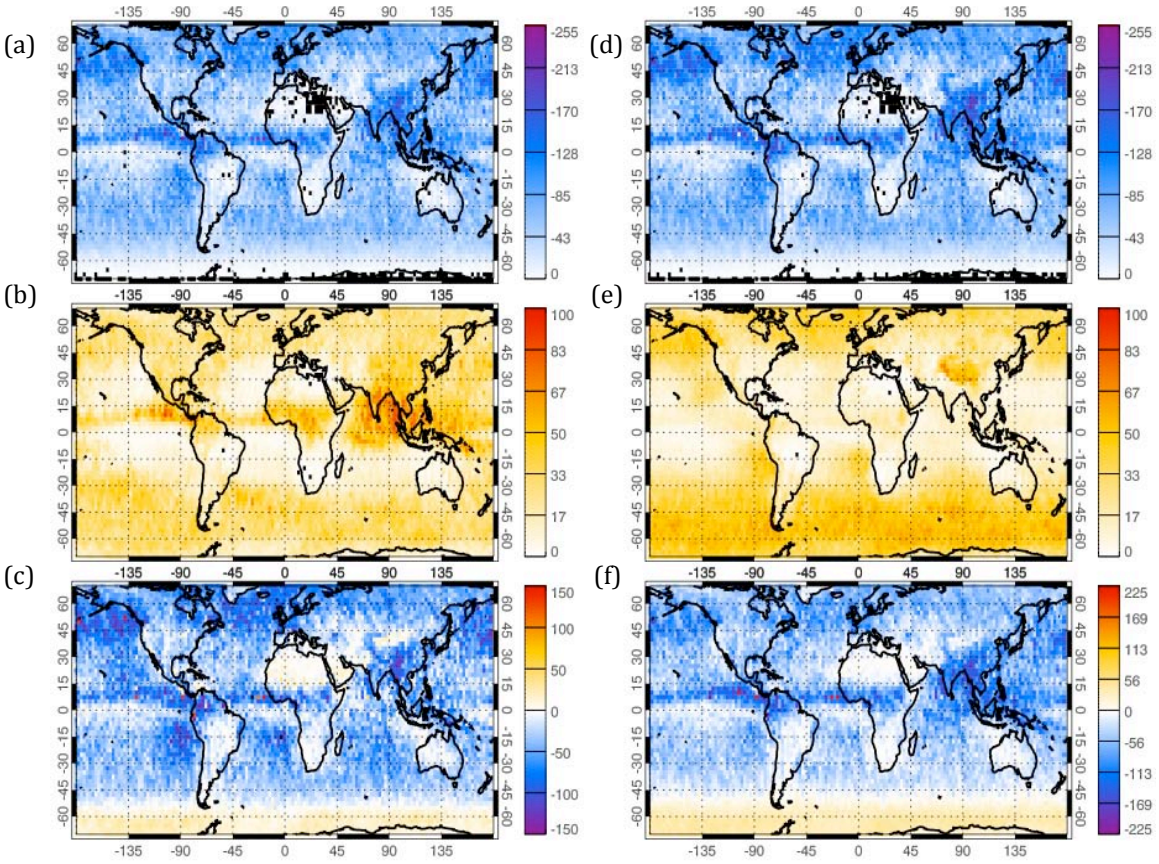

Figure 4.30. The same as figure 4.29, but for JJA, with units in Wm^{-2}.

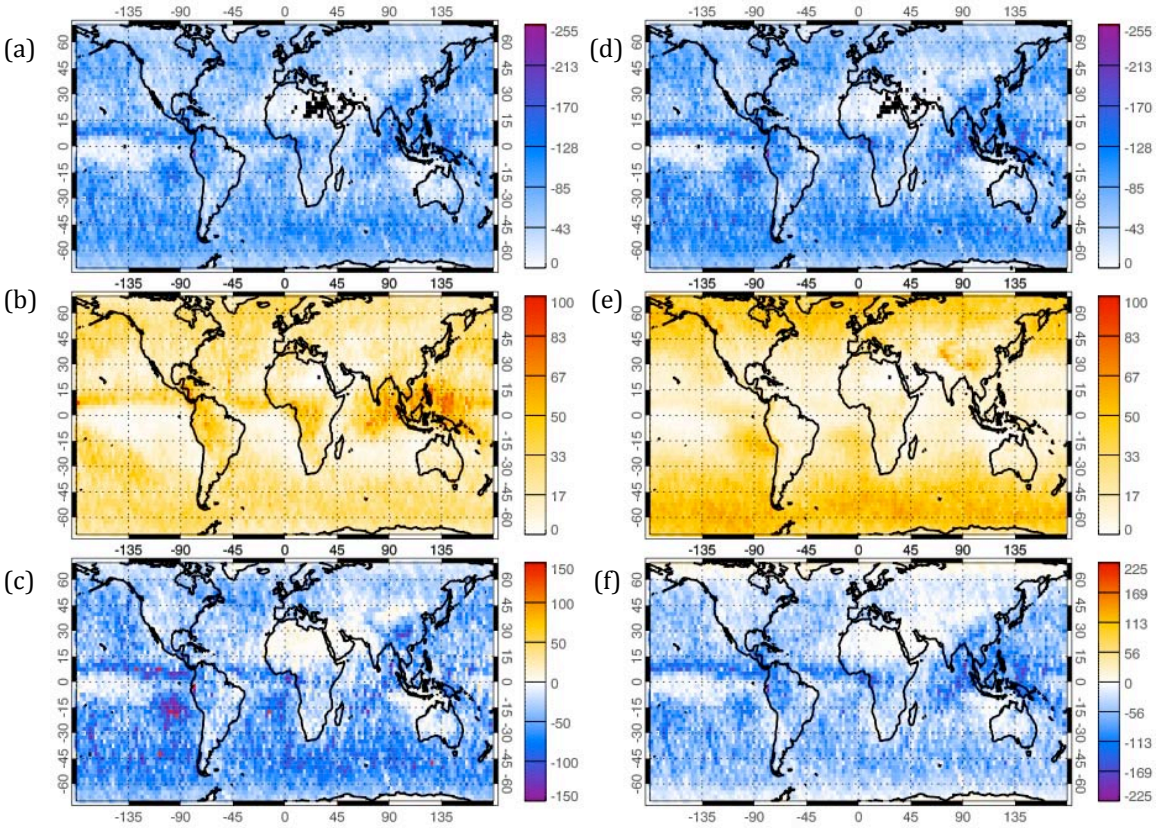

Figure 4.31. The same as figure 4.29, but for SON, with units in Wm^{-2}.

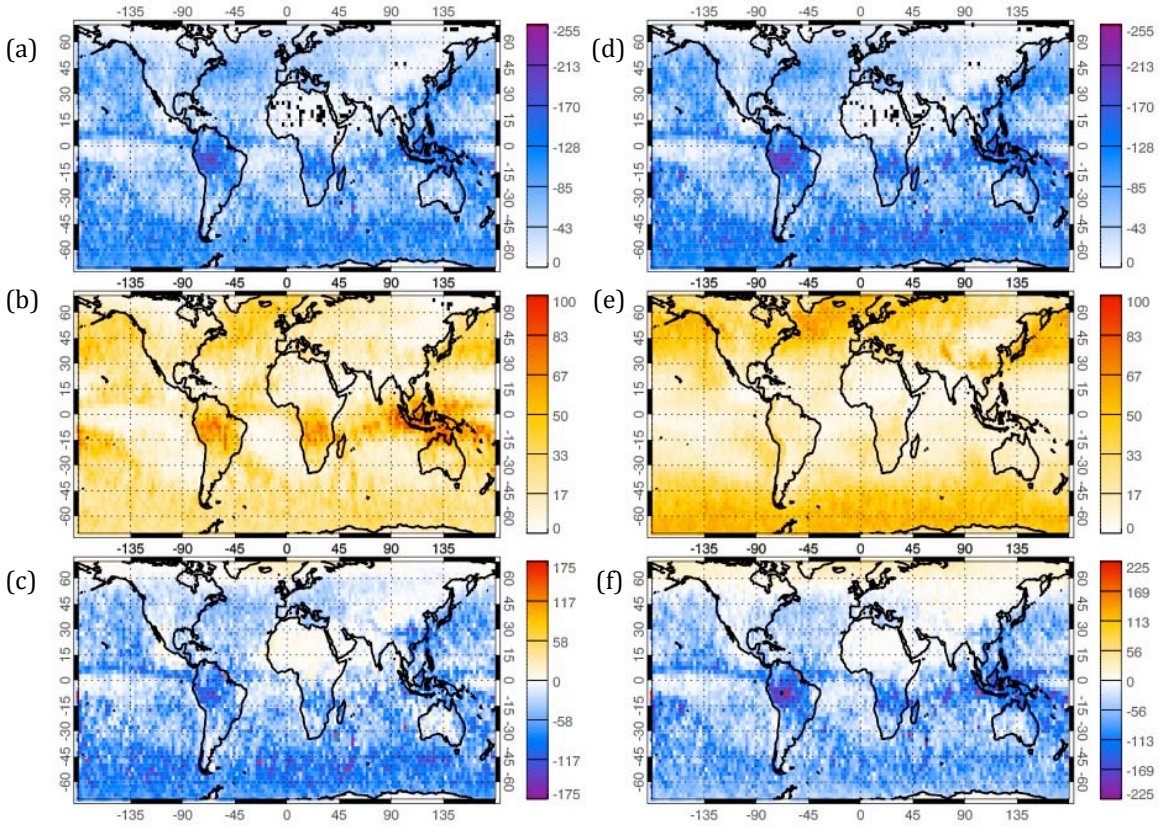

Figure 4.32. The same as figure 4.29, but for DJF, with units in Wm^{-2}.

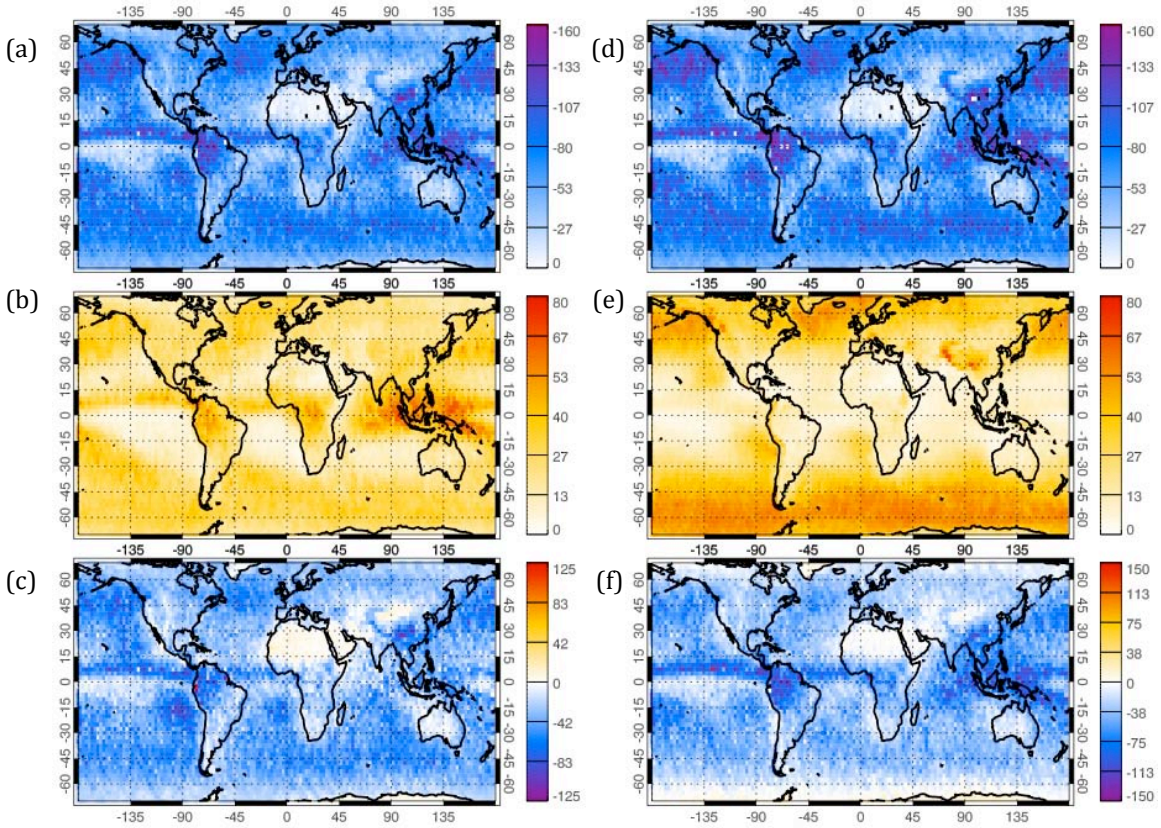

Figure 4.33. The same as figure 4.29, but for annual average with units in Wm^{-2}.

	DJF	MAM	JJA	SON	ANNUAL
	-46.7	**-43.0**	**-42.8**	**-46.2**	**-44.7**
TOA,SW	-53	-46	-50	-50	-50
	-51.7	-45.1	-46.7	-50.1	-48.4
	24.5	**25.3**	**24.6**	**24.3**	**24.6**
TOA,LW	25	26	25	25	25
	30.6	**31.3**	30.1	32.2	31.1
	-22.2	**-17.7**	**-18.2**	**-21.9**	**-20.1**
TOA,NET	-28	-20	-22	-26	-24
	-21.1	-13.8	-16.6	-17.9	-17.3
	-54.9	**-50.7**	**-50.2**	**-54.0**	**-52.5**
BOA,SW	-57	49	-50	-53	-52
	--	--	--	--	--
	23.8	**23.6**	**22.6**	**24.0**	**23.6**
BOA,LW	31	30	28	30	30
	--	--	--	--	--
	-31.1	**-27.1**	**-27.6**	**-30.0**	**-28.9**
BOA,NET	-26	-20	-21	-24	-23
	--	--	--	--	--

Table 4.4. The seasonal and annual globally averaged clouds detected by CloudSat and CALIPSO. The fluxes from FHR-A are shown first in bold print, followed below by the fluxes from Raschke et al. (2005) and Harrison et al. (1990). The TOA and BOA fluxes are shown in SW, LW, and NET, with units in Wm^{-2}.

Annually, at TOA -44.7 Wm^{-2} is reflected from cloud and 24.6 Wm^{-2} is trapped in LW resulting in -20.1 Wm^{-2} in radiative cooling from clouds. The values of forcing fit into the ranges of the above mentioned studies, with TOA net forcing sitting between Harrison et al. (1990) (ERBE) and Raschke et al. (2005) (ISCCP) who find forcings of -24 Wm^{-2} and -17 Wm^{-2}, respectively. The LW values from this study match closely to ISCCP at TOA, but are much smaller at BOA from the higher value of downwelling radiation from this study. The seasonal trends follow the above studies with the largest radiative forcing in DJF and lowest during MAM. The annually averaged forcing can be seen by latitude in Figure 4.34.

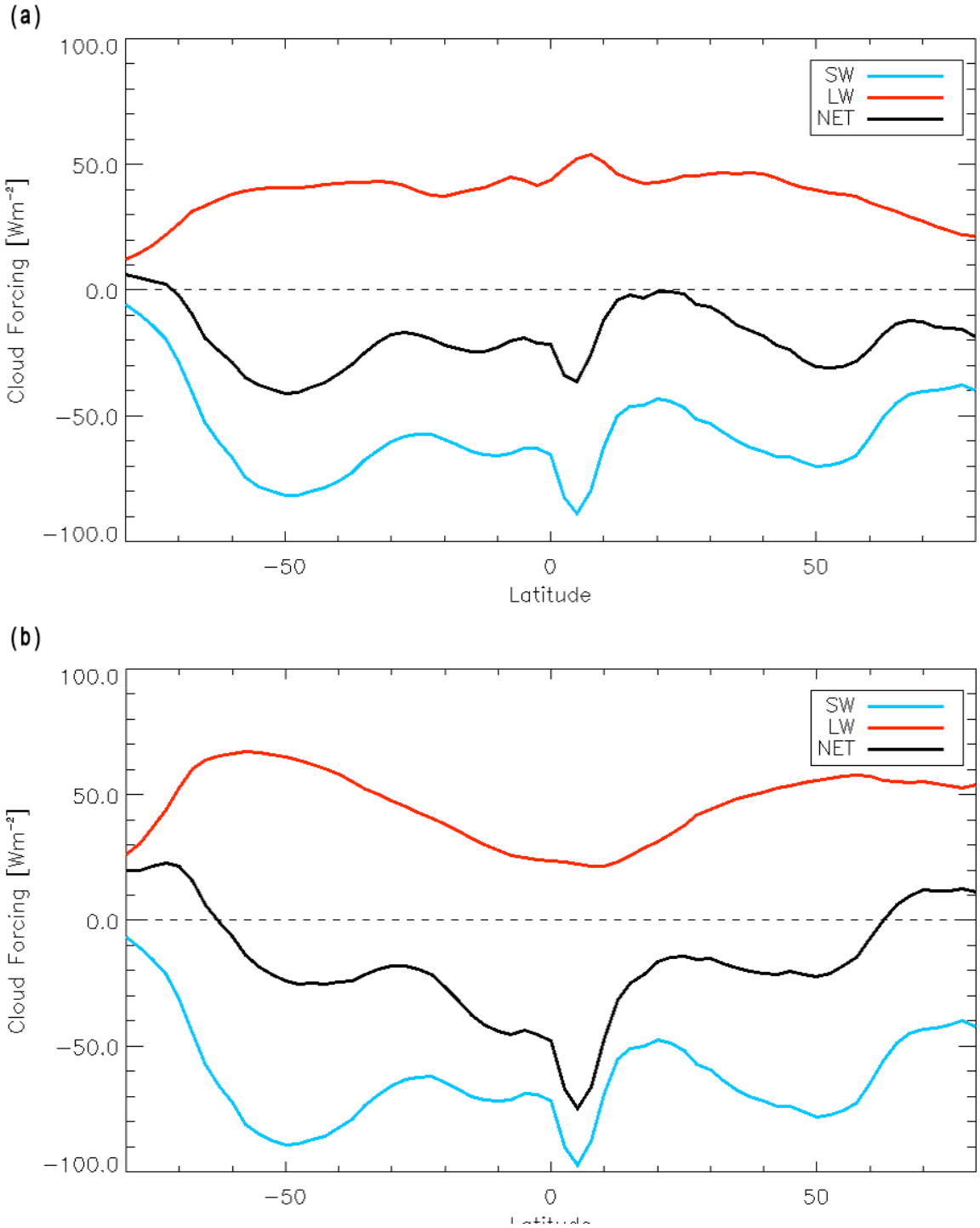

Figure 4.34. The latitude averaged cloud forcing from all clouds detected by CloudSat and CALIPSO at TOA (a) and BOA (b), with units in Wm^{-2}.

The effects of cloud distributions on these fluxes are inferred zonal averages of cloud forcing. The ITCZ is visible in the peaks in the tropics in TOA and BOA SW and the overall net forcing. The bimodal peaks in the TOA LW show the shift in the ITCZ between the hemispheres. The minimum of LW at BOA near the tropics and subtropics is possibly from the large amount of water vapor obscuring effects of clouds (eg Stephens et al., 1994). The peaks at the mid-latitudes are due to clouds in mid-latitude storm tracks, which are more extensive in the southern hemisphere.

4.3.2 Earth Radiative Balance

The TOA, BOA, and NET fluxes at the top and bottom of the atmosphere are shown in Figure 4.35.

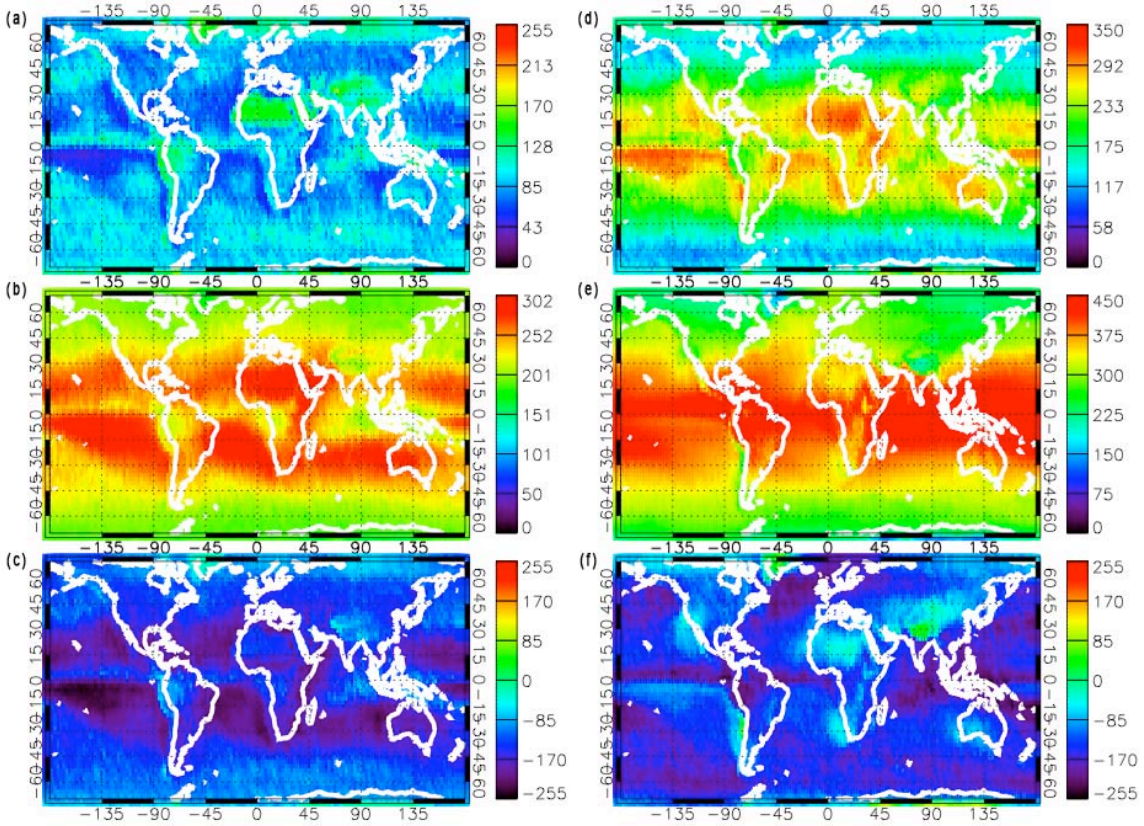

Figure 4.35. All-Sky radiative fluxes for TOA SW (a), LW (b), NET(c), and BOA SW (d), LW (e), NET (f). Units are in Wm^{-2}.

Areas of persistent cloudiness, high clouds, deserts, and areas that areas that are on average annually covered with snow or ice are evident in the SW TOA. The ITCZ can be seen in the LW TOA as a minimum across the tropics, but not in LW BOA as the cloud tops emit much less at the colder cloud top heights and water vapor masking this emission. Overall, the panels show good agreement with that of the ISCCP FD data, which can be found in Figure 4.36. More information on the ISCCP figures can be found at http://isccp.giss.nasa.gov/projects/browse_fc.html.

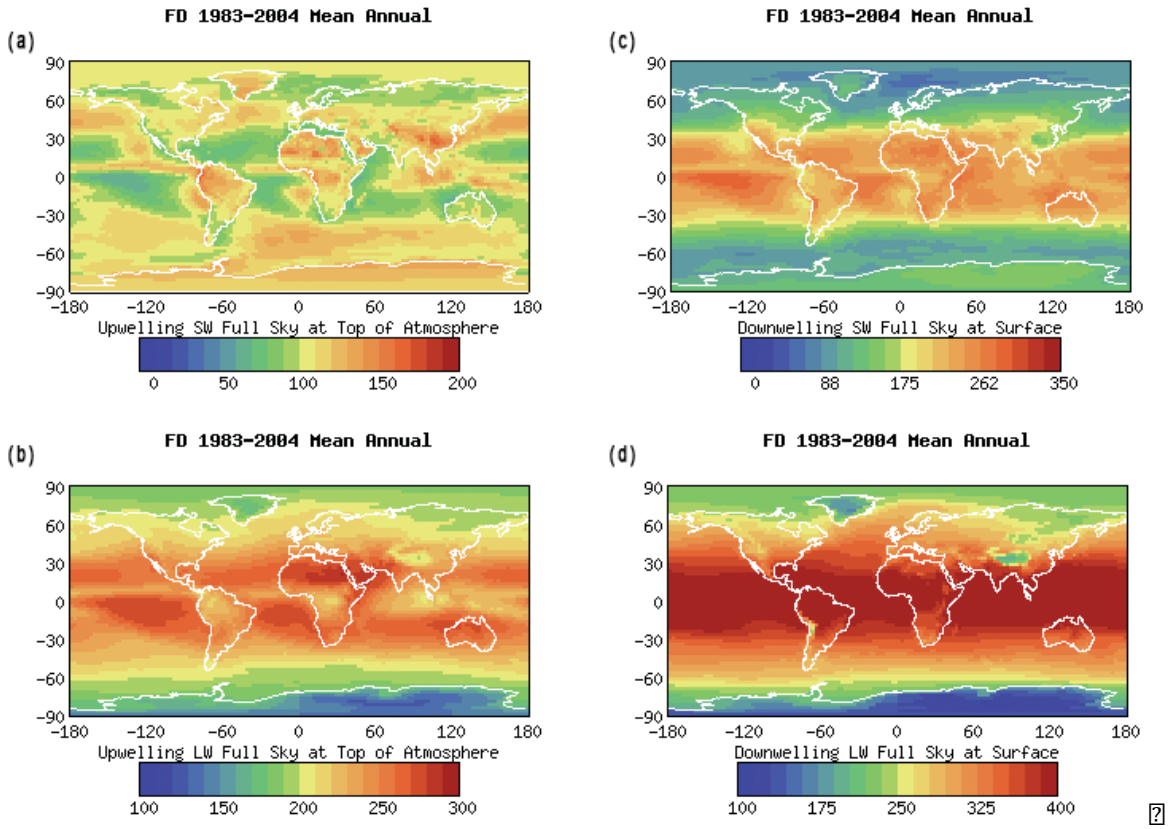

?SHBR?? i1Gi??? Ae' - ?IABM?' ?IABM?' ?ILR????????? s?ou??? s?ou??W?????????? s?ou??? s?o?
D? ?W?IRLN ??????????????D?i??WSD)??R?SW?? N e0i?

?

?

??E??R??S?DSC???IABM?' ?IRLN ?DE?????e????D????R???C?R?H????LC?R?DE???WDSR?O?RSL??
L'T?DB?-?s??WB?R-?0,,ke???RB?R-?0,,wo?DL???RSC????HAL??A??WWB?A?R??S?DSLW??B?H?D??
?SN SA?R?DL?DE????S?HR?N'?'??W?SW??SLB?s2660o??W????R?W??RDE???D??A?s0,,6o?DE??
R??S?DSLW??B?H?DAL'T?DE????RDE???W????R?OR'?WDE????-?DE???S?HR?N ???WASW??SHBR?? i1ki??
?L?N ? ?DES?SHBR?DE??IABM?'??D?????W???????ILR??LDE??? ??W???? ??R??F?SHED????-?
?R????ILR?DE??A?DSDB???'?L'T?ew05?????W??w05??b??E??N SWSN BN ??W??N ?MSN BN ?A?DSDB???'?
L?'?RC?????-??ALB????D????E????? ?IABM?'?IRLN ?DE?????e????D??N B'D?????WLRN ?ASV???SW?
'LN ??F ?-??????B'??L'T?DE??BWe'-W?ERLWLB'?LR?SDAL'T?DE???e?R?SW?'?DEASD?'i???L??LDES?
DE????? ?IABM?'??R??WLRN ?ASV???SW?????E??ALB????D??SW??-?DE???C?R?H????SA?SW'LA?DSLW?

over the Earth by latitude and day. This normalization allows the SW fluxes to act similarly if a diurnal cycle was present in the data. This of course does not change the albedo of the cloud, thus a full representation of the diurnal cycle still does not exist. This can be seen in the TOA radiative balance of the ERB system in Figure 4.37. The outgoing SW radiation is much less than observed in other ERB studies and has to do with the low solar zenith angle present during the A-Train observations. When the sun is higher overhead, the albedo of a cloud is less than if the zenith angle were higher (closer to horizon). Therefore, the outgoing SW radiation will be smaller than expected. This is especially evident in that the system is not closed at TOA and is off by ~25 Wm^{-2}. A similar feature at the TOA that is different than others versions of this diagram is the incoming solar radiation of 352 Wm^{-2}. This is due to the fact that the A-Train does not pass completely over the poles, and thus the entire Earth is not sampled. It is a feature that is common to sun-synchronous satellites such as ones in ERBE which also measured similar incoming solar at TOA. The outgoing SW radiation at TOA is 92 Wm^{-2}, smaller than expected due to the diurnal error in measurement mentioned above. Outgoing LW radiation is calculated to be 235 Wm^{-2}, which remains consistent with past studies (Ellis and Vonder Haar, 1976; Stephens et al., 1981; Harrison et al., 1990, Rossow and Zhang 1995). Longwave emission from the surface agrees closest with Trenberth et al. (2009) with 398 Wm^{-2} and also confirms another point from the Trenberth et al. (2009) paper. They say that there has been a lot of uncertainty in the number that needs to be used for the downward LW radiation at the surface, and that more information was needed about cloud height in order to back this up.

This study has information on cloud base height and has calculated a value of 349 Wm^{-2}, which is much higher than their estimate of 333 Wm^{-2}. This has been stated to be higher in newer studies in ISCCP (Raschke et al., 2005) and recent numbers from the GEWEX Surface radiation budget project of 347.5 Wm^{-2} (Through personal communication). Looking at the difference between the upwelling and downwelling LW radiation an atmospheric cooling of -187 Wm^{-2} is calculated; higher than those found in Hartmann (1994), L'Ecuyer et al. (2008), and Trenberth (2009), who show a range of 168-178 Wm^{-2}, but closer to numbers from Raschke et al. (2005) who state -183 Wm^{-2}. The increase would be from more accurate locations of low stratocumulus clouds increasing the downward LW radiation at the surface. The same can be calculated for the SW with a warming of 63 Wm^{-2}, fitting well with the above-mentioned studies ranging from 58-71 Wm^{-2}. Uncertainties in fluxes are calculated by observing the RMS error differences between FHR-A and CERES FLASHFlux TOA and surface fluxes (similar to Section 4.4, but at a coarser resolution) along with estimated uncertainty in the surface albedo and emissivity. The fluxes are averaged into four quadrants of the Earth separated by the Equator and Prime Meridian for each 3-month season. The seasonal averaging allows four different estimates of uncertainties of flux measurements at the TOA and surface. Uncertainties within the atmosphere are calculated from the combinations of the surface and TOA fluxes used to derive the atmosphere flux convergence, and uncertainties in the aerosol effect are represented by the range of values in the previously mentioned aerosol studies and the IPCC AR4 report. The highest uncertainty lies in the SW measurements within the atmosphere and at the surface.

Uncertainty in the downwelling LW radiation at the surface falls within range of the previously mentioned newer studies, but still greater in magnitude than measurements derived from past passive satellite studies.

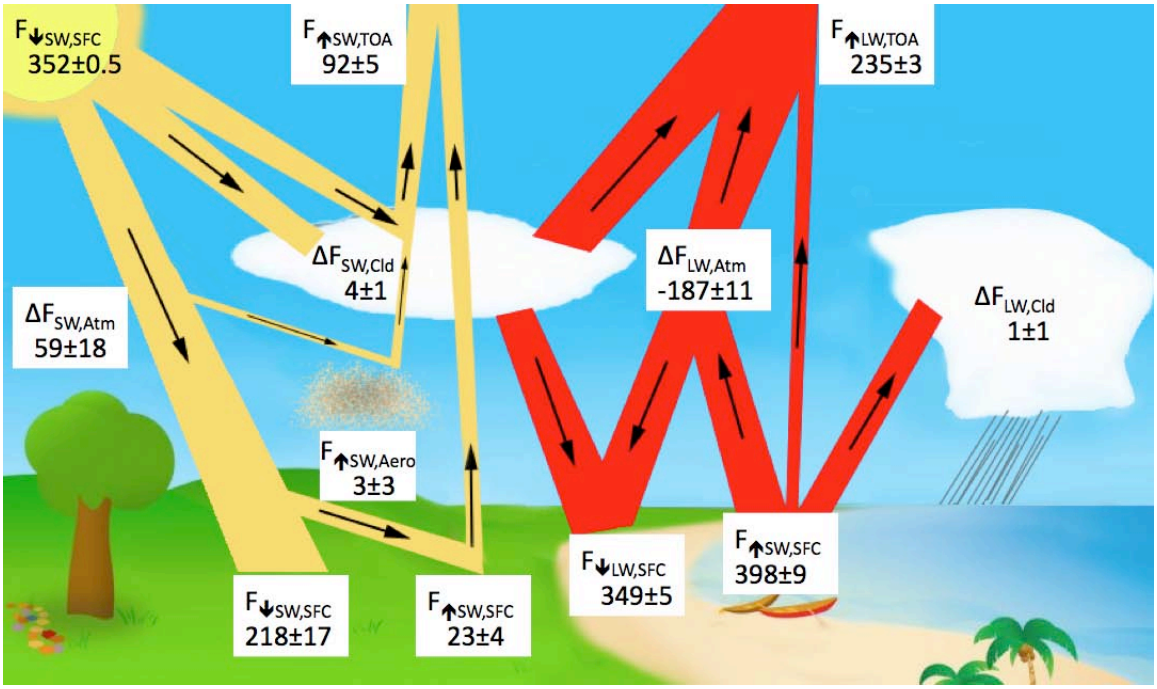

Figure 4.37. The annually average ERB for the period of study. Fluxes are represented by $F_{SW/LW}$, Heating from the atmosphere is notated as $\Delta F_{Atm,SW/LW}$ or cloud as $\Delta F_{Cld,SW/LW}$. Longwave cooling from flux divergence is notated as $\Delta F_{atm,LW}$. All units are in $Wm^{-2.}$

To continue the study, an experimental run of FHR-A was completed to attempt a representation of the solar diurnal cycle. To do this the same properties are for cloud and aerosol are used, but the solar zenith angle is changed every 12 CloudSat bins. The first bin will be the actual time of observation, but the 11 after will increase the solar zenith 2 hours for each bin. This method will not change the meteorological properties of the atmosphere, but will increase cloud and aerosol albedo as solar zenith angle increases. The resolution of the data is technically

reduced to about 14 km, but this is still high enough resolution to solve the global radiative budget. The results of this study in a similar diagram as above are shown in Figure 4.38. Uncertainties for the diurnal cycle FHR-A are based off RMS error differences between FHR-A and CERES FLASHFlux for the full time of day.

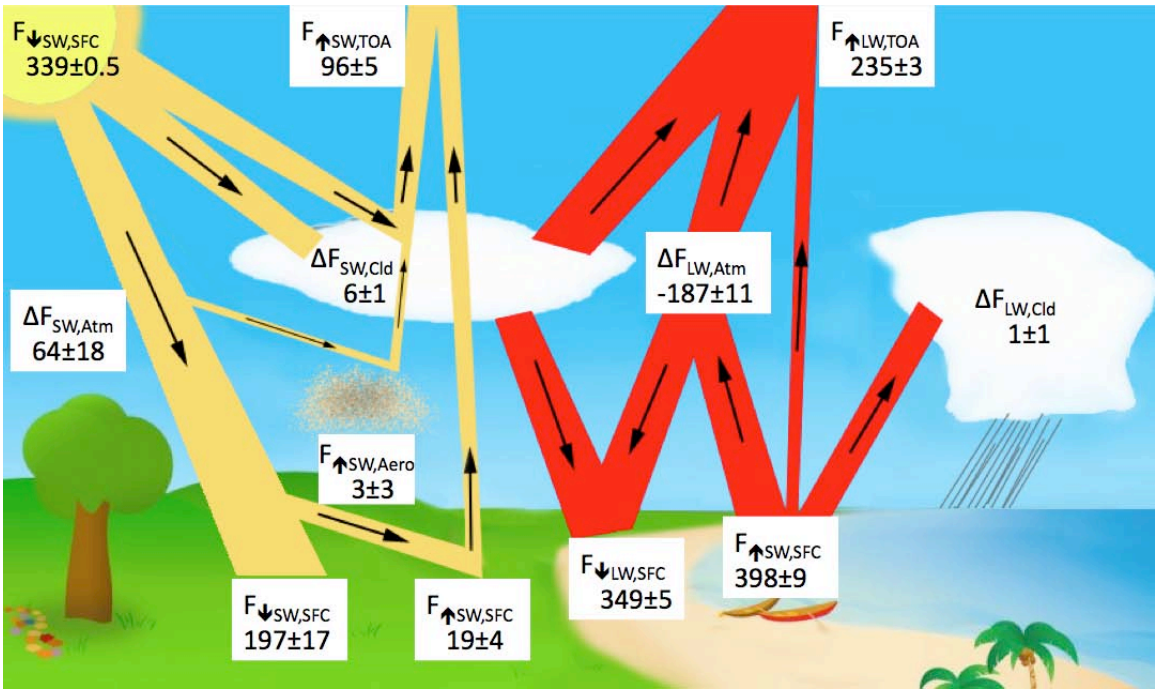

Figure 4.38. The annually average ERB for the period of study simulating a diurnal cycle. Fluxes are represented by $F_{SW/LW}$, Heating from the atmosphere is notated as $\Delta F_{Atm,SW/LW}$ or cloud as $\Delta F_{Cld,SW/LW}$. Longwave cooling from flux divergence is notated as $\Delta F_{atm,LW}$. All units are in $Wm^{-2.}$

The results of the diurnal cycle show increased solar reflection with outgoing SW radiation increasing to 96 Wm^{-2}. The incoming solar at TOA and BOA have decreased, closing the TOA radiative budget within 9 Wm^{-2}. The change in longwave radiation due to varying the Sun's zenith angle had a negligible effect. The outgoing radiation at the TOA is smaller than the ISCPP study. The smaller amount of radiation can be accounted for by the low cloud detection from CALIOP. Using the

high confidence flag has limited the amount of low clouds and aerosol used in this study, thus underestimating the reflected solar radiation from cloud. Other possible errors can be explored by comparing the FHR-A database to other products.

4.4 Validation

This section will focus on how the data created from this research was validated against other radiation budget studies. One of these is the CERES instrument aboard the Aqua satellite providing an excellent dataset to compare with the outgoing and surface fluxes calculated from FHR-A. As explained earlier, the Aqua satellite orbits closely with CloudSat and therefore when comparing data, nearly the same clouds, surfaces, and atmospheric conditions will be viewed by both instruments. The fluxes calculated in this study from CloudSat and CALIPSO observations will evaluated with the CERES FLASHFlux product (Stackhouse et al, 2006). The fact that the CloudSat and CALIPSO calculated fluxes are very unique, and no other data has the vertically distributed fluxes, the differences between the products will present the best evaluation of this research. To compare the two products fluxes at the top and bottom of the atmosphere were averaged into 5° x 5° latitude/longitude grids. The CERES data was collocated to the CloudSat footprint in the same fashion as with the CALIPSO data. The data were compared for the study of January-December 2007, and compared bin to bin as shown in Figure 4.38. Each mark on the figure represents one of the 5° x 5° averaged grid boxes. The bias and RMS

errors for the entire data period are also in the figure. The outgoing shortwave (OSR) and longwave (OLR), and the surface shortwave (SSR) and longwave (SLR) are used in the comparison.

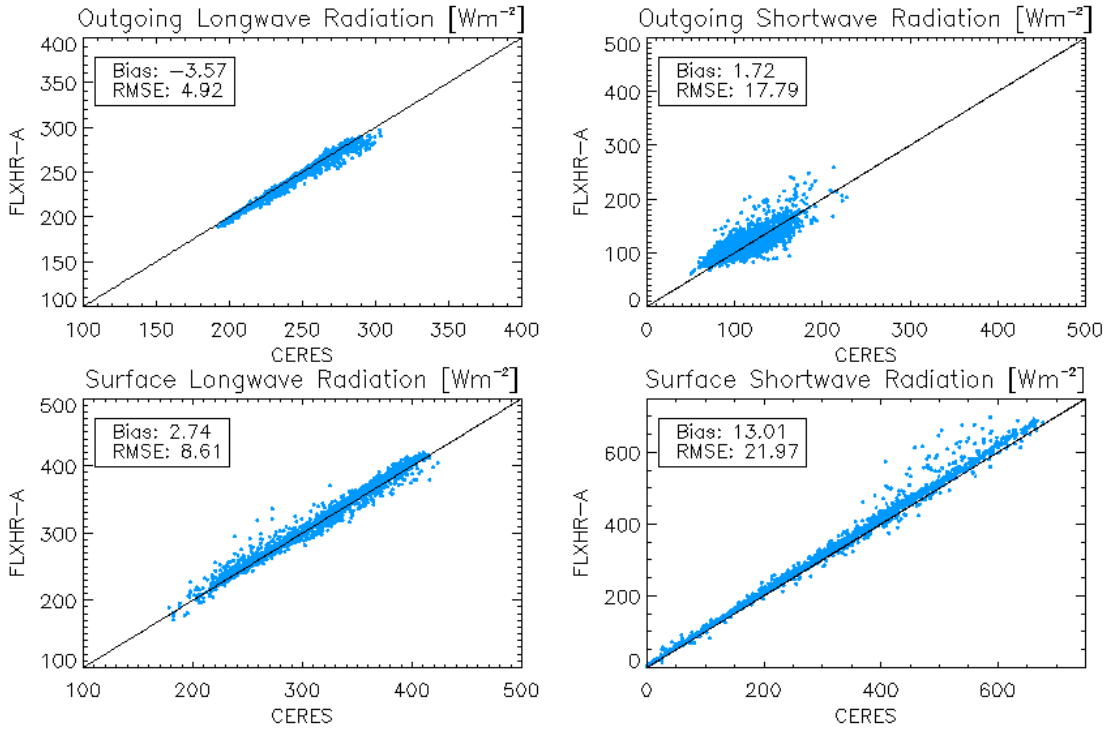

Figure 4.38. Scatter plot showing the comparison of the fluxes from this study to the CERES FLASHFlux product from January 2007 to December 2007. Each point is averaged to a 5 x 5 degree latitude/longitude grid box and contains outgoing and surface LW radiation, and outgoing and surface SW radiation.

The RMS errors in the outgoing radiation are 4.9 Wm^{-2} for the LW and 17.8 Wm^{-2} in the SW. The OSR error is higher due to the spatial differences in the resolution, with CERES having a footprint of 20 km, while CloudSat has a footprint of just over 1 km. The lower biases of -3.6 and 1.7 Wm^{-2} are signs that the data from this study correlates well with the CERES FLASHFlux product. Looking back at Figure 1.3, the errors from comparing 2B-FLXHR with CERES can be compared to FHR-A. Although, the physical properties of clouds and other factors have been

altered in this study, it is good to see improvement in the outgoing SW and surface LW with lower RMS and biases. The increased scattering for surface SW, as well as the slightly increased errors would have to be due to the introduction of newer low clouds and that many have been given properties defined as climatological values. The properties of these clouds are going to be different than the values of cloud used in the CERES model to estimate surfaces fluxes, so scatter and error in the surface estimates is expected. Another factor to consider is the number of data points being used. The surface data for CERES has many missing values and lowers the amount of data points to compare. This will also in essence cause scatter compared to outgoing radiation if less points are being averaged.

It is important to test the product against more than one source of data to test its validity. The fluxes at TOA and BOA are also compared to ISCCP FD fluxes in the same manner as the CERES fluxes (Figure 4.39). The errors seen in the ISCCP comparison are higher, but is to be expected because the ISCCP data is in a 2.5 degree resolution grid, and filed every three hours. Therefore, in order to best match the data from the CloudSat latitude and longitude, it must be matched to the closest grid box, as well as the closest 3-hour interval. The closest error is in the OLR with a Bias of -2.4 Wm^{-2} and RMS of 6.6 Wm^{-2}. The other comparisons in OSR, SLR, and SSR, however, are much worse. The OSR has a bias of -46.3 Wm^{-2} and RMS of 70.2 Wm^{-2}, which can be reflected in the SSR having a positive bias of 39.9 Wm^{-2} and RMS of 111.3 Wm^{-2}. The SLR has a larger negative bias, and what seems to be a more negative slope associated with it.

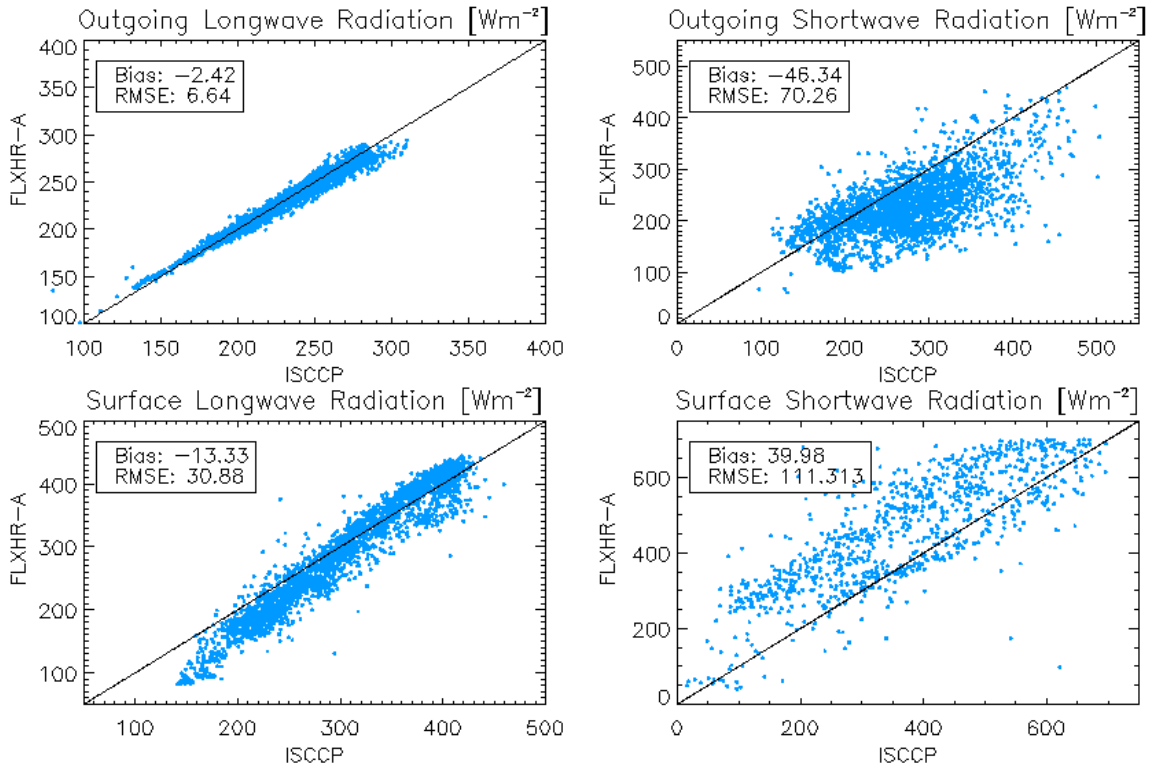

Figure 4.39. Scatter plot showing the comparison of the fluxes from this study to the ISCCP FD product from January 2007 to July 2007. Each point is averaged to a 5 x 5 degree latitude/longitude grid box and contains outgoing and surface LW radiation, and outgoing and surface SW radiation.

Finally, the FLASHFlux product along with ISCCP FD fluxes are compared to each other (Figure 4.40). A similar pattern overall is found with CERES and ISSCP as seen by the comparison with this study and ISCCP. Though, similar trends are seen the errors between CERES and ISCCP are lower. This most likely can be associated to the fact that CERES has a much larger horizontal resolution than CloudSat. Therefore, the CERES sensor will detect a larger fraction of cloud than CloudSat. One more reason for the smaller errors would related to the fact that CERES is a passive sensor, and the data going into the ISCCP dataset is pulled from passive

radiometers on their associated satellites. The errors for this comparison as well as the others can be found in Table 4.5.

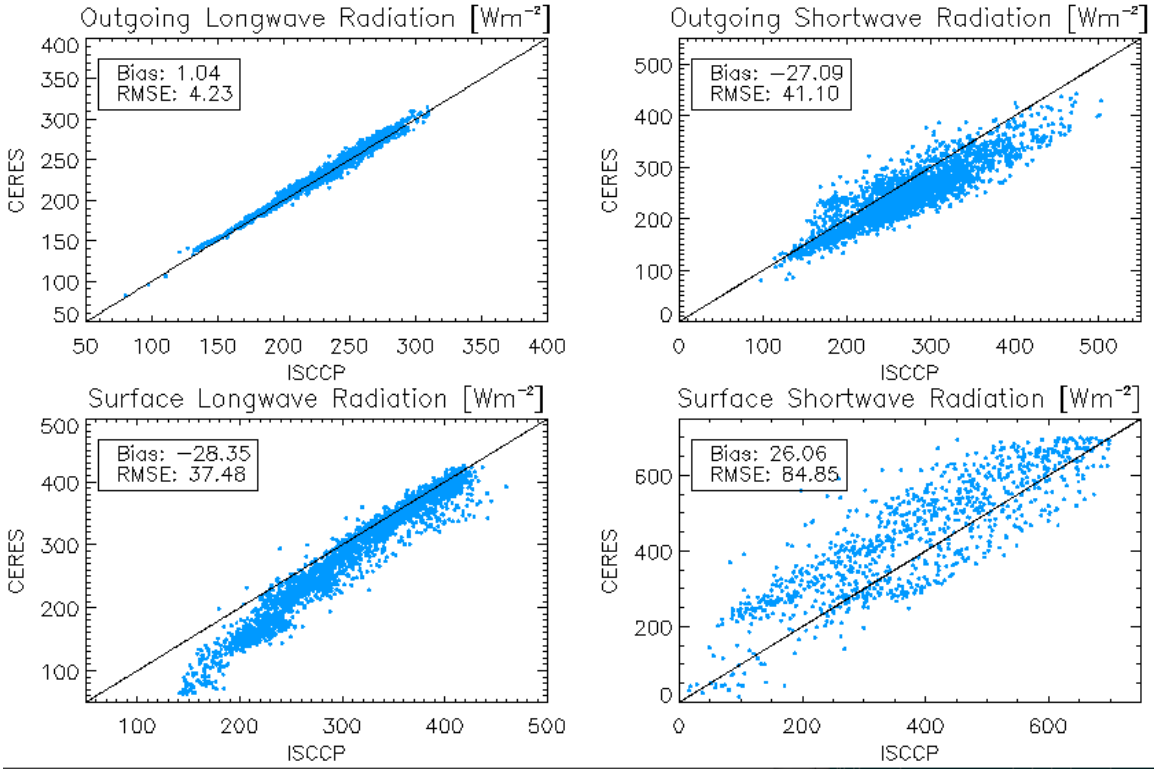

Figure 4.40. Scatter plot showing the comparison of the fluxes CERES FLASHFlux to the ISCCP FD product from January 2007 to July 2007. Each point is averaged to a 5 x 5 degree latitude/longitude grid box and contains outgoing and surface LW radiation, and outgoing and surface SW radiation.

	FHR-A/CERES Bias (RMS)	FHR-A /ISCCP Bias (RMS)	FHR-A /ISCCP Bias (RMS)
OLR	-3.57 (4.92)	-2.42 (6.64)	1.04 (4.23)
OSR	1.72 (17.79)	-46.34 (70.26)	-27.09 (41.10)
SLR	2.74 (8.61)	-13.33 (30.88)	-28.35 (37.48)
SSR	13.01 (21.97)	39.98 (111.31)	26.06 (84.06)

Table 4.5. This table shows the Bias and RMS errors from the three comparisons between FHR-A/CERES, FHR-A/ISCCP, and CERES/ISCCP. All values are in Wm^{-2}.

5. CONCLUSIONS

5.1 Summary

The Earth's radiative budget had been a topic of study for many years, but never until the launch of CloudSat have we been able to obtain vertical distribution of cloud heights and cloud base in particular. Fluxes and heating rates were provided in the existing 2B-FLXHR product from the CloudSat DPC, but these data were limited by CloudSat's inability to detect low clouds due to either effects of ground clutter or they were below the minimal detectable signal of the CPR. Similarly thin sub-visible cirrus clouds and aerosol layers go undetected by the radar. By combing the CALIPSO lidar data and MODIS satellite data this study was able create a new more comprehensive dataset of cloud and aerosol locations in the atmosphere along with their properties. Clouds undetected by CloudSat were included in a combined cloud mask along with aerosol. From the CALIPSO measurements, optical depths of aerosol were determined and the thin cirrus properties were calculated using a lidar-transmission technique. Properties of new clouds and aerosol were then included in a radiative transfer model, creating a new dataset from which the impacts of clouds and aerosol on the ERB can be assessed.

Four case studies were presented to illustrate the effects of these undetected clouds, aerosols, and precipitation properties have on the radiative heating rates. Low clouds showed heating above the cloud layer from the albedo effect, while cooling below occurred from blocking solar radiation. Sub-visible cirrus had little effect in the SW, but did absorb LW radiation within the cloud layer, and trapped LW radiation below the cirrus, causing a warming in the atmosphere below. Precipitation properties were changed to remove an artificial spike in heating rates occurring around 8 km due to too much liquid water from precipitation in the clouds. A Saharan dust layer was observed to view the impacts of dust. Heating was observed above the aerosol layer and within the layer suggesting that the aerosol effect is dominated by reflected and absorbed solar radiation.

The impacts of the undetected clouds and aerosol were observed globally, both seasonally and annually. For low clouds the impacts were most profound in three subsidence regions in the sub-tropics off the western coasts of N. America, S. America, and Africa. Low clouds are also undetected frequently in the mid-latitude storm tracks. Overall, the low clouds have an overall cooling effect reflecting 5.7 Wm^{-2} and trapping 2.1 Wm^{-2} in LW at TOA. Sub-visible cirrus clouds were found to have little effect on the global scale, but did provide a larger amount of LW trapping at the surface in the tropics where deep convection is more frequent. Globally the cirrus warmed the surface by about 1 Wm^{-2}, but average by latitude over the tropics the impact approaches 3.5 Wm^{-2}, and regionally impacts can reach up to 8-10 Wm^{-2}.

Aerosol information from CALIPSO provided the ability to look at the radiative impact of aerosol. Many studies have used the TOA SW radiative effect to see the

impacts of aerosol, and it is listed in the IPCC to have an impact at TOA of around -5 Wm^{-2}. This study calculated a direct effect of -3 Wm^{-2}, but this was expected to be lower due the aerosols overlying low clouds not used in the calculation and missed aerosol from the high confidence CAD scores. This study was able to pinpoint Saharan dust transport and the impacts of dust over the Atlantic, as well as pick up sources of pollution over India and China.

After finding the impacts of undetected clouds, the radiative forcing of clouds were examined. The seasonal shifts in cloud distributions and their radiative forcings were dominated by shifts in the ITCZ and mid-latitude storm tracks. The magnitudes of radiative forcing matched observations closely of the other studies. The TOA cloud forcing is 44.7 Wm^{-2} associated with reflected sunlight from cloud while 24.6 Wm^{-2} less radiation is emitted to space, leaving an overall cloud forcing of -20.1 Wm^{-2}. Similar patterns were found for surface forcing also leading to a cooling effect of clouds with a forcing of -28.9 Wm^{-2}.

One of the more important ways to use flux data is to view the energy balance of the Earth. At a first glance (Figure 4.37) the energy system is not closed being off by $\sim$25 Wm^{-2}, but this in effect is counteracted by the high amount of incoming solar due to lack of measurement at the poles, and the low amount of reflected shortwave due to lack of sampling across the diurnal cycle of 92 Wm^{-2}. Completing comparisons of this study to CERES showed that the error is most likely in the SW and at the surface. As a partial solution to this issue, the diurnal cycle was sampled in the following way. The solar zenith angle was changed that every 12 pixels along track was characterized by a different zenith angle. This provided a way of

simulating the effect of changing solar elevation through the diurnal cycle. It does not account for diurnal changes within the atmosphere. This method proved to work and helped increase the outgoing solar radiation to 96 Wm^{-2} for the entire period of study. Surface values showed that there is also agreement with more current estimates of solar flux. The downward component of the LW radiation at the surface is higher with calculated value of 349 Wm^{-2}.

Finally, as mentioned above the dataset was compared to CERES as well as ISCCP flux data to assess the validity of our data. Comparisons with both showed good agreement especially in the outgoing fluxes. Larger differences existed in surface fluxes, but are to be expected due to differences in resolution, increased missing data at the surface, different cloud properties, and different modeling techniques to obtain surface values.

5.2 Future Work

The work presented in this paper was designed to give an overall estimate of the Earth Radiative budget from a combined CloudSat, CALIPSO, and MODIS viewpoint. However, there is still work to be completed in order to continue to improve the properties of the clouds, aerosol, and land properties to make sure the best data is used to calculate the fluxes and heating rates.

To start the cloud mask created for the FHR-A data needs to be compared to the 2B-Geoprof-Lidar product from CloudSat and ultimately substitute the latter product used instead of the experimental product developed in this study. CloudSat

also has a 2C-Precip-Column product that will soon be released. This product will provide more information on the location of precipitation vertically within a cloud, as well as an estimate of the liquid water content from precipitation within the cloud. This will allow liquid to be properly distributed in the cloud, as well as give a better value than the climatological value for liquid water content used in this study. By adding these CloudSat products, the data can the be used and matched to 2B-Cld-Class which is a product that distinguishes cloud type (such as, cumulus, stratus, cirrus, etc…). This would provide the opportunity to deduce the impacts of each type on the radiative budget. Finally, the last product to add to the flux calculations would be AMSR-E surface type for use of detecting sea ice in the oceans. Currently climatological values from International Geosphere-Biosphere Programme (IGBP) are used to define sea ice, and the use of AMSR-E data would allow for real time positioning of sea ice. This could be used to look at the flux changes over the past few years to see how the decrease in sea ice has impacted atmospheric fluxes and heating rates.

Results from this study show that using aerosol information from CALIPSO provides the vertical placement of aerosol layers. The aerosol properties from SPRINTARS do not exactly match that of CALIPSO. Therefore, it would be useful to reexamine the how the aerosols are being modeled in the radiative transfer model to try to match values from the last IPCC report, such as from MODIS. It is also useful to reevaluate the filter procedures used in locating CALIPSO aerosols. There are other aerosol products from CALIPSO that provide more information on the cloud/aerosol detection confidences. Also, thick aerosol layers can provide false

information on the aerosol optical depth if the lidar is attenuated, so these cases could be separated to remove bad data. The MODIS satellite also provides aerosol information, but not in a vertical profile. It could be used in tandem with CALIPSO to help provide the best overall estimates of aerosol properties to be used in the FHR-A product. Finally, not all aerosol are used in the radiative effect calculation due to the presence of cloud in the same pixel. It would be useful to look three cases; clear sky, all sky, and cloud sky. These case would help to get more accurate results of the aerosol impact on our climate.

The changing of zenith angle along the orbit to sample the diurnal cycle provided estimates of SW fluxes that were close to other studies of the ERB. Even though this reduces the overall sample resolution, it is still high enough to provide estimates of the components of the ERB shown in this study. More work can be done on this solar zenith estimate to confirm its accuracy by comparing it with other products, which will help to assess how well the flux and heating rates calculations are doing. If the comparisons prove to be accurate the results of this study can be reprocessed using this data to provide a second estimate of cloud and aerosol effects.

Finally, with the promising results of this study, it will be helpful to work with the CloudSat DPC to try and integrate the combined data into the current 2B-FLXHR product and create a separate product allowing the user to have radar only, and combined estimate of fluxes and heating rates. The properties used in this study can also be used to improve some of the estimates made in the 2B-FLXHR product to also improve its data.

6. REFERNECES

Ackerman, S. A., 1997: Remote sensing aerosols using satellite infrared observations. J. Geophys. Res., 102, 17 069–17 079.

Ardanuy, P. E., L. L. Stowe, A. Gruber, M. Weiss, and C. L. Long, 1989: Longwave cloud radiative forcing as determined from Nimbus-7 observation. J. Climate,2, 766–799.

Ardanuy, P. E., L. L. Stowe, A. Gruber, and M. Weiss, 1991: Shortwave, longwave and net cloud-radiative forcing as determined from Nimbus 7 observations. J. Geophys. Res.,96, 18 537–18 549.

Barkstrom, B. R., 1984: The Earth Radiation Budget Experiment (ERBE). Bull. Amer. Meteor. Soc., 65:1170–1185.

Charlson, R. J., J. Langner, H. Rodhe, C. B. Leovy, and S. G. Warren, 1991: Perturbation of the northern hemisphere radiative balance by backscattering from anthropogenic sulfate aerosols. Tellus, 43A–B:152–163.

Chand, D., R. Wood, T.L. Anderson, S.K. Satheesh, and R.J. Charlson, 2009: Satellite-derived direct radiative effect of aerosols dependent on cloud cover. Nature Geoscience, 2, 181-184.

Comstock, J. M. and K. Sassen, 2001: Retrieval of cirrus cloud radiative and backscattering properties using combined lidar and infrared radiometer (LIRAD) measurements. J. Atmos. Oceanic Technol., 18:1658–1673.

D'Almeida, G. A., P. Koepke, and E. P. Shettle, 1991: Atmospheric Aerosols: Global Climatology and Radiative Characteristics. A. Deepak, 561 pp.

Ellis, J. S. and T. H. VonderHaar, 1976: Zonal average radiation budget measurements from satellites for climate studies. Atmospheric Science Paper 240, Dept. of Atmospheric Sciences, Colorado State University, 57 pp.

Gill A.E. 1980: Some simple solutions for heat-induced tropical circulations. Q. J. R. Meteorol. Soc. 106: 447 – 462.

Haladay, T. and G. Stephens, 2009: Characteristics of tropical thin cirrus clouds deduced from joint CloudSat-CALIPSO observations. J. Geophys. Res., 114:D00A25. doi:10.1029/2008JD010675

Halley, E., 1686: An historical account of the trade winds, and monsoons, observable in the seas between and near the tropicks, with an attempt to assign physical cause of said winds. Philos. Trans. Roy. Soc. London., 16:153–168.

Harries, J. E., Coauthors 2005: The Geostationary Earth Radiation Budget Project. Bull. Amer. Meteor. Soc., 86:945–960.

Harrison, E. F., P. Minnis, B. R. Barkstrom, V. Ramanathan, R. D. Cess, and G. G. Gibson, 1990: Seasonal variation of cloud radiative forcing derived from the Earth Radiation Budget Experiment. J. Geophys. Res, 95:18687–18703.

Hartmann, D. L. and D. A. Short, 1980: On the use of earth radiation budget statistics for studies of clouds and climate. J. Atmos. Sci., 37:1233–1250.

Hartmann, D. L., H. H. Hendon, and R. A. Houze Jr., 1984: Some implications of the mesoscale circulations in tropical cloud clusters of large-scale dynamics and climate. J. Atmos. Sci., 41:113–121.

Hartmann, D. L., V. Ramanathan, A. Berroir, and G. E. Hunt, 1986: Earth radiation budget data and climate research. Rev. Geophys, 24:439–468.

Hartmann, D. L., M. E. Ockert-Bell, and M. L. Michelsen, 1992: The effect of cloud type on Earth's energy balance: Global analysis. J. Climate, 5:1281–1304.

Hartmann, D. L., 1994: Global Physical Climatology, 411 pp., Academic, New York.

Hendon, H. H., B. Liebmann, M. Newman, J. D. Glick, and J. E. Schemm, 2000: Medium-range forecast errors associated with active episodes of the Madden–Julian oscillation. Mon. Wea. Rev, 128:69–86.

Jacobowitz, H., W. L. Smith, H. B. Howell, F. W. Nagle, and J. R. Hickey, 1979: The first 18 months of planetary radiation budget measurements from the Nimbus 6 ERB experiment. J. Atmos. Sci., 36:501–507.

Lau, K-M. and L. Peng, 1987: Origin of low-frequency (intraseasonal) oscillations in the tropical atmosphere. Part I: Basic theory. J. Atmos. Sci., 44:950–972.

L'Ecuyer, T., N. Wood, T. Haladay, G. L. Stephens, and P. W. Stackhouse, 2008: Impact of clouds on atmospheric heating based on the R04 CloudSat fluxes and heating rates dataset. J. Geophys. Res., 113:D00A15. doi:10.1029/2008JD009951.

L'Ecuyer, T. S., and J. H. Jiang, 2010: Touring the atmosphere aboard the A-Train. Physics Today, 63, 36-41.

Lin, B., P. W. Stackhouse Jr., P. Minnis, B. A. Wielicki, Y. Hu, W. Sun, T-F. Fan, and L. M. Hinkelman, 2008: Assessment of global annual atmospheric energy balance from satellite observations. J. Geophys. Res., 113:D16114. doi:10.1029/2008JD009869.

Liou, K. N., 1986: Influence of cirrus clouds on weather and climate processes: A global perspective. Mon. Wea. Rev., 114:1167–1199.

Liou, K. N., 1992: Radiation and Cloud Processes in the Atmosphere: Theory, Observation, and Modeling. Oxford University Press, 487 pp.

Lo, C., J. M. Comstock, and C. Flynn, 2006: An atmospheric radiation measurements value-added product to retrieve optically thin cloud visible optical depths using micropulse lidar, DOE/SC-ARM/TR-077, U.S. Dep. of Energy, Washington, D. C.

Kalashnikova, O. V. and I. N. Sokolik, 2002: Importance of shapes and compositions of wind-blown dust particles for remote sensing at solar wavelengths. Geophys. Res. Lett., 29:1398. doi:10.1029/2002GL014947.

Kandel R., and Coauthors, 1998: The ScaRaB Earth Radiation Budget dataset. Bull. Amer. Meteor. Soc.,79, 765–783.

Kiehl, J. T. and K. E. Trenberth, 1997: Earth's annual global mean energy budget. Bull. Amer. Meteor. Soc., 78:197–208.

Kim, D. and V. Ramanathan, 2008: Solar radiation budget and radiative forcing due to aerosols and clouds. J. Geophys. Res., 113:D2203. doi:10.1029/2007JD008434.

King, M. D., S-C. Tsay, S. Platnick, M. Wang, and K-N. Liou, 1997: Cloud retrieval algorithms for MODIS: Optical thickness, effective particle radius, and thermodynamic phase. MODIS Algorithm Theoretical Basis Doc. ATBD-MOD-05, 79 pp.

Klein, S. A. and D. L. Hartmann, 1993: The seasonal cycle of low stratiform clouds. J. Climate, 6:1587–1606.

Mace, G. G., Q. Zhang, M. Vaughan, R. Marchand, G. Stephens, C. Trepte, and D.Winker, 2009: A description of hydrometeor layer occurrence statistics derived from the first year of merged Cloudsat and CALIPSO data. J. Geophys. Res., 114:D00A26.doi:10.1029/2007JD009755.

Madden, R. A. and P. R. Julian, 1972: Description of global-scale circulation cells in the tropics with a 40–50 day period. J. Atmos. Sci., 29:1109–1123.

Maloney, E. D. and D. L. Hartmann, 2000: Modulation of hurricane activity in the Gulf of Mexico by the Madden–Julian oscillation. Science, 287:2002–2004.

Manabe, S. and R. F. Strickler, 1964: Thermal equilibrium of the atmosphere with a convective adjustment. J. Atmos. Sci., 21:361–385.

Menzel, P., and Strabala, K., 1997, Cloud top properties and cloud phase algorithm theoretical basis document. MODIS Algorithm Theoretical Basis Document No. ATBD-MOD-04, Version 5.

Mitchell, D. L., A. Macke, and Y. Liu, 1996: Modeling cirrus clouds. Part II: Treatment of radiative properties. J. Atmos. Sci., 53:2967–2988.

Omar, A. H., Coauthors 2009: The CALIPSO automated aerosol classification and lidar ratio selection algorithm. J. Atmos. Oceanic Technol., 26:1994–2014.

Pincus, R. and M. B. Baker, 1994: Effect of precipitation on the albedo susceptibility of clouds in the marine boundary layer. Nature, 372:250–252.

Quaas, J., O. Boucher, N. Bellouin, and S. Kinne, 2008: Satellite-based estimate of the direct and indirect aerosol climate forcing, J. Geophys. Res., 113:D05204.doi:10.1029/2007JD008962.

Ramanathan, V., 1987: The role of earth radiation budget studies in climate and general circulation research. J.Geophys. Res., 92, 4075–4095.

Ramanathan, V., R. D. Cess, E. F. Harrison, P. Minnis, B. R. Barkstrom, E. Ahmad, and D. Hartmann, 1989: Cloud-radiative forcing and climate: Results from the Earth Radiation Budget Experiment. Science, 243:57–63.

Raschke, E., A. Ohmura, W. B. Rossow, B. E. Carlson, Y-C. Zhang, C. Stubenrauch, M. Kottek, and M. Wild, 2005: Cloud effects on the radiation budget based on ISCCP data (1991 to 1995). Int. J. Climatol., 25:1103–1125.

Remer, L. A. and Y. J. Kaufman, 2006: Aerosol direct radiative effect at the top of the atmosphere over cloud free ocean derived from four years of MODIS data. Atmos. Chem. Phys., 6:237–253.

Ritter, B., and J.-F. Geleyn, 1992: A comprehensive radiation scheme for numerical weather prediction models with potential applications in climate simulations. Mon. Wea. Rev.,120, 303–325.

Rossow, W. B. and Y-C. Zhang, 1995: Calculation of surface and top of atmosphere radiative fluxes from physical quantities based on ISCCP data sets. 2: Validation and first results. J. Geophys. Res., 100:D1,. 1167–1197.

Sassen, K., Z. Wang and D. Liu, 2009: Cirrus clouds and deep convection in the tropics: Insights from CALIPSO and CloudSat. J. Geophys. Res., 114, D00H06, doi:10.1029/2009JD011916.

Schiffer, R. A. and W. B. Rossow, 1983: The International Satellite Cloud Climatology Project (ISCCP): The first project of the World Climate Research Programme. Bull. Amer. Meteor. Soc., 64:779–784.

Slingo, A., 1990: Sensitivity of earth's radiation budget to changes in low clouds. Nature, 343:49–51.

Slingo, A. and J. M. Slingo, 1988: The response of a general circulation model to cloud longwave radiative forcing. I: Introduction and initial experiments. Quart. J. Roy. Meteor. Soc., 114:1027–1062.

Slingo, A. and J. M. Slingo, 1991: Response of the National Center for Atmospheric Research Community Climate Model to improvements in the representation of clouds. J. Geophys. Res., 96:15341–15357.

Sohn, B-J. and E. A. Smith, 1992: The significance of cloud-radiative forcing to the general circulation on climate time scales—A satellite interpretation. J. Atmos. Sci, 49:845–860.

Sokolik, I. and O. Toon, 1996: Direct radiative forcing by anthropogenic mineral aerosols. Nature, 381:681–683.

Stackhouse, P. W., D. P. Kratz, G. R. McGarragh, S. K. Gupta and E. B. Geier, 2006: Fast Longwave and Shortwave Flux (FLASHFlux) products derived from CERES and MODIS measurements, 12th Conference on Atmospheric Radiation, Madison, Wisconsin.

Stephens, G., 1978: Radiation Profiles in Extended Water Clouds. II: Parameterization Schemes. J. Atmos. Sci. , 35, 2123-2132.

Stephens, G. L., Coauthors 2002: The CloudSat mission and the A-Train: A new dimension of space-based observations of clouds and precipitation. Bull. Amer. Meteor. Soc., 83:1771–1790.

Stephens, G. L., 2005: Cloud feedbacks in the climate system: A critical review. J. Clim., 18, 237-273.

Stephens, G. L., D. G. Vane, R. J. Boain, G. G. Mace, K. Sassen, Z. Wang, A. J. Illingworth, E. J. O'Connor, W. B. Rossow, S. L. Durden, S. D. Miller, R. T. Austin, A. Benedetti, C. Mitrescu, and the CloudSat Science Team, 2002: The CloudSat Mission and the A-TRAIN: A new dimension to space-based observations of clouds and precipitation. Bull. Am. Met. Soc., 83, 1771-1790.

Stephens, G. L., A. Slingo, M. J. Webb, P. J. Minnett, P. H. Daum, L. Kleinman, I. Wittmeyer, and D. A. Randall, 1994: Observations of the earth's radiation budget in relation to atmospheric hydrology 4: Atmospheric column radiative cooling over the world's oceans. J. Geophys. Res., 99, (D9) 18,585-18,604.

Stephens, G. L., S. C. Tsay, P. W. Stackhouse, and P. J. Flatau, 1990: The Relevance of the Microphysical and Radiative Properties of Cirrus Clouds to Climate and Climate Feedback. J. Atmos. Sci., 47, 1742-1754.

Stephens, G. L., 1980: Radiative Properties of Cirrus Clouds in the Infrared Region. J. Atmos. Sci., 37, 435-446.

Stephens, G. L., G. G. Campbell, and T. H. Vonder Haar, 1981. Earth radiation budgets. J. Geophys. Res 86:9739–9760.

Stephens, G. L., S-C. Tsay, P. W. Stackhouse Jr., and P. J. Flatau, 1990: The relevance of the microphysical and radiative properties of cirrus clouds to climate and climate feedback. J. Atmos. Sci., 47:1742–1753.

Takemura, T., T. Nakajima, O. Dubovik, B. N. Holben, and S. Kinne, 2002: Single-scattering albedo and radiative forcing of various aerosol species with a global three-dimensional model. J. Climate, 15:333–352.

Tian, B. and V. Ramanathan, 2002: Role of tropical clouds in surface and atmospheric energy budget. J. Climate, 15:296–305.

Trepte, Q. Z., P. Minnis, C. R. Trepte, S. Sun-Mack, and R. Brown, 2010: Improved cloud detection in CERES Edition 3 algorithm and comparison with the CALIPSO Vertical Feature Mask. Proc. AMS 13th Conf. Atmos. Rad. and Cloud Phys., Portland, OR, June 27 – July 2, JP1.32.

Trenberth, K. E., J. T. Fasullo, and J. Kiehl, 2009: Earth’s global energy budget. Bull. Amer. Meteor. Soc., 90:311–323.

Twomey, S., 1977: The influence of pollution on the shortwave albedo of clouds. J. Atmos. Sci., 34:1149–1152.

Vaughan, M., D. Winker, and K. Powell, 2005: CALIOP Algorithm Theoretical Basis Document, part 2, Feature detection and layer proper- ties algorithms, PC-SCI-202.01, NASA Langley Res. Cent., Hampton, Va. (Available at http://www-calipso.larc.nasa.gov/resources/project_documentation.php).

Vonder Haar, T. H. and V. E. Suomi, 1971: Measurements of the Earth's radiation budget from satellites during a five-year period. Part I: Extended time and space means. J. Atmos. Sci, 28:305–314.

Warren, S. G., Hahn, C. J., London, J., Chervin, R. M. and Jenne, R. 1988. Global Distribution of Total Cloud Cover and Cloud Type Amount Over the Ocean. NCAR TN-317 STR, 212 pp.

WCP-55, 1983: Report of the expert meeting on aerosols and their climate effects. World Meteorological Organization, Geneva, 107 pp.

Webster, P. J., 1994: The role of hydrological processes in ocean– atmosphere interactions. Rev. Geophys, 32:427–276.

Wielicki, B. A., B. R. Barkstrom, E. F. Harrison, R. B. Lee III, G. L. Smith, and J. E. Cooper, 1996: Clouds and the Earth's Radiant Energy System (CERES): An Earth Observing System experiment. Bull. Amer. Meteor. Soc., 77:853–868.

Winker, D. M., W. H. Hunt, and C. A. Hostetler, 2004: Status and performance of the CALIOP lidar. Laser Radar Techniques for Atmospheric Sensing. U. N. Singh, Ed. International Society for Optical Engineering (SPIE Proceedings Vol. 5575), 8–15.

Winker, D. M., W. H. Hunt, and M. J. McGill, 2007: Initial performance assessment of CALIOP. Geophys. Res. Lett., 34:L19803. doi:10.1029/2007GL030135.

Yu, H., Coauthors 2006: A review of measurement-based assessment of aerosol direct radiative effect and forcing. Atmos. Chem. Phys., 6:613–666.

Zhang, Y., W. B. Rossow, and A. A. Lacis, 1995: Calculation of surface and top of atmosphere radiative fluxes from physical quantities based on ISCCP datasets 1. Method and sensitivity to input data uncertainties. J. Geophys. Res., 100:1149–1165.

Zhang, J., S. A. Christopher, L. Remer, and Y. J. Kaufmann, 2005b: Shortwave aerosol radiative forcing over cloud-free oceans from Terra: 2. Seasonal and global distributions. J. Geophys. Res., 110.D10S24, doi:10.1029/2004JD005009.